2

# Optics Research

1971

Issued 24 April 1972

Prepared for the Advanced Research Projects Agency
under Electronic Systems Division Contract F19628-70-C-0230 by

Lincoln Laboratory

MASSACHUSETTS INSTITUTE OF TECHNOLOGY

Lexington, Massachusetts

The work reported in this document was performed at Lincoln Laboratory, a center for research operated by Massachusetts Institute of Technology. This work was sponsored by the Advanced Research Projects Agency of the Department of Defense under Air Force Contract F19628-70-C-0230 (ARPA Order 600). Where noted, research sponsored by the Air Pollution Control Office of the Environmental Protection Agency is included.

ABSTRACT

This report covers work of the Optics Division at Lincoln Laboratory for the period 1 July through 31 December 1971. The topics covered are laser technology and propagation, optical measurements and instrumentation, and laser radar and tracking. Additional information on the optics program may be found in the semiannual technical summary reports to the Advanced Research Projects Agency.

Accepted for the Air Force
Joseph R. Waterman, Lt. Col., USAF
Chief, Lincoln Laboratory Project Office

# CONTENTS

# INTRODUCTION

## 1. LASER TECHNOLOGY AND PROPAGATION

The existing program to calculate thermal blooming of a CW beam (steady state) has been improved by including the capability of using a truncated beam source (possibly with central obscuration). In addition, computation time has been further reduced by altering the reference wavefront at each step so that it coincides more nearly with the actual wavefront. Examples are given.

Programs have been developed for the time-dependent propagation of a high-energy laser pulse through an absorbing atmosphere. Kinetic cooling and saturation effects are presently omitted. Separate codes for the short, long and intermediate time regimes (compared with hydrodynamic time) have been developed. A sample calculation is presented.

The eikonal theory of thermal blooming of a pulsed laser beam has been extended to include the variation of atmospheric absorption with altitude. Effects of saturation are also now taken into account. Some typical results are shown.

A piezoelectric stress gauge has been developed to monitor the temporal development of the impulse delivered to a target when irradiated by a high energy density pulse of a laser beam. The objective is to provide sufficient temporal resolution to distinguish between blow-off and blast wave coupling.

The experimental program on laser-induced breakdown in air has continued. Emphasis has been placed on studying the initiation mechanism and the interaction with the surrounding air.

The study of the explosion of individual fog particles under irradiation by a 10.6-$\mu$m laser beam has been extended to longer times (~100 $\mu$sec) by using a micro-schlieren apparatus. A model has been developed which predicts the spread in a laser beam traversing a clearing hole as a function of time.

The primary thrust of the EDL laser effort is the design and construction of an E-beam $CO_2$ device capable of delivering 500 J.

A small E-beam laser has been constructed using an RCA electron gun capable of 20 mA (continuous). The purpose of this laser is to test theories for larger scale devices and perform parametric studies.

Studies of the spatial and temporal dependence of the gain of a pulsed HF laser have been carried out, with the results being compared to those for $CO_2$ lasers. Use of a Marx-bank pulser has substantially increased the energy output of the 75-cm HF pin laser to about 360 mJ/pulse. Studies of E-beam initiated chemical lasers have begun.

Measurements of the medium homogeneity in a TEA pin laser have been continued, and extended to several different total pressures. The results suggest that the TEA laser should make an excellent single-pass amplifier, although distortion in an oscillator could be quite severe.

A number of CO lasers have been assembled and used to investigate the physical and chemical processes involved in sealed-off CO lasers. Improved lasers have been designed.

A program has been undertaken to numerically model the unharmonic pumping effect in the CO laser. Considerable success has been achieved in predicting gains, saturation intensity and the effect of the radiation field on the electron gas.

## II. OPTICAL MEASUREMENTS AND INSTRUMENTATION

An airborne imaging experiment was performed using a wing-tip point source to study the degradation of telescope performance in high-altitude flight. Use of the wing-tip source, which was a passive retroreflector reflecting a laser beam, was implemented to isolate fuselage boundary-layer effects from other sources of degradation. Results indicate that a strong optical disturbance is localized just outside the aircraft window.

Stellar images have been recorded at various latitudes and altitudes with the new diffraction-limited, long-focal-length telescope mounted in the KC-135 aircraft. Agreement with previous results was substantial, in that the principal source of airborne image degradation was identified with the fuselage boundary layer. Angular dispersion was found to act as a random variable in the presence of other airborne perturbations.

The Laboratory-model, corner cube shearing interferometer has been used to make MTF measurements of the atmosphere from the KC-135 optical aircraft. Stellar sources as well as the wing-tip retroreflector were used to illuminate the interferometer. Preliminary results indicate that the principal source of MTF degradation is the aircraft boundary layer.

The spectral characteristics of the ZnS upconversion and the UV-induced IR absorption have been examined in more detail using a series of nine, 1-$\mu$m-bandpass IR filters centered on wavelengths 2 $\mu$m apart from 2 to 16 $\mu$m. The visible output has been measured as a function of IR wavelength and intensity, as well as time after IR turn-on. The results are being studied to determine the upconversion mechanism, as well as the overall IR sensitivity and imaging capability.

The high-resolution spectra, which were obtained with tunable semiconductor lasers for the 8.7-$\mu$m absorption band of $SO_2$, were compared with theory. The theoretical model for this spectrum, derived elsewhere, on the basis of accurate microwave spectra, was found to be in near-perfect agreement with the laser spectra, once the band center used in the theory was properly adjusted on the basis of the laser data. Pollutant detection using the absorption "fingerprint" has been shown feasible by a multiple-reflection White cell, and by long-path transmission. The White cell results indicate that with increased laser power in the mW range, point sampling of pollutant concentration in the low parts per billion (ppb) region should be possible.

## III. LASER RADAR AND TRACKING

The laser radar imaging system was calibrated with spherical standard targets and used to measure the incoherent backscattering from targets including an aircraft tail section.

The optimum free-carrier concentration for the use of InSb as a Faraday rotator at liquid $N_2$ temperature was computed and confirmed by experiment. An experimental 10.6-$\mu$m isolator using this material was assembled and tested.

For the Firepond 10.6-$\mu$m laser radar, automatic angle and frequency tracking in the pulsed mode was demonstrated on unenhanced light aircraft targets out to ranges of approximately eight miles.

In support of pulse-mode operation, manual range tracking and gating circuits were added to process the pulse signal.

In the course of measuring the characteristics and performance of the components of the Firepond laser radar, the frequency stability of the laser oscillator and the Doppler velocity measurement capability were determined.

The annual average temperature, water vapor partial pressure and 10.6-$\mu$m absorption due to $H_2O$ have been compiled for the Firepond site over a range of seasonal variation.

The laser radar optical system was converted to the duplexed configuration, which will also incorporate a rapid scan imaging capability.

A 48-inch aperture telescope has been installed at the Firepond Research Facility oriented to project a focused spot at a tower 5.4 km distant. The spot size and characteristics will be measured by a scanning IR camera, while the characteristics of the propagation path will be simultaneously measured in the visible spectral region.

# REPORTS ON OPTICS RESEARCH

1 July through 31 December 1971

## PUBLISHED REPORTS

### Journal Articles*

| JA No. | | | |
|---|---|---|---|
| 3811 | A Wide Dynamic Range Photometer for Film Densitometry | D. G. Kocher | J. SMPTE 80, 481 (1971), DDC AD-731934 |
| 3897 | Performance of a Transversely Excited Pulsed HF Laser | S. Marcus<br>R. J. Carbone | IEEE J. Quantum Electron. QE-7, 493 (1971), DDC AD-734115 |

### Meeting Speech†

| MS No. | | | |
|---|---|---|---|
| 3192 | Tunable Infrared Lasers and Their Applications | P. L. Kelley<br>E. D. Hinkley<br>A. Mooradian | NEREM Record 13, Pt. 1, 221 (1971) |

* * * * *

## UNPUBLISHED REPORTS

### Journal Articles

| JA No. | | | |
|---|---|---|---|
| 3962 | Experiment on Cross-Relaxation in $CO_2$ | H. Granek<br>C. Freed<br>H. A. Haus‡ | Accepted IEEE J. Quantum Electron. |
| MS-3189 | Influence of Particles on Laser Induced Air Breakdown | R. J. Hull<br>D. E. Lencioni<br>L. C. Marquet | Accepted Proc. 2nd Laser Workshop [Plenum Press (to be published)] |

### Meeting Speeches†

| MS No. | | | |
|---|---|---|---|
| 2944A | 10.6$\mu$ $CO_2$ Laser Radar | T. J. Gilmartin<br>L. J. Sullivan<br>H. A. Bostick | Seminar, Lowell Technological Institute, Lowell, Massachusetts, 2 December 1971 |
| 3031A | Tunable Laser Spectroscopy | E. D. Hinkley | 2nd European Conference on High-Resolution Molecular Spectroscopy, Dijon, France, 16 September 1971 |

* Reprints available.

† Titles of Meeting Speeches are listed for information only. No copies are available for distribution.

‡ Author not at Lincoln Laboratory.

| MS No. | | | |
|---|---|---|---|
| 3031B | Tunable Laser Spectroscopy – Application to Air Pollution Detection | E. D. Hinkley | European Joint Research Center (EURATOM), Ispra, Italy, 8 September 1971 |
| 3044A | Solid State Tunable Lasers | E. D. Hinkley | Seminar, NASA/Ames, Moffet Field, California, 11 November 1971 |
| 3142 | Remote Heterodyne Detection of Gaseous Pollutants with Tunable Lasers | E. D. Hinkley<br>R. H. Kingston | Conference on Sensing and Environmental Pollutants, Palo Alto, 8-10 November 1971 |
| 3174 | Lasers in Pollution Detection | E. D. Hinkley | Laser & Optics for Applications, M. I. T., 30 July 1971 |
| 3188 | Designs and Experiments Relating to Stable Gas Lasers | C. Freed | Frequency Standards & Metrology, Conference, Quebec, 30 August – 1 September 1971 |
| 3192A | Tunable Lasers in Pollution Applications | E. D. Hinkley | Laser Principles & Applications, Northeastern University, 7 December 1971 |
| 3194 | $CO_2$ Laser Induced Air Breakdown | D. E. Lencioni<br>R. J. Hull<br>L. C. Marquet | American Physical Society, Plasma Division, Madison, Wisconsin, 15-18 November 1971 |
| 3217 | Tunable Semiconductor Lasers | R. H. Rediker | Seminar, Zenith Corporation, Chicago, 8 October 1971 |

# ORGANIZATION

## OPTICS DIVISION

R. H. Kingston, *Head*
R. H. Rediker, *Associate Head*
R. S. Cooper, *Assistant Head*
M. J. Hudson, *Assistant*

## LASER TECHNOLOGY

S. Edelberg, *Leader*
L. C. Marquet, *Assistant Leader*

Bradley, L. C.
Brennan, M. J.
Bushee, J. F., Jr.
Carbone, R. J.
Ferdinand, A. P., Jr.
Granek, H.
Herrmann, J.
Hilton, T. W.
Johnson, J. Q.
Kafalas, P.
Kilcline, C. W.
Kleiman, H.
Lencioni, D. E.
Levine, J. S.
Lowder, J. E.
Marcus, S.
Morency, A. J.
O'Neil, R. W.
Pirroni, J. S.
Theriault, J. B.

## ADVANCED SENSORS

J. O. Dimmock, *Leader*
E. S. Cotton, *Associate Leader*
T. M. Qnist, *Assistant Leader*

Ariel, E. D.
Bauer, J. R.
Bielinski, J. W.
Bryant, B. W.
Chatterton, E. J.
Dickey, D. H.
DiMarzio, E. W.
Edwards, D. M.
Ellis, R. H.
Fulton, M.
Gylfphe, C. H.
Hinkley, E. D.
Kelsall, D.
Malling, L. R.
Merrill, E. R.
Nork, L.
Perry, F. H.
Pike, H. A.
Pitts, R. F.
Ross, A. H. M.*
Scouler, W. J.
Sinclair, R. S.
Stack, T. E.
Sullivan, F. M.
Thomas, M. A.
Wainwright, E. S.
Ziegler, H. L.

## OPTO-RADAR SYSTEMS

A. B. Gschwendtner, *Leader*

Billups, R. R.
Brownson, J. S.
Clay, W. G.
Coles, R. M.
Dyjak, C. P.
Garavano, L. A.
Hull, B. J.
Longaker, P. R.
McPhie, J. M.
Stevens, R. R.
Zieman, H. E.

## LASER SYSTEMS

R. S. Cooper, *Leader*
L. J. Sullivan, *Associate Leader*

Bates, D. H.
Bicknell, W. E.
Capes, R. N., Jr.
Chaulk, L. W.
Daley, J. A., Jr.
Freed, C.
Gilmartin, T. J.
Holtz, J. Z.
Kramer, R.
Marapoti, J. V.
Mehlhorn, H. A.
Meyerhoff, N. J.
Munoz-Flores, J.
O'Donnell, R. G.
Parker, A. C.
Swezey, L. W.
Teoste, R.
Zimmerman, M. D.

*Staff Associate

# I. LASER TECHNOLOGY AND PROPAGATION

## A. THERMAL-BLOOMING PROGRAM

Our code for propagation of a CW beam has been improved in two important ways. First, we have included a capability for using as source a truncated beam, with or without a central obscuration. Since the analytic expression for propagation from a uniformly illuminated aperture predicts that the intensity on axis oscillates with a frequency that approaches infinity as the observation point approaches the source, some doubt has been expressed about the possibility of calculating such a case using a finite-difference scheme. Our results for propagation in vacuum from a uniformly illuminated aperture are shown in Figs. I-1 and I-2.

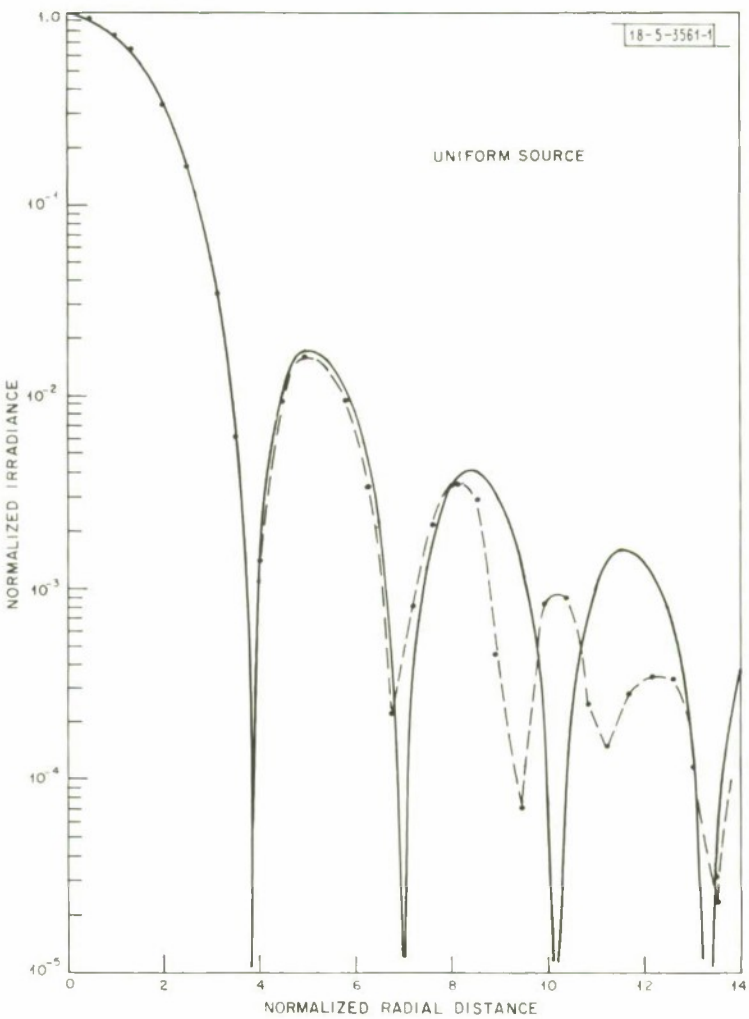


Fig. I-1. Normolized irrodionce I(r)/I(0) in the focol plone os o function of rodius. Uniformly illuminoted mirror (rodius $R_m$ = 63.6 cm) focused ot o ronge $Z_f$ = 1 km. Doshed line is onolytic solution os o function of normolized rodiol distonce $x = kR_m r/Z_f$. Points result from numericol integrotion.

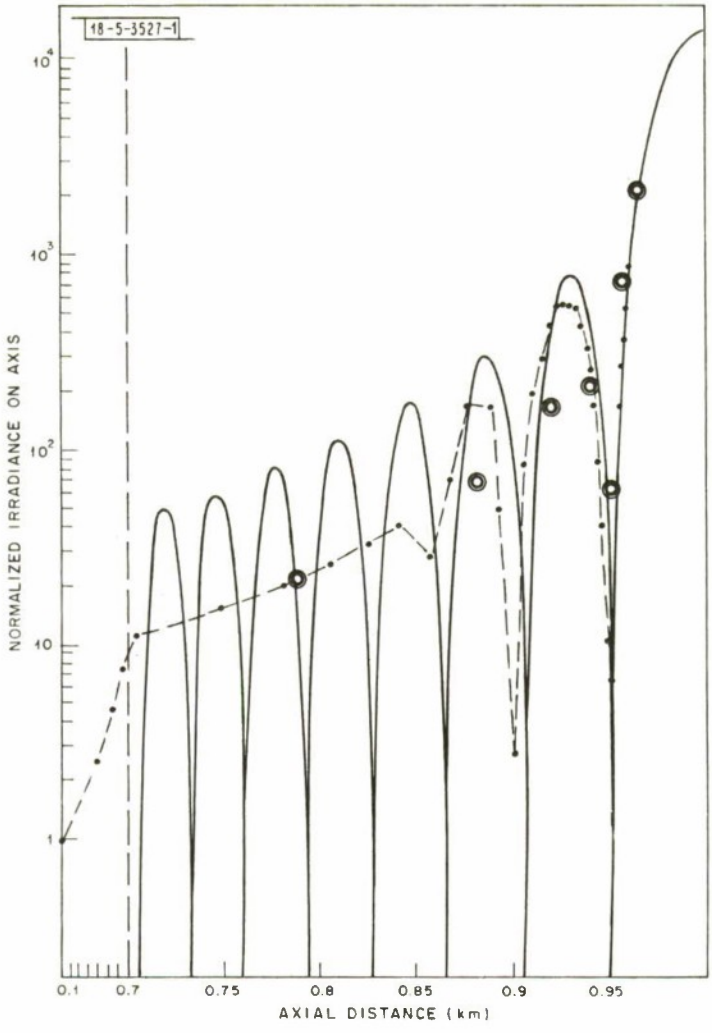


Fig. I-2. Normalized irradiance on the axis I(r = 0, z)/I(r = 0, z = 0) as a function of distance. Same case as in Fig. I-1. Dashed line is analytic solution: Note change in scale at z = 0.7. Circled points are calculated using a coarse mesh (DR = $R_m/8$ at mirror), other points, using a refined mesh (DR = $R_m/20$ at mirror).

In Fig. I-1 we present the irradiance distribution in the focal plane and in Fig. I-2, the irradiance on axis as a function of distance from the source. One observes two significant differences between the computed points and the analytical curves: in Fig. I-1 the computed intensities are too small at large radii, and in Fig. I-2 the computed intensities do not follow the rapid oscillations at small distances. Both of these differences are due to the fact that a finite transverse mesh cannot reproduce the high spatial frequencies that are present in the analytical calculation. It is clear, however, that this has no adverse effect on the computation in regions of high intensity, where only low spatial frequencies are important. Similar remarks apply to Fig. I-3, which shows the irradiance distribution in the focal plane in the presence of a central obscuration. Note that the displacement of the first minimum from its position in the uniformly illuminated case is well reproduced. We conclude that our code simulates the propagation of a truncated beam with good accuracy.

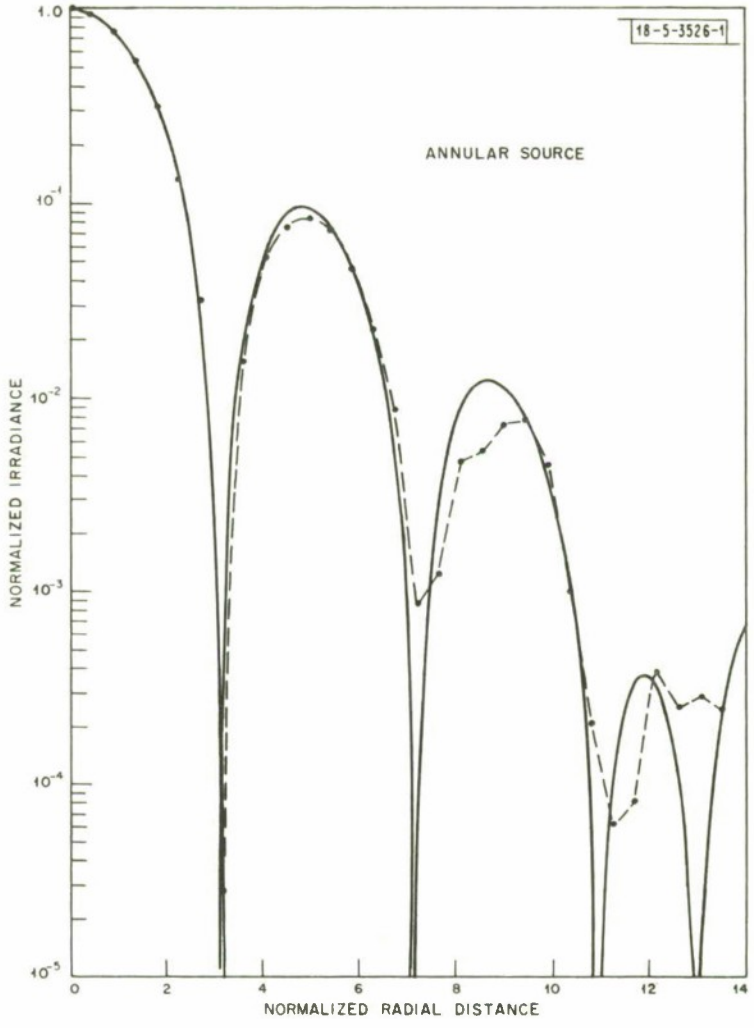


Fig. I-3. Normalized irradionce I(r)/I(0) in focol plone. Some case as Fig. I-1, except a central obscuration with a radius $R_m/2$.

The second improvement consists of the capability for changing the reference wave front at each step in the propagation direction, so that it more nearly coincides with the actual wavefront at that point. This is accomplished by referring the wave front to a new focal point, and is suggested by the well-known fact[1] that the addition of linear and quadratic terms to the phase does not result in aberrations, but merely in a displacement of the focus. The result is twofold: numerical differentiation is more accurate, since it does not have such large phase changes to contend with; and the transverse mesh follows more closely the actual expansion, contraction and displacement of the beam. Thus the grid can be both coarser and less extensive. While the savings may be considerable in cases where thermal blooming predominates (typical computation times have been decreased by a factor of two or three for moderate blooming), it is in cases where strong cooling is present that this feature is most useful. Here the self-focusing effect has meant that prohibitively refined meshes were required before the refocusing feature was

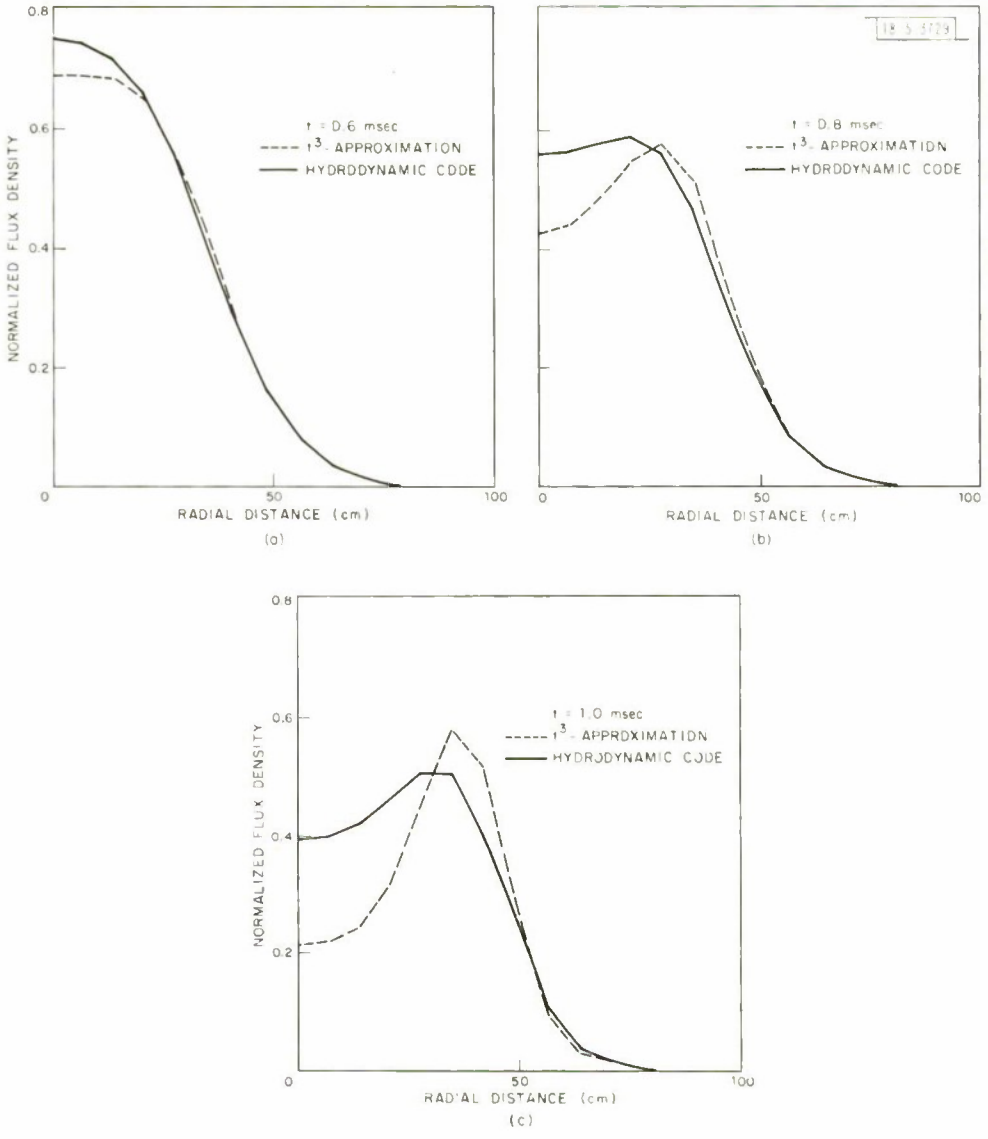


Fig. I-4. Normolized flux density as a functian af radial distance ot o ronge of 10 km for o 1-msec pulse of 5-MW power ond collimoted beom with o $1/e^2$-power diometer af 1 m ot various times (t). Hydradynamic time far this cose is 1 msec.

introduced, whereas now the meshes are quite reasonable. The positive feedback inherent in self-focusing necessitates, even so, more care than is needed for thermally-blooming beams, since a mesh that is too coarse can easily predict spurious catastrophic focusing.

L. C. Bradley
J. Herrmann

## B. THERMAL-BLOOMING PROGRAM FOR PULSES

We have written codes that compute the time-dependent propagation of a pulsed laser beam through an absorbing atmosphere. The beam is assumed to be cylindrically symmetrical, and for each time step the calculation of the beam propagation is done in a manner analogous to that used for the CW case, as we have described it in a previous report.[2] The propagation is assumed to take place along the forward-moving characteristics of the optical scalar wave equation, so that the interaction at a range z and time t corresponds to source emission at time $t - z/c$. It is thus assumed that reflections can be neglected, and time can therefore be treated simply as a parameter.

The interaction of the laser beam with the atmosphere is presently treated as a simple heating, though in the future we intend to include the phenomena of kinetic cooling and saturation. The reaction of the atmosphere is treated by linearized hydrodynamics without viscosity or heat conduction. It can be shown[3] that there are simple approximations for the gas density (and therefore the index of refraction) that are valid for times short and long compared with the time required for a sound wave to cross the beam. We have written codes incorporating each of these approximations. For the intermediate regime, we have written a code that solves the hydrodynamic equations simultaneously with the equation of light propagation. The hydrodynamic equations are treated by a method analogous to that used for light propagation: a Crank-Nicolson approximation is used for the time coordinate and a Galerkin method with circularly symmetric splines for the radial coordinate. This method is implicit; the solution is equivalent to the inversion of a matrix that is block tri-diagonal, and is accomplished by an appropriate generalization of the well-known Thomas algorithm.

The computation for the intermediate case is rather slow, and although we hope that it will be possible to decrease the computation time, it is clear that the approximate codes will always be faster, and in that respect preferable when the respective approximations are valid. In Figs. I-4(a-c) we show a comparison of the results for a single case, computed using the hydrodynamic code and using the short-time approximation. For this case the short-time approximation coincides well with the hydrodynamic code up to half the hydrodynamic time.

L. C. Bradley
J. Herrmann

## C. SURFACE EFFECTS

A piezoelectric stress gauge has been developed to monitor the temporal structure of laser induced interactions at solid surfaces. With $CO_2$ laser radiation and amorphous carbon targets, the compressive stress was found to follow the laser pulse shape for about 5 μsec before tensile relief waves dominated the signal.

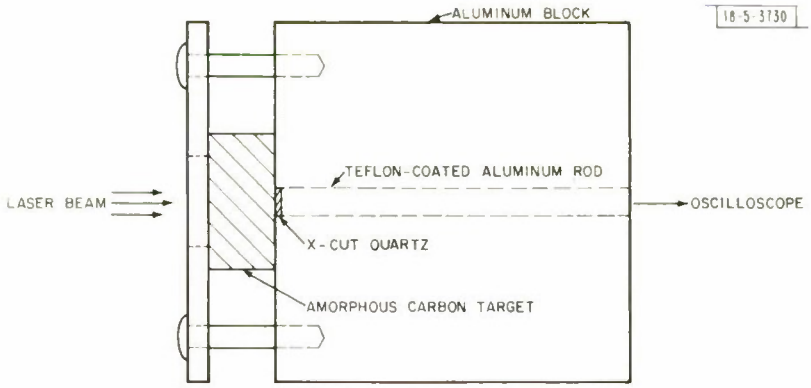


Fig. I-5. Schematic af stress gauge develaped ta manitar temparal structure af laser induced interactians with carban targets.

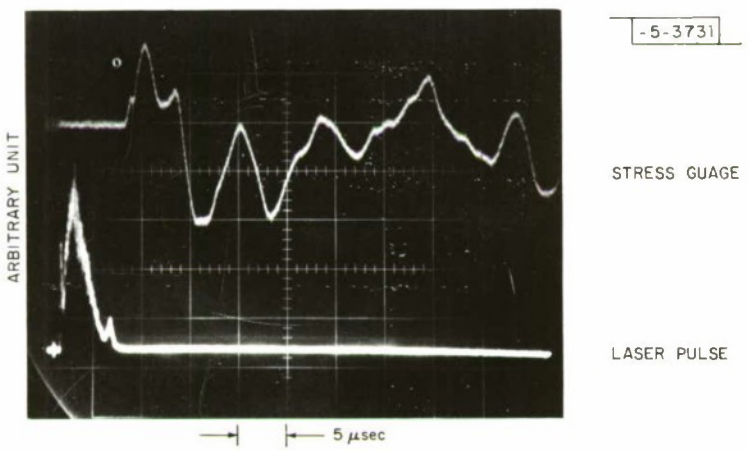


Fig. I-6. Stress gauge respanse (tap trace) to surface vaparizatian af carban target caused by a $CO_2$ laser pulse (3 J) (battam trace). Na breakdawn was induced.

A schematic of the stress gauge is shown in Fig. I-5. The target material is $\frac{1}{2}$ inch of pure amorphous carbon backed up with a thin X-cut quartz piezoelectric crystal and a 4-inch aluminum rod. A compressive stress pulse introduced at the carbon surface propagates through the target and is both reflected and transmitted at the rear surface due to the change in acoustic impedance. Quartz and aluminum have nearly the same acoustic impedance and thus negligible stress reflection occurs at their interface. The compressive stress pulse transmitted through the quartz crystal produces a voltage proportional to the instantaneous compression of the crystal.[4]

$$V = \frac{A d_{11}}{C} \sigma$$

where V is the voltage, A is the cross-sectional area, $d_{11}$ is the piezoelectric modulus, C is the total capacitance and $\sigma$ is the compressive stress in the crystal. The compressive stress is usually equated to the pressure.[4] Thus the temporal structure of a compressive stress pulse input at the carbon surface may be monitored by recording the voltage produced by the quartz crystal as long as the transit time through it is short compared with the compressive pulse width.

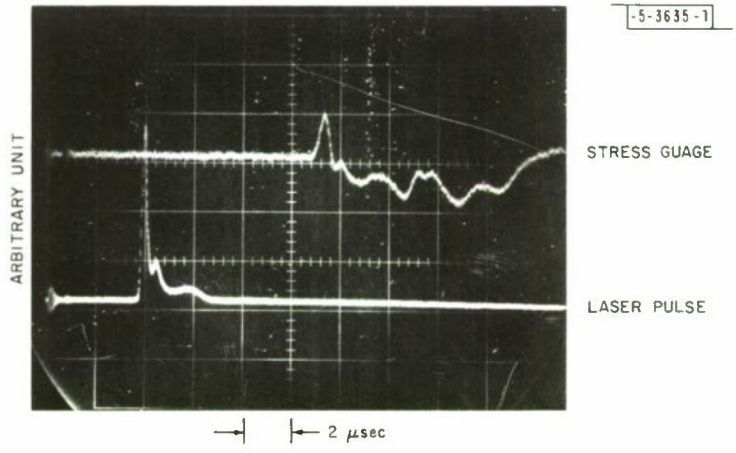


Fig. I-7. Stress gauge response (top trace) to surface vaporization of carbon target caused by a $CO_2$ laser pulse (0.5 J) (bottom trace). No breakdown was induced.

Figures I-6 and I-7 show the carbon stress response for two $CO_2$ laser pulse shapes. In each photo, the top trace is the stress gauge response to surface vaporization and the bottom trace is the laser pulse shape. The delay between the laser pulse and stress response is equal to the compressive stress transit time through the carbon target yielding a speed of sound of 0.225 cm/μsec. Knowing the speed of sound and the reported density of 2.25 gm/cm$^3$, we can calculate Young's modulus ($E = 1.14 \times 10^{11}$ dyne/cm$^2$) and the acoustic impedance ($Z = 5.63 \times 10^5$ gm/cm$^2$ sec). In Fig. I-6, the first three compressive peaks accurately reflect the structure in the laser pulse (~3 J) until the following tensile relief wave drives the signal negative. Figure I-7 shows the stress gauge response for a different laser pulse shape and a total energy of about 0.5 J. No breakdown was induced off the surface of the targets for either of these cases.

Figures I-8 and I-9 show the stress gauge response when air breakdown is induced near the carbon surface by focusing the laser beam with a 5-cm focal length germanium lens. In Fig. I-8,

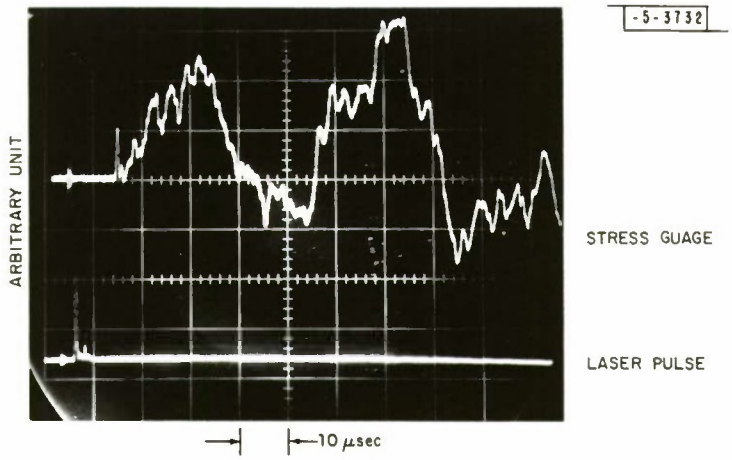


Fig. I-8. Stress gauge response (top trace) to air breakdown caused by a $CO_2$ laser pulse (0.5 J) (bottom troce) focused with a 5-cm focal length germanium lens. Stress gauge was located at focal point of lens.

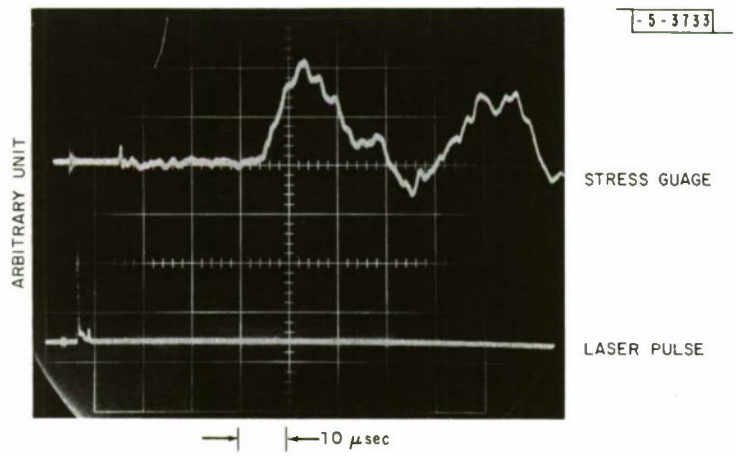


Fig. I-9. Stress gauge response (top trace) to air breakdown caused by a $CO_2$ laser pulse (0.5 J) (bottom trace) focused with a 5-cm focal length germanium lens. Stress gauge was lacated approximately 1.5 cm beyond focal point of lens.

the air breakdown was initiated at the carbon surface placed at the focal point of the lens. The stress gauge response shows a small peak caused by vaporization at the surface immediately followed by a pressure wave from the air breakdown region. In Fig. I-9, the stress gauge was placed approximately 1.5 cm beyond the focal point of the lens. Again the initial laser induced vaporization peak was observed, followed by a 29-μsec delay before the pressure wave from the breakdown region reached the target. The resulting velocity of 0.05 cm/μsec is about 1.5X the speed of sound in ambient air and is consistent with the speed of a weak shock wave.

Further development of the stress gauge is planned to extend the useful read time for vaporization induced compressive stresses. It is also planned to calibrate the stress gauge as a pressure gauge by exposing it to known step pressure increases in a detonation tube and monitoring its long time response.

J. E. Lowder

## D. LASER-INDUCED BREAKDOWN

The experimental program on laser-induced breakdown in air has concentrated on several aspects of the breakdown problem: the various ignition mechanisms, the rapid growth of the breakdown, and the interaction of the breakdown with the surrounding air. The basic experimental arrangement is similar to that described in Ref. 5, p. 11.

### 1. Threshold Measurements

In addition to the effects of aerosols on the breakdown thresholds[5] several other effects are currently under investigation.

#### a. Energy Thresholds

Laser pulses which exceed the flux density $2 \times 10^9$ W/cm$^2$ will break down air provided also that the energy density exceeds some threshold value. Canavan and Rockwood[6] established a relationship between the flux density and the time at which breakdown occurs. Their calculated threshold in terms of energy density along with our experimental results are shown in Fig. I-10. The data were fit at one point to the theory so that the agreement is somewhat misleading. A verification of the theory will require breakdown at times much shorter than we have yet been able to obtain.

#### b. Double Pulse Experiments

The ionization of the air produced by a breakdown was found to persist for times ~10 μsec. The effect of this ionization on the breakdown threshold of a second pulse was studied by focusing a second pulse near the first breakdown and delayed a time $\tau$ with respect to the first. The threshold of the second pulse as a function of this delay time is shown in Fig. I-11. As can be seen, the threshold is reduced by an order of magnitude for some 10 μsec.

The electrons become attached to $O_2$ in a time ~10 nsec. These negative ions behave as a density $N^-$ of impurity atoms with an ionization potential $X^- \approx 0.5$ eV. A simple model for the reduction in the threshold flux density can be obtained in this case from cascade theory and is

$$\frac{I_2}{I_1} = \frac{N_1}{N_2}\left\{1 - \left[1 - \frac{X^-}{X_o}\right]\frac{\ell n N^-}{44}\right\}$$

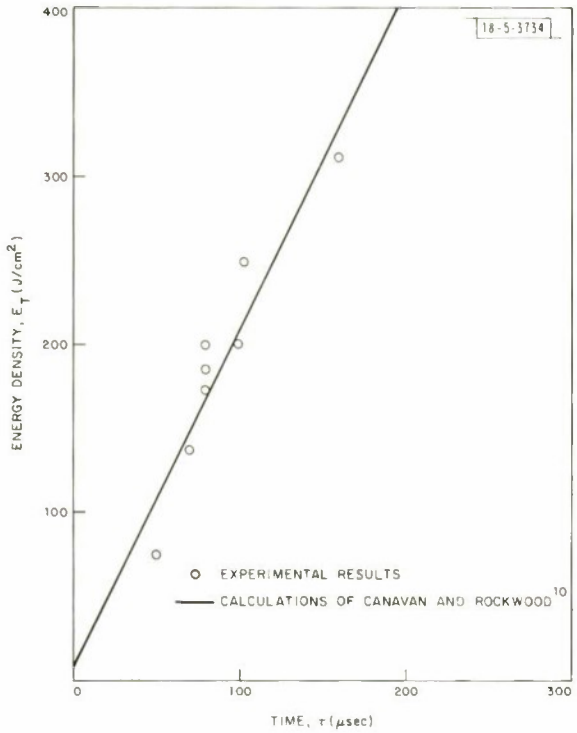


Fig. I-10. Energy transmitted through the focal volume before air breakdown as a function of the time of breakdown.

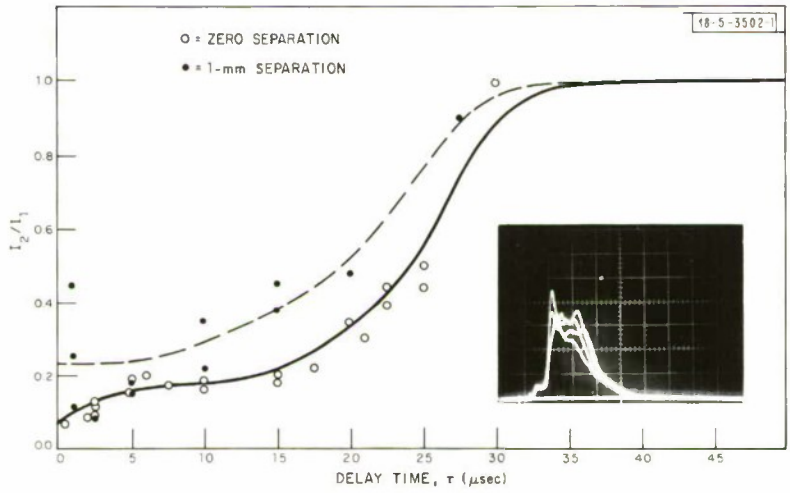


Fig. I-11. Energy threshold of a laser pulse fired at time T after a breakdown. Two curves correspond to a separation in focal volumes of 0 and 1 mm. Oscillograph shows ion probe current (5 μsec/div) at 1 mm.

where $I_2$ and $I_1$ are the threshold energies of the second and first pulse and where $N_1$ and $N_2$ are the neutral particle densities before and after breakdown and $X_o$ = 14 eV. The oscillograph in Fig. I-11 shows the ion current at 1 mm from the breakdown. The peak density obtained from this current is $10^{17}$ cm$^{-3}$. The above formula predicts a reduction of $I_2/I_1 \approx 0.1$. The breakdown also causes a reduction in the neutral density due to heating and expansion. Thus the two effects compete. For the data in Fig. I-11, ionization was the dominant effect, although we have also observed cases where there was an increase in the threshold for a short time after breakdown.

D. E. Lencioni
R. J. Hull
L. C. Marquet

## 2. Electrostatic Probes

Electrostatic probe studies of the interaction of the breakdown with the surrounding air have also been carried out. The experimental arrangement and preliminary results are described in Ref. 5, p. 13. A complete description will be published separately.

The perturbation in the probe signal (Fig. I-10 of Ref. 5) due to the shock wave can be explained in terms of a continuum probe theory[7] as follows: The probe current is related to the ion and neutral density by

$$I^+ \propto \frac{(N^+)^{3/4}}{N_o} = \frac{1}{(N^+)^{1/4}} \frac{N^+}{N_o} \quad .$$

Thus a compression which leaves the ratio $N^+/N_o$ constant will cause a dip in the probe signal.

The neutral particle density inside the shock front was obtained from the magnitude and width of this dip and the measured shock velocity. The results are shown in Fig. I-12 for probe signals obtained at various distances from the breakdown. The solid curve corresponds to a "snow plow" model in which all the particles inside a sphere of radius r are contained inside the shock-front shell. The results for this breakdown (E = 0.2 J) show that a strong shock wave theory can hold out to $r \approx 0.5$ cm. This is consistent with the requirement that the pressure behind the shock be much higher than atmospheric.

The photoionization density was found to decrease exponentially with distance away from the breakdown. The e-folding distance characterizes the distribution of x-ray energies involved and should be a strong function of the plasma temperature. The variation with pulse energy of the photoionization at two distances from the breakdown is shown in Fig. I-13, while the corresponding e-folding length $\lambda$ is shown in Fig. I-14. These data imply that although the amount of photoionization increases rapidly, the electron temperature increases only slightly with pulse energy.

We are presently developing an experiment which will check these conclusions by a direct measurement of the x-ray distribution.

D. E. Lencioni

## 3. High-Speed Photography

High-speed photography has been used to measure the velocities of the luminous fronts and blast waves created in laser-induced air breakdown. The measured velocities provide information on the temperature of the plasma and overpressure generated by the blast wave. The results are given below.

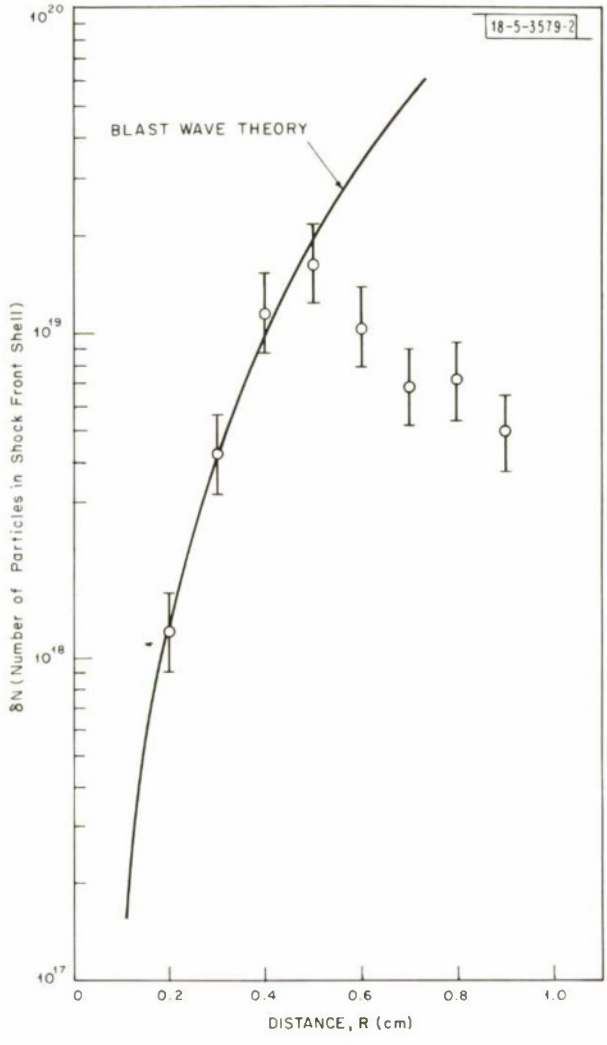


Fig. I-12. Number of particles in shock-front shell far o 0.2-J pulse energy. Data were obtoined from the dip in probe current caused by the shock front. Solid curve corresponds to o strong blast wave ar "snow plaw" model in which all porticles originally within o sphere af radius r are cantained in the shell.

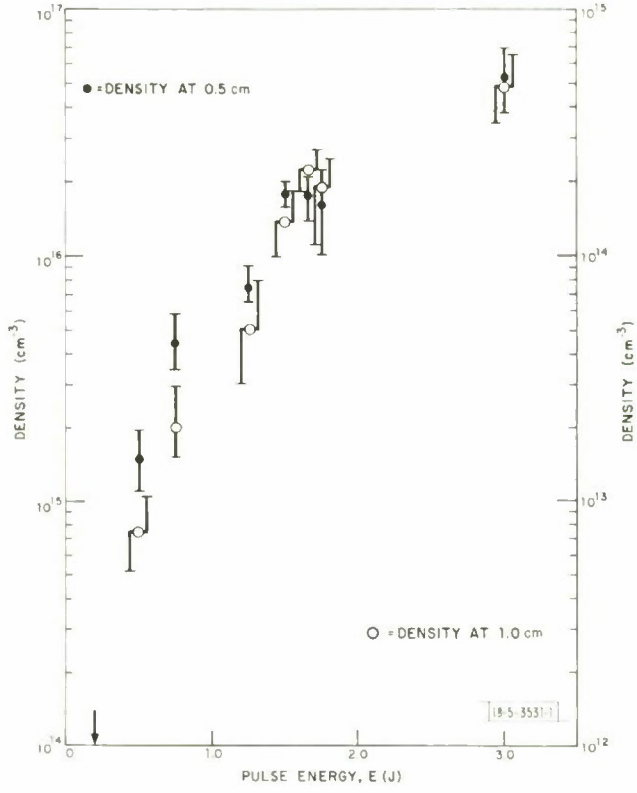


Fig. I-13. Ion density produced by photoionization as a function of pulse energy. Arrow indicates energy at breakdown threshold.

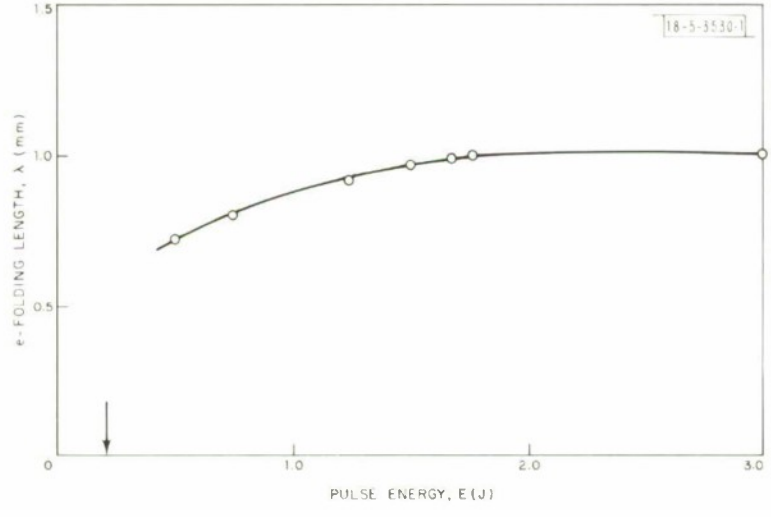


Fig. I-14. E-folding distance for spatial distribution of density as a function of pulse energy. This should be a sensitive function of electron temperature in the breakdown. Arrow indicates energy at breakdown threshold.

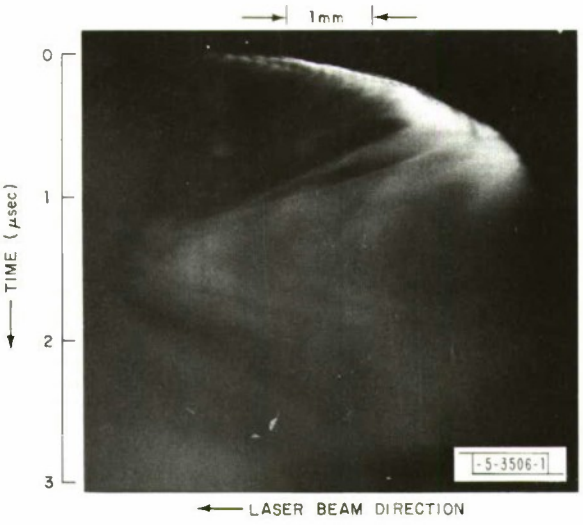


Fig. I-15. Streak photograph of laser-induced breakdown. Herring-bone pattern apparent in the shock front is attributed to a modulation of laser intensity. Measured 15-nsec period of modulation agrees with mode-locking period of 2.2-m-long laser cavity. Some modulation was observed in laser beam intensity when examined with a fast 10.6-μm detector.

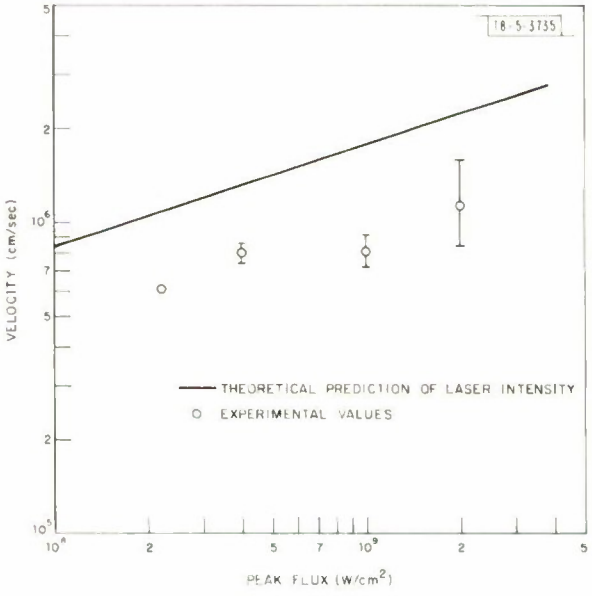


Fig. I-16. Plot of measured initial velocity of luminous front vs peak intensity of laser beam. Solid line is a theoretical prediction of velocity vs laser flux. Breakdowns were initiated off a carbon block in order to obtain data below the air breakdown threshold.

a. Luminous Front Streak Photography

High-speed streak photographs were taken of the development of the luminous front generated by the air breakdown. At sufficiently high flux levels ($I > 2 \times 10^9$ W/cm$^2$), breakdowns occur in laboratory air at normal pressure. A typical streak reeord of such a case is shown in Fig. I-15. The laser used is the helical TEA $CO_2$ laser described earlier[5] which produces 0.2 J in a pulse of 300 nsec. A typieal plasma plume consists of a narrow region of high luminosity which advanees toward the laser. The measured initial velocity of the front is $1.6 \times 10^6$ cm/sec for the conditions under which Fig. I-15 was taken. This velocity is approximately that predicted for a laser-supported detonation (LSD) wave.[8,9] An LSD wave is generated when the laser flux is absorbed within a thin layer $\ell$ of the shock front, wherc $\ell$ is small compared with the radius of the laser beam. The luminous front travels as a one dimensional shock wave whose velocity v is given by

$$v = \left[\frac{2(\gamma^2 - 1)\, I}{\rho_o}\right]^{1/3} \qquad (I\text{-}1)$$

where $\gamma$ is the ratio of specific heats of the gas at the temperature of interest, I is the laser intensity (ergs cm$^{-2}$ sec$^{-1}$), and $\rho_o$ is the density of the ambient gas. At the breakdown threshold for air, Eq. (I-1) predicts a velocity of $2.3 \times 10^6$ cm/sec. The heating of the gas $\epsilon$ is given by[8]

$$\epsilon = \frac{\gamma v^2}{(\gamma^2 - 1)(\gamma + 1)} \quad .$$

From the velocity we obtain a value of $\epsilon$ which corresponds to a temperature of about 2 eV for this case.

The velocity dependence of the front on intensity was studied at intensities below threshold by initiating breakdowns off a carbon block oriented at 45° to the laser beam. At identical flux levels, the appearance of the streak records is similar to the air breakdown cases and the luminous front velocities are the same. Figure I-16 is a plot of the measured initial veloeity of the front vs the peak intensity of the laser pulse. The peak intensity occurs within the first few hundred nsec of the pulse. The spread of the experimental data is shown on the plot. The solid line is a plot of Eq. (I-1) for the measured incident laser intensities. The experimental values are low because Eq. (I-1) requires the use of the absorbed flux rather than the incident flux.

b. Shadowgraph Measurements

The presence of a shock wave after the self-luminosity of the plasma has died away was observed by using the shadowgraph technique. The breakdown region was backlighted with a pulsed argon ion laser focused down to a point. The argon laser pulse at 4880 Å was 40 μsec long. The breakdowns were ereated by a $CO_2$ laser operating at approximately 3-J output with a total pulse length of 5 μsec. Both streak and high speed framing shadowgrams were taken.

Figure I-17 shows a sequence of frames taken at 0.75-μsec intervals. The shock front appears as a white line. This sequence shows the growth of a spherical shoek front.

Figure I-18 is a typical streak record of the growth of a laser induced shock. The streak camera slit was oriented perpendicular to the direetion of travel of the $CO_2$ laser beam. The position of the shock appears as a pair of white lines.

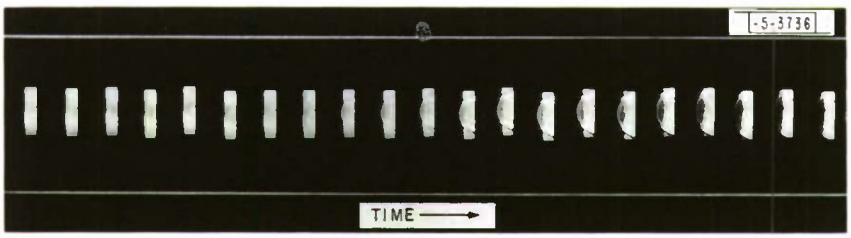


Fig. I-17. Sequence of frames taken at 0.75-μsec intervals of backlighted shock front for laser induced air breakdown.

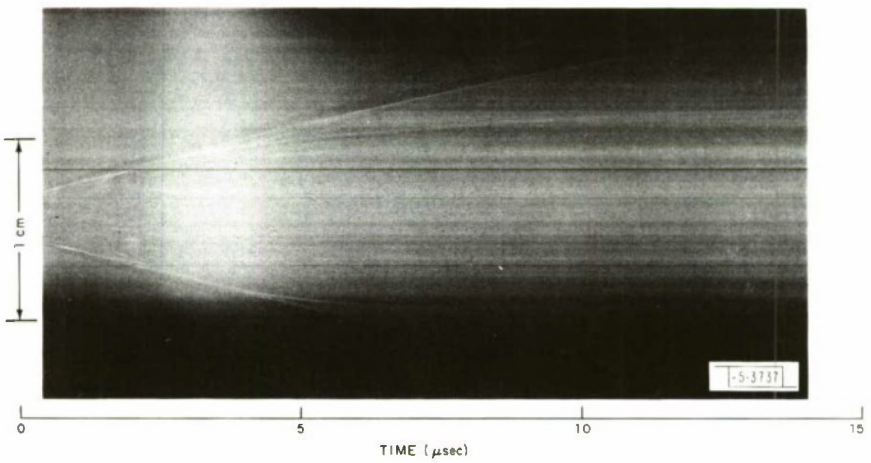


Fig. I-18. Streak shadowgram showing development of a blast wave for a laser produced air breakdown.

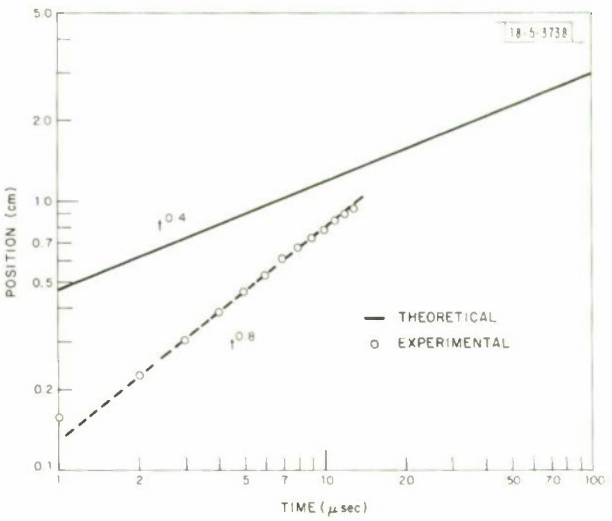


Fig. I-19. Position of blast front as a function of time for a laser induced breakdown in air. Dashed line is a fit to experimental points. Solid line is the prediction of spherical blast wave theory for 3-J input.

In Fig. I-19 we plot the position of the shock as a function of time. Time is measured from the onset of luminosity of the gas breakdown. The circles are the experimental points which depend on time as $t^{0.8}$. Intense spherical blast wave theory predicts that the radius should go as $t^{0.4}$. The solid line is a plot of the equation[10]

$$R = (E/\rho)^{1/5} t^{2/5} \quad ,$$

where E is the energy absorbed and $\rho$ is the density of air. The fit is not particularly good. However at long times the experimental points are beginning to show a dependence on time weaker than $t^{0.8}$. The disagreement is probably due to the fact that the energy is not deposited instantaneously at a point, but rather is spread in several μsec over a column of gas approximately one cm in length by the LSD wave mechanism discussed above. Furthermore, because of a limitation of our field-of-view in these experiments we were able to follow the growth of the blast wave for a time not much longer than the time to deposit the energy by the laser beam. If a better fit to theory can be obtained at longer times, this technique will provide a useful estimate of the fraction of the laser energy used in generating the blast wave.

R. J. Hull
D. E. Lencioni
L. C. Marquet

## E. INTERACTION OF A 10.6-μm LASER PULSE WITH FOG

Previous reports* have described the fragmentation and evaporation of single fog droplets upon irradiation with a submicrosecond pulse from a 10.6-μm laser. In those experiments we used the tri-scopic camera system to photograph the liquid droplet as it was exploding, that is, we studied the early stage of the explosion. Now we have extended the study to a later time regime by examining the vapor "blob" produced by the evaporation of a single droplet. We have also continued the calculations of the effects of such vapor blobs on the propagation of a 10.6-μm beam through a hole bored in a fog by a precurser pulse of 10.6-μm radiation.

* Ref. 11, pp. 19-25 and Ref. 5, pp. 7-10.

## 1. Single Droplet Experiments: Schlieren Photography of Vapor Blobs

### a. Deseription of Experiment

A sehlieren photography system has been built using a pulsed xenon laser as a light souree, as shown in Fig. I-20. This is a small, sensitive system with a magnifieation of 10X. The sensitivity is $\sim 3 \times 10^4$ (Ref. 12). The xenon laser has a pulse length of 0.3 μsee, FWHM (full width at half maximum). A droplet generator, which is positioned above the plane of the diagram in

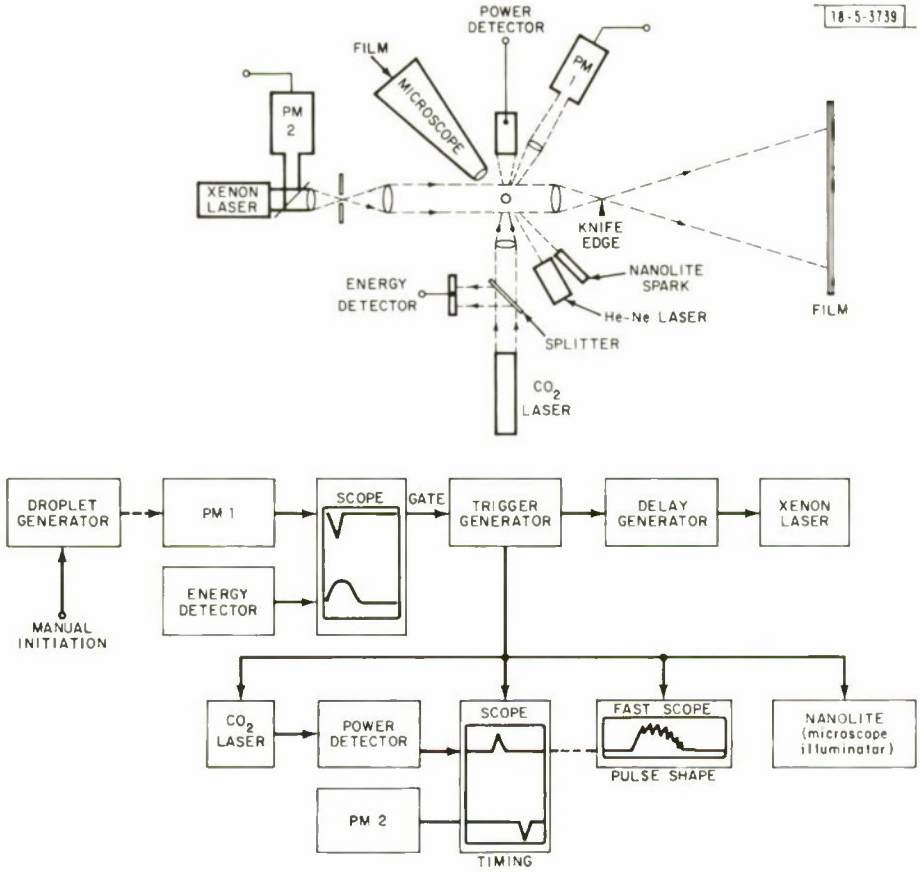


Fig. I-20. Schlieren systems — schematic diagram.

Fig. I-20, injeets a single droplet into the optieal volume of the system. This droplet is "pieked up" by a photomultiplier that deteets He-Ne laser radiation scattered by the droplet. The droplet must be in foeus in order to trigger the sequenee of events: First the droplet is photographed at 50X (for measuring its size); then it is irradiated by the 10.6-μm pulse from the $CO_2$ laser; and finally the sehlieren film is exposed by the pulse from the xenon laser.

The sehlieren photographs ean be taken at any time from a fraetion of a μsee to several msee after the $CO_2$ laser pulse, but the usual delay times are 2 to 100 μsee. The power and the energy of the 10.6-μm laser pulse are measured on eaeh shot; the pulse shape is monitored on a fast seope. A dual-beam seope is used to display the $CO_2$ laser pulse and the xenon laser pulse (detected by a photomultiplier); these traees are used to measure the elapsed time between the two pulses.

The $CO_2$ laser pulse is mode locked. The pulse envelope can be varied from a full-width at half-maximum of ~150 nsee to ~400 nsec. The fine-structure shows peaks 15 nsec apart. At the droplet position the laser energy density is 10 $J/cm^2$.

The preliminary experiments were performed on droplets of 25 to 75 μm radius in an effort to reveal the dynamics of the liquid-vapor explosion phenomena, even though our main interest is with smaller droplets. We have now started studying droplets of 5 to 25 μm radius.

b. Experimental Results

The most obvious phenomenon is a readily observable shock wave expanding outside the volume of the vapor blob (Fig. I-21). This shock wave expands with a radial velocity between Mach 1 and Mach 2 in the time period 2 to 20 μsec (perhaps faster at earlier times). For example, a shock front velocity of Mach 1.7, averaged over the first 2.7 μsec, has been measured. This velocity was observed for droplets of 35 μm radius.

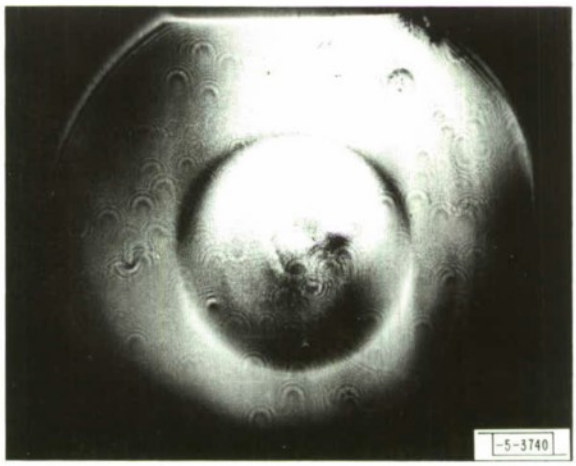


Fig. I-21. Hot vapor blob (dumbbell shope) surrounded by shock wove. Time = 5.0 μsec after the 10.6-μsec laser pulse. Loser pulse traveled from left to right. (Schlieren knife-edge was horizontal.)

In Fig. I-21 the hot vapor blob can be seen at the eenter of the shock sphere. For these large droplets the vapor blob is approximately spherical only at the earliest times when vaporization may not even be complete. Then it develops into a mushroom shape with the "stem" growing out of the back of the sphere approximately in the direction of the 10.6-μm laser pulse. At later times, 10 to 20 μsec, a second sphere grows at the back end of the stem, forming a dumbbell shape. The rate of expansion in this axial direction is about twice as great as the expansion rate in a direction perpendicular to the 10.6-μm pulse axis. This observation is consistent with our previous findings, where we observed front-surface heating and back-surface spallation for droplets greater than ~15 μm radius. This asymmetry should be less pronounced, or perhaps nonexistent, for droplets of radius <15 μm, where volume heating would prevail.

The expansion velocity of the hot vapor blob in the axial direction is ~0.13 mm/μsec for the first 10 μsec. This value is the same as the expansion velocity of the exploding liquid previously reported. After this, the expansion rate is slower: about 0.015 mm/μsee in the time period 10 to 100 μsec (axial direction). These measurements were for droplets of 50 μm radius.

c. Energy Deposited Calculated from Schlieren Photographs

An important quantity in the study of the evaporation of water droplets is the energy which is absorbed beyond the energy required to evaporate the droplet. It is this excess energy that determines the seeing conditions through evaporated fog.

The minimum amount of excess energy is given by slow heating leading to evaporation of the water at 100°C. This limiting case gives rise to a temperature increase of the water vapor above ambient by an amount of 75°C.

Fast heating leads to a shattering of the water droplets and subsequent evaporation accompanied by a shock wave. Under these conditions, more energy will be absorbed than for the slow heating case. The experimental observations with the schlieren system permit two different evaluations of the excess energy deposited by a laser pulse.

Energy of an Exploding Water Droplet:– The shock wave observed with the schlieren system can be used to determine the explosive energy. The yield of an explosion can be calculated from arrival time and distance measurements of the shock wave using the semiempirical relationship of Kinney.[13] We calculate a scaled time $t_x$ from the measured time of arrival $t_s$ of the shock front at the radial distance $r_s$. The yield of the explosion is then given by

$$W = 4 \times 10^9 (t_s/t_x)^3 \text{ J} \quad .$$

Using this formula we have calculated the yield from the experimental data. The explosive yield from the shot presented in Fig. I-21 is $5 \times 10^{-4}$ J.

Heating of Surrounding Air:– The same schlieren pictures can be used to measure the heating of surrounding air. The schlieren pictures are taken with a light source having the wavelength in the visible. The index of refraction, n, of air can be considered the same at this wavelength as at the wavelength of the $CO_2$ laser. For air blobs sufficiently larger than the $CO_2$ wavelength, diffraction can be neglected and, therefore, the ray optics for the two wavelengths can be considered identical.

The exposure, E, of the schlieren film is mapped with a vidicon scanning microdensitometer. The contrast defined by $C = (E - \bar{E})/\bar{E}$, has a maximum value, $C_{max}$, which is related to the index of refraction: $C_{max} \approx 2\, s\, \Delta n/n$, where s is the sensitivity of the schlieren system.

The schlieren picture in Fig. I-21 gives $C_{max} = 0.1$ for the smooth part inside the shock wave. Using a sensitivity $s = 3 \times 10^4$, we obtain a temperature of the air sphere of $\Delta T_a = 1.5$°C above ambient. From this temperature one can calculate the energy stored inside the shock wave to be $1.8 \times 10^{-4}$ J. The irregular part in the center, corresponding to the water vapor blob, gives a contrast about 15 times larger than the smooth part of Fig. I-21. But with a volume about 20 times smaller, the total energy stored inside the irregular pattern is about the same, $\sim 2 \times 10^{-4}$ J.

There is a reasonable agreement between the energies calculated by the two methods. It should be pointed out that the water droplet size did not enter into the calculations.

The energy absorbed goes into heat of evaporation and into excess energy available for heating the air. For a droplet of 35 μm radius the evaporation energy is approximately equal to the excess energy.

## 2. Calculation of Spread for Laser Beam Traversing a Hole Bored in Fog

We shall consider the deflection of a laser beam traversing a hole that has been bored in a fog by a pulse from a 10.6-μm laser. We take the case of a fog with the size distribution shown in Fig. I-22. This is a heavy fog, with 420 droplets/cm$^3$ and a liquid water content of 0.5 g/m$^3$. The shape of the distribution function corresponds closely to that measured for the fog of 6 October 1971 in Lexington, Massachusetts although the Lexington fog was less dense, ~4 droplets/cm$^3$.

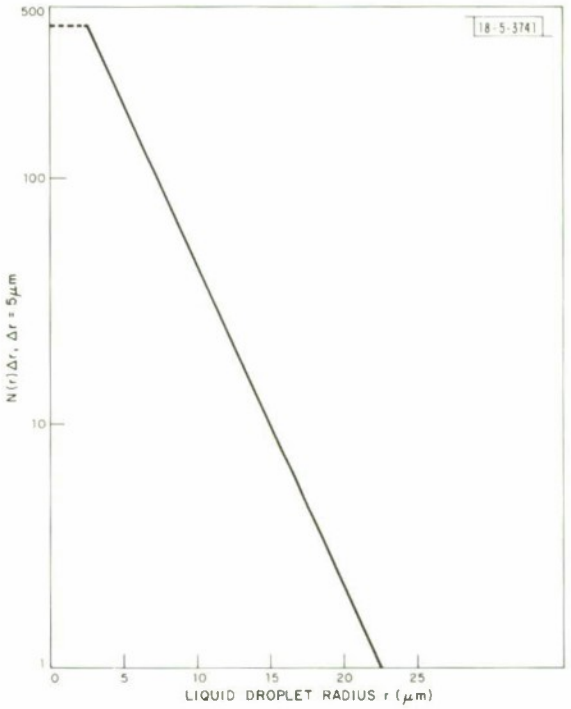


Fig. I-22. Fog droplet size distribution.

We assume that each droplet is completely vaporized by a single, submicrosecond pulse and that the vapor then persists as a hot sphere that expands explosively at 100 μm/μsec for the first 10 μsec and then at 10 μm/μsec for the next 90 μsec. We carry the calculations out to 100 μsec after the pulse. The air within the dimensions of the vapor sphere is heated by the vapor in the sphere. The energy available for heating is the energy that is stored in the hot vapor. All the water in a droplet is converted to vapor at an initial temperature of $\Delta T_i$ above ambient. In this example we assume $\Delta T_i = 100°C$. This is 25°C above the evaporation temperature. We use the following expressions:

$$\epsilon = \frac{\Delta n}{n} = \frac{\Delta T_i}{2T_o}\frac{r^3}{r_v}$$

$$\Theta_r = N_r^{1/2} L^{1/2} A_v^{1/2} \epsilon = \frac{\sqrt{\pi}}{600} N_r^{1/2} L^{1/2} \frac{r^3}{r_v^2} \Delta T_i$$

$$y_r = \frac{2}{3}\,\theta_r L = 2 \times 10^{-3}\, L^{3/2} \Delta T_i N_r^{1/2}\, \frac{r^3}{r_v^2}$$

$$y_{total} = \left( \sum_r y_r^2 \right)^{1/2}$$

where

$\epsilon$ = angle of deflection in a single event

n = index of refraction

$\Delta T_i$ = initial temperature above ambient to which vapor has been heated

$T_o$ = ambient temperature

r = radius of liquid droplet

$r_v$ = radius of vapor sphere at time t

$\theta_r$ = rms angle of deflection at distance L (in rad)

$N_r$ = number density (per $cm^3$) of droplets having radius r

L = path length through fog

$A_v = \pi r_v^2$

y = rms displacement at distance L (in cm).

In Fig. I-23 we show the values of $y_r$ and $y_{total}$ as a function of time.

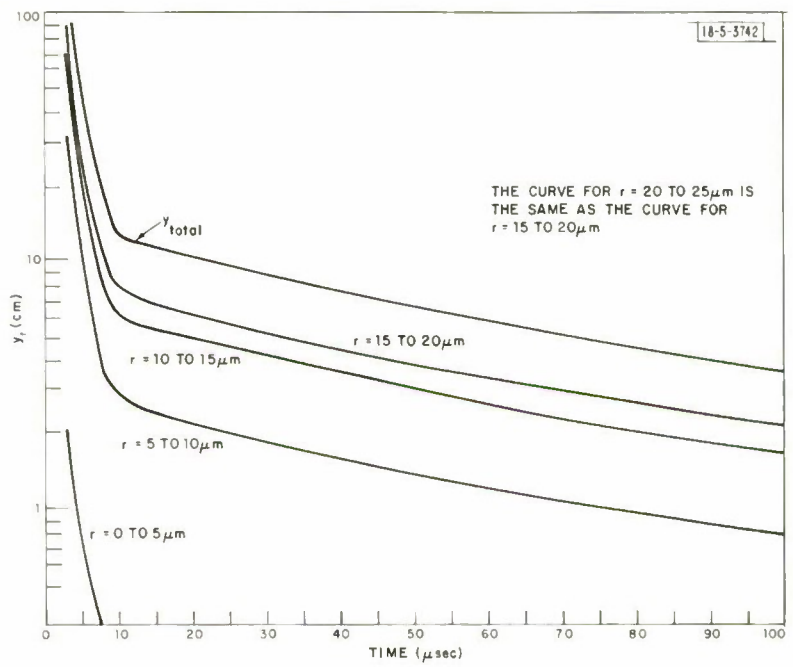


Fig. I-23. Spreod resulting from scottering by vopor "spheres" produced in L = 1 km of fog by a 10.6-μm laser pulse.

The radial spread of the beam at 100 μsec after the pulse is 3 cm after traversing a path of 1 km. This is an angular spread of 30 μrad at this distance. Even for this very heavy fog, the radial spread in a 1-km path would be ~10 μrad in 300 μsec. For a lighter fog, such as the Lexington fog mentioned above, the radial spread in a 1-km path would be 3 μrad in 100 μsec.

If we want to know the spread at a point beyond a patch of fog, we need to know the angle of deflection as the beam emerges from the fog. This angle, Θ, can be obtained from the $y_{total}$ value in Fig. I-23 by multiplying by 1.5/L.

P. Kafalas
J. Herrmann

## F. PULSED LASER DEVICES

### 1. 500-J Electron-Beam Excited Laser

The EDL laser effort now has as its main thrust the construction of an electron beam controlled $CO_2$ device, designed to deliver 500 J of optical energy. A large area (15 × 104 cm) electron gun is under procurement, and it is expected to give up to 30 mA/cm$^2$ into the laser medium at 200 kV. The active volume of the lasing medium will be about 20 liters. It is expected to outcouple 500 J in a single mode in a 1- to 100-μsec pulse interval. The actual minimum pulse interval will depend on the maximum current density obtained from the large area (15 × 105 cm) electron gun now under procurement. The device design is now being finalized and our expectation is to have it operational by mid-summer 1972.

R. J. Carbone
A. J. Morency

### 2. Small Scale Electron-Beam Excited Laser

Previous works[14,15] have demonstrated the feasibility of seeding a laser medium with electrons by passing a high energy electron beam through it. Ionizing collisions by the primary current beam, $J_e$, produce essentially zero-energy secondary electrons. By this mechanism a desired electron density, $n_e$, can be established without breaking down the gas with a discharge. A set of sustaining electrodes can be used to accelerate the secondaries to a given desired energy for optimum collisional cross section with the gas molecules (i.e., the E/P with peak molecular cross section). Such a system could be uniformly excited and would therefore be scalable to a large volume device.

A small electron-beam-excited laser cavity has been constructed using an RCA type J15034 electron gun as a primary beam source. The gun is capable of supplying at least 20 mA continuous stream through a 1.3-cm-diameter output window of 0.0003-inch-thick titanium foil. Its purpose is to make a small electron-beam excited laser in which to test theories for a larger scale device, and to perform studies of the parameters of a medium excited in such a fashion.

Figure I-24 is a sketch of the experimental configuration. The electron beam, delivered from a thoriated-tungsten cathode is preaccelerated by a 1-kV gate pulse which determines the pulse length (~3 μsec) and shape of the beam. The beam is then accelerated through a 75-kV drop (being focused by an intermediate grid) into the foil. We have also provided a defocusing capability for the gun to permit measurements as a function of current density. The beam passes into a cavity (of about 25-cm maximum depth) between a pair of sustainer electrodes. The electrodes are a pair of rounded aluminum balls with flattened segments facing each other. The axes of these electrodes are transverse both to the optical path and the primary beam.

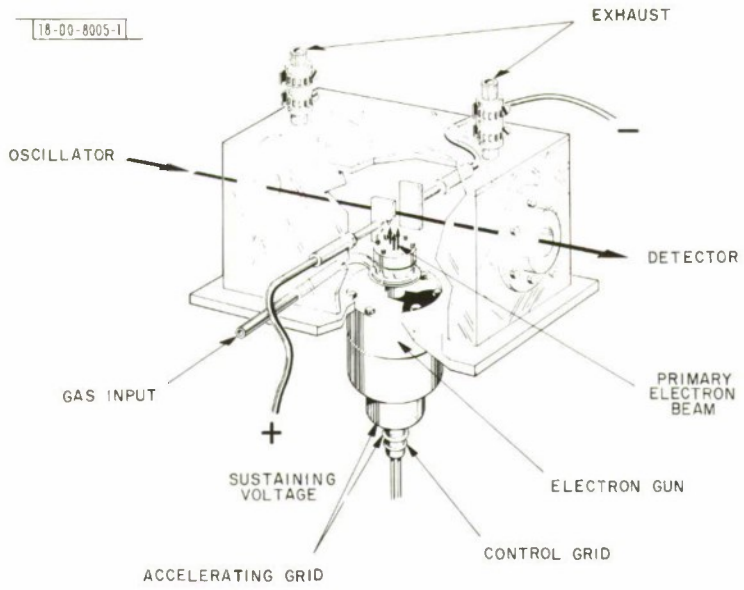


Fig. I-24. Schematic of small electron-beam excited laser. Primary electron current passes through the transverse sustaining voltage field region. Orthogonal to these axes is the optical gain axis.

An estimate of the energy capacity may be made for our system with a $CO_2$-$N_2$-$H_2$ mixture totaling 760 torr. Such an analysis can be simply extended for other systems. The rate of electron ion-pair production, $P_{ion}$, is given by

$$P_{ion} = \frac{1}{U_p} \left(\frac{dE}{dx}\right)_{E_o} J_e$$

where $U_p$ is the average energy lost by a primary electron per collision ($U_p \approx 34$ eV), and $(dE/dx)_{E_o}$ is the rate of energy loss per unit length of the primary beam in the gas. The rate equation of the electron density is given by

$$\frac{dn_e}{dt} = P_{ion} - \alpha_R n_e n_{ion} - \beta n_e$$

where $\alpha_e$ is the recombination coefficient, $n_{ion}$ is the ion density and $\beta$ is the attachment coefficient of the medium. For this system, equilibrium is quickly reached in a time short compared to our pulse lengths, and the electron attachment is negligible compared to electron recombination. Since the secondary electron density and ion density must then be equal,

$$n_e = \sqrt{\frac{P_{ion}}{\alpha_R}} \approx 10^{13}/cm^3$$

where the last term has been evaluated for our system. The energy output of the laser is then given by

$$n_{photon}(h\nu) = \Theta n_e [ev_d \tau_p E] \quad , \tag{I-2}$$

where the term in brackets represents the average energy transferred per secondary to the $N_2$ molecules and $\Theta$ is the percentage of this energy transferred to the 001 level of $CO_2$ (thereby utilized in lasing). In brackets we have the product of the electron charge e, the drift velocity $v_d$, the pulse length $\tau_p$ and the electric field E. We use values from McDaniel[16] and choose $E/p \approx 7$ V/cm torr to optimize the electron transfer to nitrogen. We choose our maximum pulse length by limiting the gas temperature rise to a factor of two. The gas heating arises predominately from the resistive heating by the secondary current:

$$E_{dissipation} = 1/2\ \tau_p J_{sec} \times E = 1/2\ \tau_p (n_e e v_d)\ E$$

$$= 3/2\ n_{gas} k \Delta T_{gas} = 3/2\ n_{gas} k T_{gas} \quad .$$

One finds for our system the pulse length should not exceed $\tau_p \cong 1\ \mu$sec, and by substituting this and other appropriate values into Eq. (I-2), assuming, $\Theta \approx 0.2$, we find that our small system is capable of about 1/4 J in the $CO_2$ system.

We have not yet observed lasing in our system but have had excellent success in the early experiments. In a 300:35:5T mixture of $He:SF_6:H_2$, we have found a voltage of about 20 kV for a spacing of about 3 cm to produce a pulsed discharge. However, by applying the primary electron beam we were able to produce a discharge as low as 6 kV. This discharge filled the region between the flat sections of the electrodes. Observations are under way of the temporal behavior of the primary and secondary beams inside the medium for various mixtures. These experiments should give us information on the recombination coefficient and parameters that are necessary in the construction of larger devices.

H. Granek

### 3. Chemical Laser Devices

Studies of the spatial and temporal dependence of the gain of a pulsed HF laser were made and were compared with those for $CO_2$ lasers. Results of these experiments are described in detail in Ref. 17 and have been submitted for publication in the IEEE Journal of Quantum Electronics.

Summarizing these results, the propagation in space of a locally excited gain medium was observed to be comparable for the two lasers, while the time developments were vastly different. The extremely fast gain decay rates observed in the HF laser were shown to be a serious detriment to efficient high power CW or long-pulse operation.

Efforts were continued to increase the output energy of the 75-cm HF pin-laser. A substantial increase was achieved by initiating the chemical reaction with a Field Emission Corporation Marx bank pulser. The maximum energy thus obtained has been 360 mJ/pulse, as compared to 140 mJ/pulse with the previous pulsing network. This increased output, which had been predicted,[18] is attributed to the extremely fast (50 nsec) excitation pulse which is short compared with the HF vibrational relaxation time (~1 μsec). This results in higher efficiency than with the 1-μsec pulse previously obtained by discharging a single capacitor through a triggered spark gap.

Studies of electron-beam initiation of chemical lasers were begun, using a Field Emission Corporation Febetron 706 electron beam source which produces a 10-kA, 3-nsec beam of 600-keV electrons. As shown in Fig. I-25, the electrons pass into the laser tube through a titanium foil, where they ionize the molecules of the laser medium, thus producing secondary electrons. These

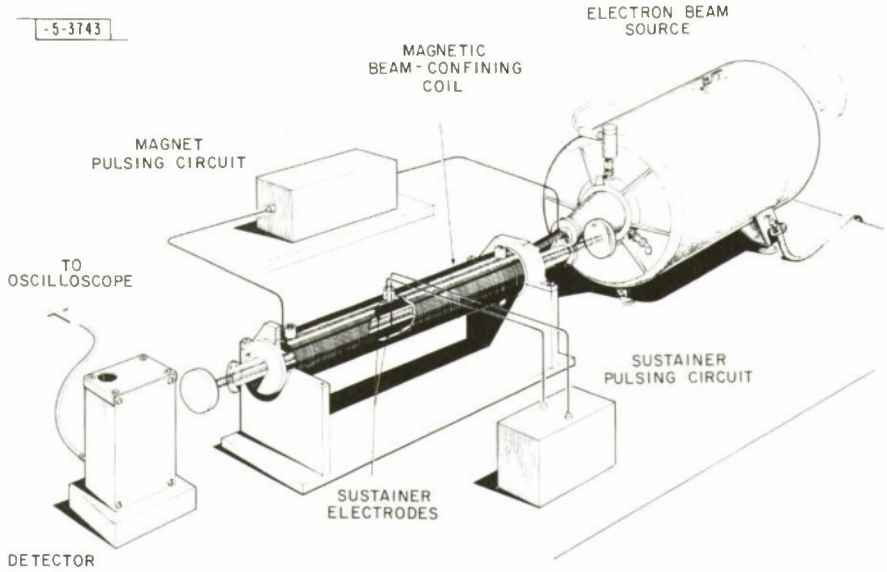


Fig. I-25. Electron beom loser.

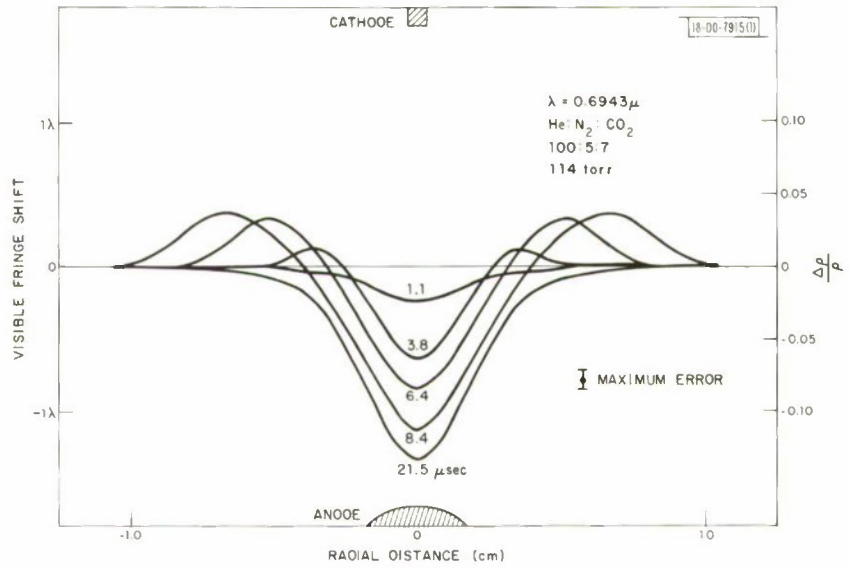


Fig. I-26. Time evolution of the index os o function of rodiol position.

electrons are accelerated by a sustaining electric field which imparts to them the required energy to initiate the chemical reaction. To date, this device has only been operated without the sustaining field on the $SF_6$-$H_2$ system. Marginal oscillation has been observed.

S. Marcus
R. J. Carbone

## G. MEDIUM DIAGNOSTICS OF LASER DEVICES

Continued progress has been made on the medium diagnostics of the transverse excited pin laser which were reported earlier.[5] Observations were made at several different total pressures for a given mixture of helium, nitrogen and carbon dioxide. Interferometric data are presented for one set of conditions. A comparison is made of the distribution of the index of refraction in the medium as a function of time as compared with the vibrational temperature distribution or gain profile measured elsewhere.[17] We observed that the spatial distribution of the energy in the medium due to the discharge is much broader than the observed optical flash in the individual pin-to-plane discharges. Indeed, our spatial extent is comparable to the inversion region measured by gain experiments. Lasing did not occur during the actual interferometric observations. To relate the time of observation to the time when lasing would normally occur, cavity mirrors were installed and the 10.6-μm pulse output was measured relative to the beginning of the current pulse. We can thus relate the temporal development of the index of refraction distribution to times appropriate for lasing, typically the initial 1- to 3-μsec interval after the beginning of the current pulse. The temporal dependence of lasing on the gas mixture and total pressure was found to be negligibly weak. Interferometric measurements were extended to about 40 μsec to follow the index distribution to its final equilibrium state in order to provide data for future double pulsing experiments.

Figure 1-26 shows the visible fringe shift in the medium as a function of transverse dimension and time. We observe that the medium undergoes negative fringe shifts in the central region, where the initial surge of energy is added and the medium becomes rarefied, and positive fringe shifts in the outer region. If one compares the widths of the translational heating measured by our experiment with the vibrational heating (gain) measured by Marcus and Carbone,[17] one observes good agreement between the two processes in the transverse excited pin devices.

The general behavior observed in the interferograms can be predicted if we take as a model for energy dissipation in a TEA laser medium N pins separated by distance $\Delta Y$ located along the Y axis. At each pin we allow a cylinder (with Z axis symmetry) of power density to be injected. At the $K^{th}$ pin, the spatial distribution of the injected power density is

$$Q_K(x, y) = Q_o \, e^{(x/a)^2} \, e^{-(y-K\Delta y/a)^2} \quad .$$

$Q_o$ has the dimensions of $W/cm^3$, and a is the 1/e point of index change.

The hydrodynamic response of the laser medium to the heat source is[19]

$$\delta n = \frac{(n-1)\, V_s^2 t^3 \nabla_r^2 Q(x, y)}{6\rho c_p T}$$

Here n is the index of refraction; $V_s$, the medium sound speed; $\rho$, the density; $c_p$, the specific heat; and T, the temperature. The $t^3$ growth of the density change is valid only for times short compared with the time for a sound wave to traverse the characteristic dimension of the cylinders into which the energy is injected. For our geometry, this time is approximately 4 μsec. Summing the effects of each pin on the refractive index one deduces the expected fringe shift in the interferometer as:

$$F = \frac{N\sqrt{\pi}(n-1)\,Q_o t^3 V_s^2\, e^{-(x/a)^2}}{3\rho c_p T a \lambda}\left(\frac{x^2}{a^2} - 1\right) \quad . \tag{I-3}$$

Here F is the shift in fractions of a fringe spacing and $\lambda = 0.69 \times 10^{-5}$ cm.

After some time (in this experiment approximately 20 μsec), the hydrodynamic effects have had a chance to equilibrate, and the fringe pattern should stop growing and remain stationary until conduction effects become important.

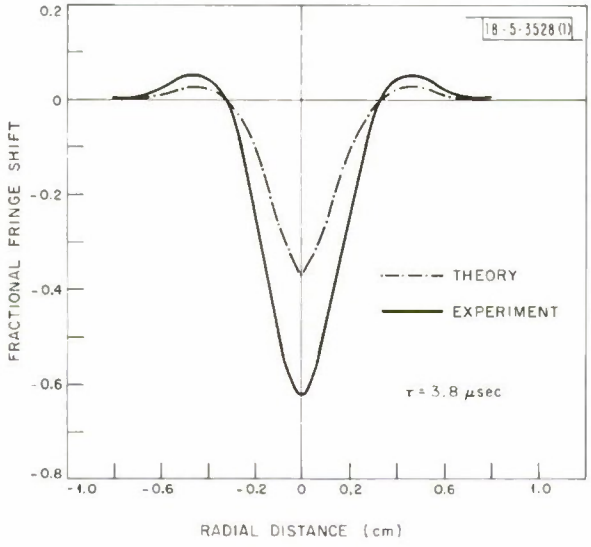


Fig. I-27. Fractian fringe shift (λ6923 Å) as a functian af radial position at 3.8 μsec after initiatian af the current pulse.

Figure I-27 shows a calculation of the theoretical fringe profile as given by Eq. (I-3) compared with the experimental curve taken from Fig. I-26 at t = 3.8 μsec. The general features of the two curves agree well enough to indicate the role of the hydrodynamic assumptions, although the theoretical curve is approximately a factor-of-2 smaller than the experimental one. This agreement is acceptable in light of some of the assumptions made in deriving Eq. (I-3) (i.e., that the energy is injected at constant power) which are not met experimentally.

Our data suggest that the extent of disturbance of about 6 mm in diameter (compared with ~1.5 mm of the observed flash), the relative spatial smoothness, and the smallness of the index perturbation would make the transverse pin excited laser a good single-pass laser amplifier. However, possible phase distortion could be very severe in the pin laser oscillator.

H. Granek
H. Kleiman
R. W. O'Neil

## H. SEALED-OFF CARBON MONOXIDE LASERS

Our work on CO lasers continued along three general directions.

(1) Construction and evaluation of lasers and components at hand.

(2) Design of new lasers with enhanced capabilities.

(3) Determination of the physical and chemical processes in sealed-off CO lasers.

We have constructed and evaluated several grating controlled lasers with a 150-cm semi-confocal cavity configuration. The output characteristics of these lasers were found to be highly reproducible both from one laser to the other, and also as a function of time (over several months) in any one of the lasers tested so far. Nearly two hundred individual vibrational-rotational transitions have been observed between 5 and 6.5 μm. A more systematic evaluation will be performed with a higher resolution spectrometer to be received in January 1972.

The resettability of the new grating control mechanism exceeded all expectations. Any one of the laser lines could be reset without the use of an auxiliary spectrometer, and the rms error in resettability was about $0.1\ cm^{-1}$. It should be noted that $0.1\ cm^{-1}$ corresponds to a grating angular error of less than 5 arc sec in the present design.

Sealed-off operation of CO lasers was also obtained by introducing krypton or argon, instead of xenon, into the gas fill. In this fashion, the operating temperature of the CO lasers could be reduced to below the freeze-out temperature of xenon.

At ARPA's request, one of the CO lasers has been transported to Ohio State University in order to obtain high resolution absorption data.

We have commenced the study of saturation resonance phenomena with CO lasers. In one series of experiments we have obtained preliminary results on the Lamb-dip in CO lasers. Dips on the order of 15 percent were obtained without any difficulty.

Figure I-28 shows the evolution of the Lamb-dip in a stable, sealed-off, $TEM_{00q}$-mode CO laser operating at a fixed total pressure of 1.5 torr in the 9-8 P(16) transition. The vertical scale is $0.15 \times 10^{-3}$ W/cm and the curves were taken at four different fixed driving power levels to show the effect of increasing the standing wave saturating field. The horizontal scale is about $2 \times 10^{6}$ Hz/cm and is somewhat nonlinear because of the nonlinear response of the piezoelectric mirror tuner to the linear voltage ramp driving the X-Y recorder. Note, however, that the significant difference in the heights of the two power maxima at sufficiently large saturating fields is real and quite reproducible. It appears to be quite certain that this effect cannot be ascribed to either changes in cavity Q, due to slight tilts of the frequency translating mirror, or to competition of other lasing transitions. Such asymmetries in He-Ne lasers could be interpreted by the presence of isotopes. In the CO system, isotope transitions do not overlap and must therefore be ruled out as a possible cause for line distortion. We hope that a variety of experiments currently under way will yield sufficient information to fit the experimentally observed curves to theory.

C. Freed

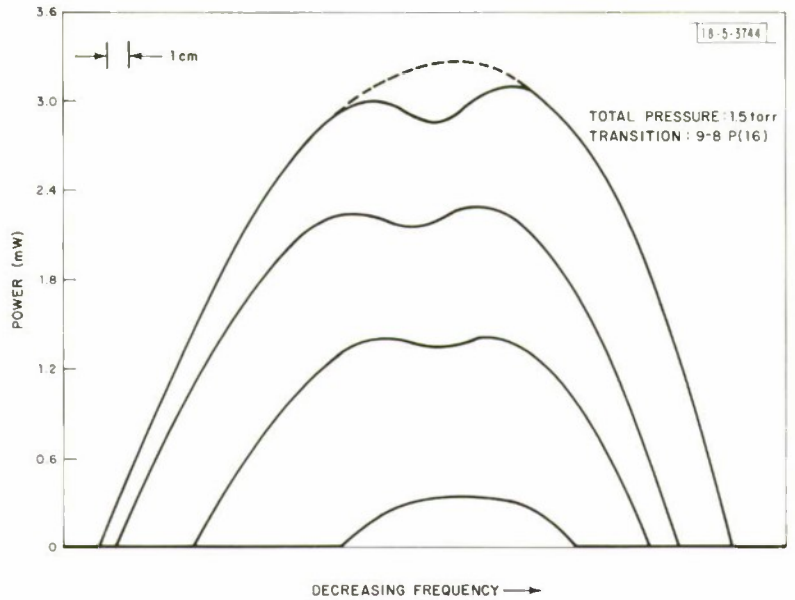


Fig. I-28. Multiple chart recording showing evolution of o typical Lamb dip in the CO loser power output.

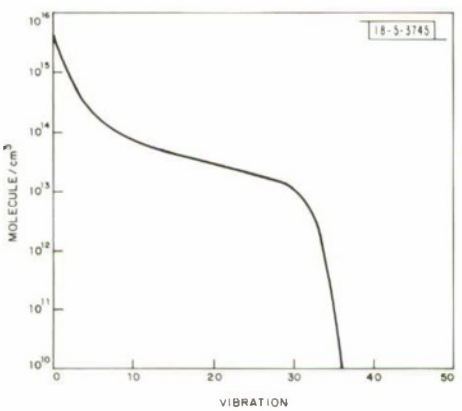


Fig. I-29. Vibrotional stote populations in CO-He dischorge.

## I. CARBON MONOXIDE LASER PLASMA RATE EQUATIONS

The carbon monoxide laser is of considerable technical interest because of its large spectral range and high electrical efficiency. The large spectral range can be explained only by a highly nonthermal distribution of the molecules over the vibration-rotation states. It is clear that this distribution is brought about by an anharmonic pumping effect in which molecules in low-lying vibrational states collide with others in high vibrational states, transferring a quantum of vibration, the molecules in the lower state then being re-excited by direct electron collisions. Such a process accounts for both the large number of vibrational bands on which lasing is observed and the high electrical efficiency of the device. We have undertaken a program of numerical modeling of these processes, and have achieved considerable success in predicting gains, saturation intensity and effect of the radiation field on the electron gas.

No direct attempt has yet been made to directly model the details of the electron energy distribution (although that is contemplated for the future); at present, it is assumed to be Maxwellian. The effect of molecule-electron collisions is modeled by the experimental cross sections of Schultz.[20] Vibration-translation (V-T) and vibration-vibration (V-V) energy exchange is modeled by an approximation to theory,[21] with assumed selection rules of $\Delta V = \pm 1$. The model also includes spontaneous and induced emission according to well known formulas.

A typical solution for the population densities is shown in Fig. I-29, and gains of the strongest lines are shown in Fig. I-30. The saturation intensity for this case was found to be roughly constant with V and J, and was about 1 $W/cm^2$.

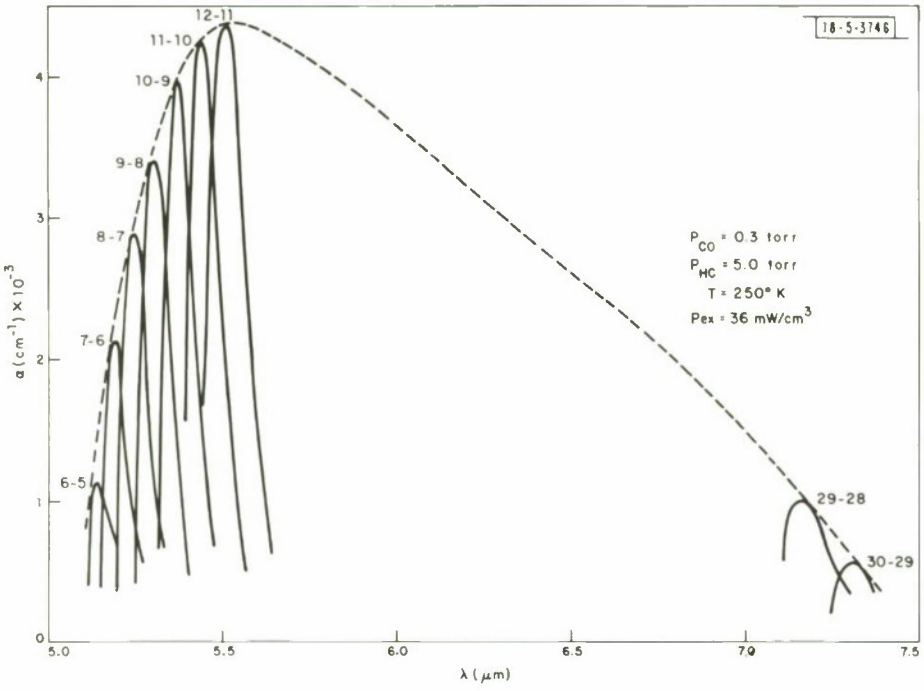


Fig. I-30. Small signal gains for populations in Fig. I-29.

Two features of these solutions are of interest: the rate of energy exchange via V-V exchange is high compared with the electronic pumping rates. For this reason we are justified in using the Maxwellian form for the electron energy distribution, since the vibrational state distribution is very insensitive to the exact form chosen for the electron distribution (rectangular distributions were tried, with no significant changes in shape). What is significant about the electron distribution is the net rate of energy deposition in the molecular vibration; it is this that we use to correlate our results with work on detailed electron distributions.[22] Second, over most of the significant range of vibrational quantum number at the densities of interest, the V-V exchange processes completely dominate the linear loss processes (V-T exchange, spontaneous emission), so that the shape of the population density curve is dependent mainly on the V dependence of the coefficients and is not strongly affected by their magnitude (it changes the location of the sudden drop of populations at high V – beyond this point, V-V no longer dominates). The saturation intensity, on the other hand, is strongly dependent on the magnitude of the coefficients and, in fact, will probably provide a sensitive measure of the overall coefficient of V-V exchange.

Future plans include simultaneous solution for both the electron energy distribution function and the molecular state distribution function, addition of a second species (nitrogen, which is found experimentally to enhance the performance), and modeling of molecular diffusion and heat conduction. We also hope to be able to include a more sophisticated model of the V-V coefficients based on a long-range electrostatic interaction,[23] although the model will probably prove to be relatively insensitive to the details of this.

A. H. M. Ross

## REFERENCES


1. M. Born and E. Wolf, Principles of Optics (Pergamon Press, New York, 1959), Sec. 9.1.2.
2. J. Herrmann and L.C. Bradley, "Numerical Calculation of Light Propagation," LTP-10, Lincoln Laboratory, M.I.T. (13 July 1971).
3. P.R. Longaker and M.M. Litvak, J. Appl. Phys. 40, 4033 (1969), DDC AD-699270.
4. D.H. Edwards, J. Sci. Instr. 35, 346 (1958).
5. Optics Research Report, Lincoln Laboratory, M.I.T. (1971:1), DDC AD-888823-L.
6. Air Force Weapons Laboratory, Laser Division Digest, LRD-71-1 (June 1971).
7. J.D. Swift and J.J.R. Schwar, "Electrical Probes for Plasma Diagnostics," American Elsevier (1969).
8. Yu P. Raizer, Soviet Physics Uspekhi 8, 650 (1966).
9. P.E. Nielsen and G.H. Canavan, Air Force Weapons Laboratory, Laser Division Digest (October 1971).
10. I.I. Glass, "Aerodynamics of Blasts," UTI Review No. 17, Institute of Aerophysics, University of Toronto (1960).
11. Optics Research Report, Lincoln Laboratory, M.I.T. (1970:3), DDC AD-882617.
12. J.W. Beams in "Physical Measurements in Gas Dynamics and Combustion," R.W. Ladenburg, et al., Eds. (Princeton University Press, 1954).
13. G.F. Kinney, "Explosive Shocks in Air" (The Macmillan Company, New York, 1962), p. 95.
14. C.A. Fenstermacher, M.J. Nutter, J.P. Rink and K. Boyer, Bull. Am. Phys. Soc. 16, Series II, No. 1, 42 (1971).
15. J.D. Daugherty, E.R. Pugh and D.H. Douglas-Hamilton, "A Stable, Scalable, High Pressure Gas Discharge as Applied to the $CO_2$ Laser," 24th Annual Gaseous Electronics Conference, Third Arc Symposium, 5-8 October 1971, p. 83.
16. E.W. McDaniel, Collisional Phenomena in Ionized Gases (Wiley, New York, 1964), pp. 224-227.
17. S. Marcus and R.J. Carbone, "Gain and Relaxation Studies in Transversely Excited HF Lasers," LTP-15, Lincoln Laboratory, M.I.T. (28 December 1971).
18. S. Marcus and R.J. Carbone, "Performance of a Transversely Excited Pulsed HF Laser," LTP-11, Lincoln Laboratory, M.I.T. (23 June 1971).
19. R.W. O'Neil, R.J. Carbone, H. Granek and H. Kleiman, "TEA Laser Medium Diagnostics" (to be published).
20. G.J. Schulz, Phys. Rev. 135, A988 (1964).
21. R.N. Schwartz, Z.I. Slawsky and K.F. Herzfeld, J. Chem. Phys. 20, 1591 (1952).
22. W.L. Nighan, Phys. Rev. A 2, 1989 (1970).
23. R.D. Sharma and C.A. Brau, Phys. Rev. Letters 19, 1273 (1967).

# II. OPTICAL MEASUREMENTS AND INSTRUMENTATION

## A. AIRBORNE OPTICAL IMAGING OF A WING-TIP POINT SOURCE

As previously reported,[1-4] the airborne performance of high-spatial-resolution instruments aboard the KC-135 airplane generally is inferior to the performance obtained when the airplane is parked on the ground. This phenomenon is of critical importance for the LFLC telescope, the primary high-resolution instrument aboard the airplane. Previous experiments have demonstrated that the telescope itself is unchanged in the airborne environment, and that the LFLC window mounted in the side of the fuselage maintains its optical figure in flight.[5] The logical next step is to investigate the image degradation due to the boundary layer and/or flow effects in the immediate vicinity of the airplane. The problem of isolating these effects from the degradation produced by a long atmospheric path was solved by placing an optical point source on the airplane wing tip. The results of an imaging experiment using the wing-tip point source are described here.

### 1. Equipment

After considering various alternatives, a passive (retroreflective mirror) method was selected for the wing-tip point source. The mirror was a small convex section (44-mm diameter) of a sphere (50-cm radius-of-curvature), mounted in a streamlined housing (see Fig. II-1) on top of the wing tip near the leading edge. The angle of the mirror was adjustable, so that it could be pointed at any of the instrument windows. For this experiment, the optical path extended from the wing tip to the LFLC window, which is located just forward of the cargo hatch, as shown in Fig. II-2. An optical diagram of the experiment is shown in Fig. II-3. A 5-mW HeNe laser, mounted alongside the telescope, illuminated the convex mirror. The curvature of the wing-tip mirror caused the reflected light to diverge, as if it radiated from the virtual focus approximately 25 cm behind the mirror. The reflected beam was automatically directed back toward the laser and the telescope mounted alongside. To accommodate small pointing errors, the laser beam overfilled the mirror aperture. The size of the reflected beam at the LFLC window was approximately 4 m in diameter. A 178-mm aperture, 6.2-m-focal-length Questar telescope was tripod-mounted behind the LFLC window for use in this experiment. (The Questar was used because the LFLC mount azimuth range does not include the wing tip.)

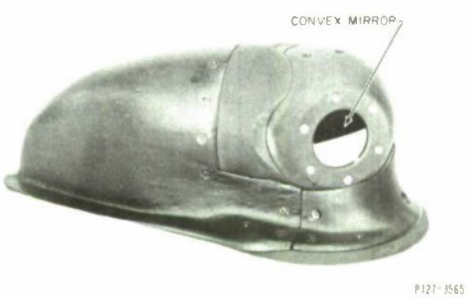


Fig. II-1. Retroreflective mirror in streamlined housing ready for installation on wing tip.

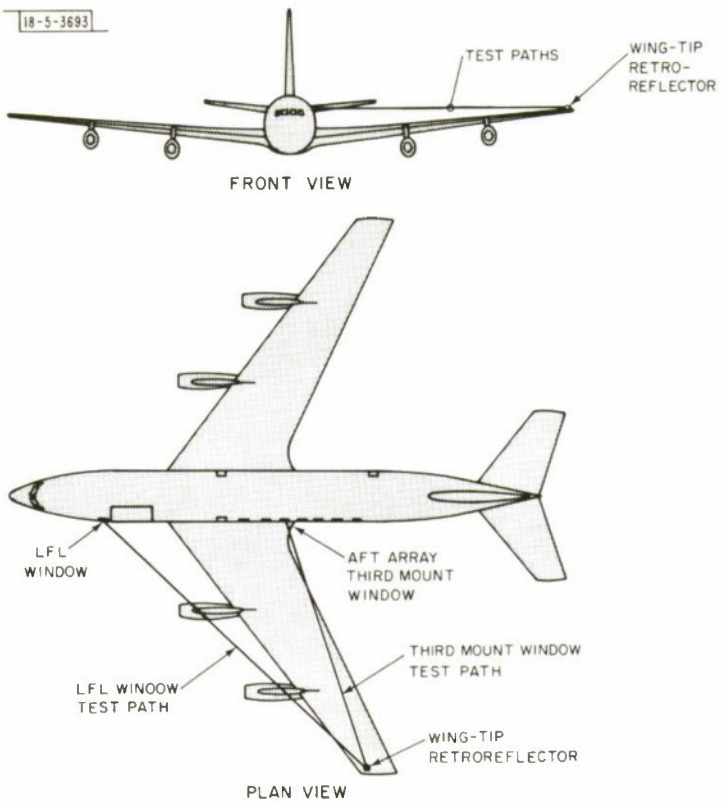


Fig. II-2. Locotion of opticol test paths. (Third mount window path wos used in interferometric imoging measurements described in Sec. II-C.)

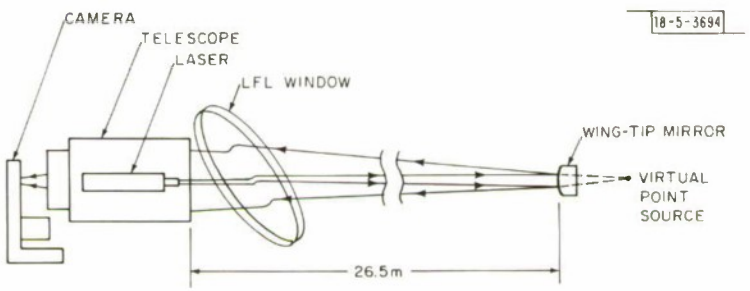


Fig. II-3. Opticol diogrom of wing-tip point-source experiment.

The aberration resulting from the use of a spherical mirror on the wing tip was negligible over the small portion of the returning wavefront whieh entered the teleseope aperture. Also, it has been shown that atmospheric turbulenee effeets on the outgoing beam are redueed by the ratio of the mirror foeal length to the wing-tip distanee (approximately 1/100) due to the foeusing aetion of the mirror. This has been verified by laboratory experiments. Consequently, degradation of the teleseope image was the result of only one traverse (incoming) of the optieal test path.

Images were reeorded with a Hyeam eamera capable of exposing 16-mm film at $10^4$ frames per seeond (f/s). The shutter installed in the eamera had a 40-percent "open" time. Three types of images were recorded: direct in-foeus images, images approximately 40-mm out of focus and images of the teleseope aperture illumination.

Foeused images were in every case selected from a eontinuous focus run to eliminate foeus shift uneertainty. Out-of-focus images were taken beeause eharacteristies of the image degradation source sometimes can be inferred from such data. Photographs of the telescope aperture were made to verify that the aperture was uniformly illuminated. All three types of images were obtained with the airplane on the ground and in flight at 9.5-km altitude.

## 2. Data

It is to be expeeted that the teleseope aperture illumination was uniform beeause of the relatively short atmospherie path. This was verified in both ground and airborne photographs made at $10^3$ f/s. In both eases, the photographs showed uniform illumination over the entire aperture. The resolution in these pictures was at least 5 mm in the aperture.

The out-of-focus photographs showed a definite change between ground and airborne conditions, as shown in Figs. II-4(a-d). In these pietures, the film intereepted the light so far in front of foeus that the shape of the eenter-bloeked telescope aperture is elearly visible. Figure II-4(a) shows a typieal frame from a sequenee exposed at $10^3$ f/s on the ground, and Figs. II-4(b) through II-4(d) show successive frames from an airborne sequence exposed at $2 \times 10^3$ f/s. In the airborne photographs, strong "bright spots" are evident, indicating the presence of wavefront phase irregularities which foeused light from eertain regions of the aperture at the film plane, which was 40 mm ahead of the best average foeus.

The loeation and size of these phase irregularities ean be estimated from the pictures. A reasonable size estimate for many of these irregularities is 1- to 2-cm diameter. Furthermore, knowing the focus shift produeed by the phase irregularities, one ean estimate that the wavefront phase distortion aeross a 2-cm-diameter "blob" was of the order $\lambda/2$. These appeared to be uneorrelated in sueeessive pictures, with rare exceptions. Approximately once or twiee during an 8-seeond data-taking run, a reeognizable feature persisted for several frames as it moved across the out-of-focus image. This has oeeurred at both airplane speeds, Mach 0.8 and 0.6, and in most instances, the velocity of the feature was found to be approximately 120 m/sec (assuming it passed directly in front of the telescope aperture). The free-stream velocity for these Maeh numbers is 240 and 180 m/see, respectively.

Early in these experiments, additional slow-moving, relatively weak irregularities were observed in the out-of-foeus images. These soon were assoeiated with the aeeumulation of cold air masses at the inner surface of the window. They were eliminated by the use of an "air curtain" streaming down across the window surface in later flights with no substantial image improvement.

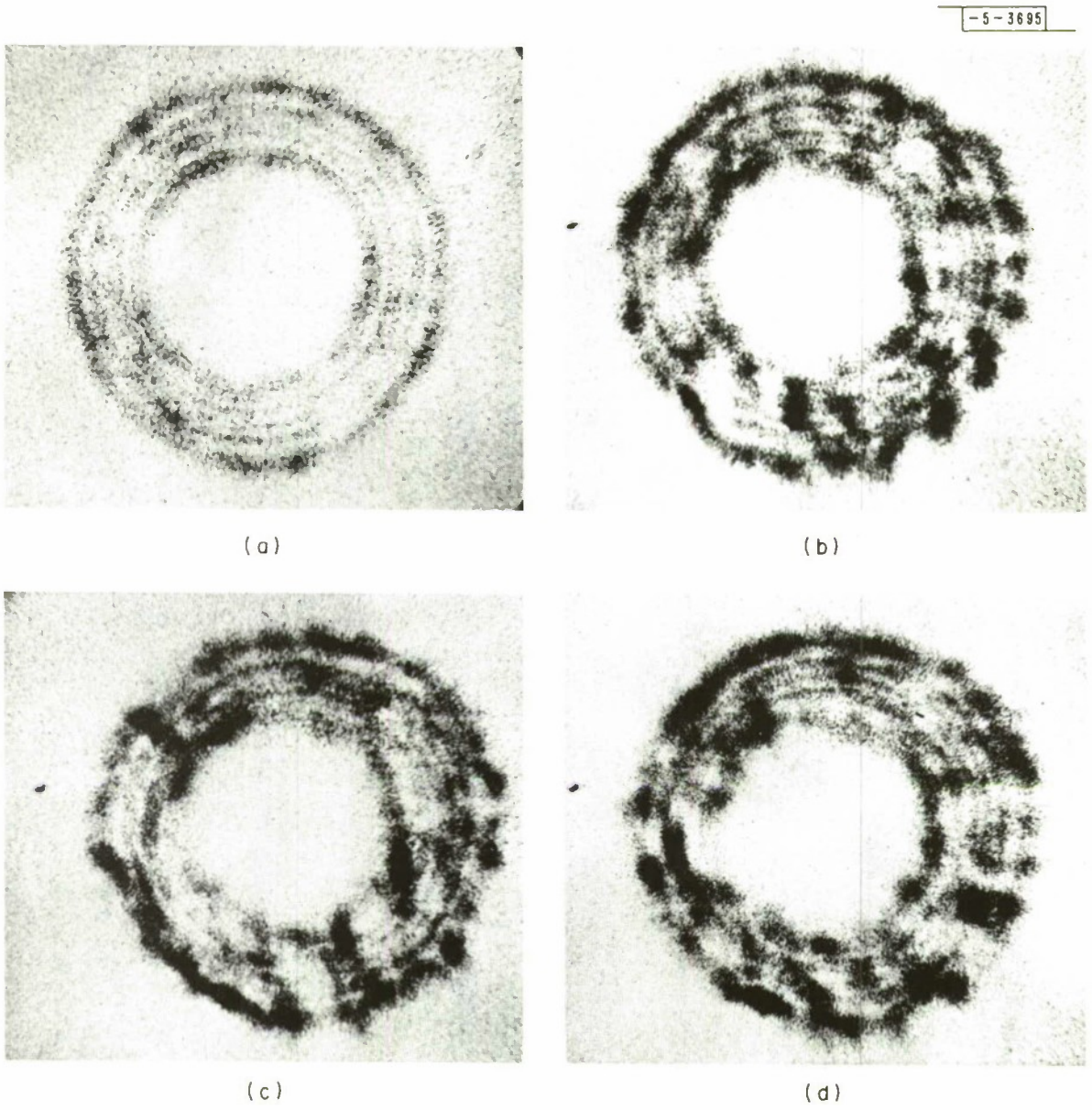


Fig. II-4. Wing-tip point-source imoges, 40-mm out-of-focus; (o) ground, (b-d) oirborne.

Photographs of the focused wing-tip souree image were obtained at various frame rates up to $9 \times 10^3$ f/s. The ground images were taken at $2 \times 10^3$ f/s. They showed considerable similarity from frame to frame, with a traee of the outer diffraction rings sometimes visible. The airborne images were all larger and showed irregularities of a random nature. After viewing the films on a stop-motion projeetor, it has been eoneluded that only at the highest framing rate ($9 \times 10^3$ f/s) ean any signifieant correlation be seen between suceessive frames, espeeially at the Maeh 0.8 flight speed. Even then, only about half the frames show features appearing in preeeding frames. For the Maeh 0.6 flight speed, there appeared to be slightly more correlation, beginning at a lower frame rate ($7 \times 10^3$ f/s).

The image sizes were estimated visually from the photographs by a grain-counting technique whieh established the diameter eontaining 90 percent of the image energy. Measured in this way, the ground images of the wing-tip point souree averaged 33-μrad diameter. This number was somewhat larger than expeeted for two reasons. The first was that the images were slightly overexposed. The seeond was that an unexpeeted aberration oeeurred beeause the expanding wavefront from the wing-tip souree passed through the LFLC window obliquely. This was despite the faet that the LFLC window was exceptionally homogeneous and plane-parallel. The aberration would have been smaller if the window had been normal to the optieal path, and would have disappeared if the souree had been at infinity. (The test path made an angle of 52° with respeet to a perpendieular to the window.*) Despite this, comparisons with the airborne images can be made because the exposure and the window aberration remain unehanged.

TABLE II-1
IMAGE SIZE
(μrad)

| Air Curtain | | Off | On |
|---|---|---|---|
| Speed | M = 0.8 | 45.1 | 53.7 |
| | M = 0.6 | 43.3 | 43.4 |

Table II-1 shows the image sizes obtained at the two flight speeds, each with and without the air curtain blowing aeross the inside of the window. Table II-1 also shows that the image size was not correlated elearly with either flight speed or the air eurtain. Ilowever, all the airborne images were signifieantly larger than the ground images. If one postulates an airborne image degradation source that added to the ground image in an rms manner, it must have a magnitude of approximately 30 μrad.

### 3. Conclusions

The nature of the experimental results points to a strong optieal disturbanee just outside the LFLC window, sueh as the turbulent boundary layer next to the fuselage. The remainder

* Since this experiment was performed, it has been found that a large part of the aberration can be removed by placing a tilted compensating plate just in front of the focal plane.

of the test path traversed airflow regions which are believed to be laminar. The boundary layers in front of the mirror and over the wing tip are expected to be quite thin. In addition, this experiment was not sensitive to turbulence near the mirror.

It was found that the wingtip source image details persisted for only $10^{-4}$ sec. The speed of the persistent "blobs" noted in the out-of-focus images was typical of velocities in the boundary layer. The temperature difference required to produce a $\lambda/2$ optical path defect in 2 cm at 10-km altitude is 35°C, a value similar to the temperature differential across the boundary layer on this airplane.

If one assumes that the image degradation is a boundary-layer effect, and furthermore, that the degradation is proportional to the path length through the layer, then the degradation expected for a path normal to the LFLC window is 19 μrad.

Many people assisted either in the construction of equipment or in the collection and discussion of these data. Among them were Mr. Donald E. Boucher, Mr. Morgan A. Thomas, Mr. Lewis W. Chaulk, Dr. Barry W. Bryant and Dr. Dennis Kelshall.

D. G. Koeher

## B. AIRBORNE IMAGE STUDIES

New measurements made in Hawaii and Christchurch, New Zealand, have supported, with some modifications, the formula for the airborne 90-percent image size proposed in the last Optics Research Report.[1] A new set of diffraction-limited optics (see Ref. 1, pp. 34-35) was installed in the KC-135 aircraft in June 1971 in order to eliminate one of the remaining intrinsic degradations. Also, a counterbalance mechanism was installed on the telescope mount to keep it in fine balance as the instrument was focused. Mount balance of both the telescope and tracker was found to have a significant effect on the resulting image size. Stellar photographs taken from the ground at Hickam Air Force Base with the new optics and the mounts carefully balanced, and the Barnes tracker alternately switched on, then off, have shown that the tracker component is now within the statistical fluctuation of the measurements, about 1.0 μrad. The rms combination of telescope spread function (~4 μrad), aircraft vibration (6 μrad), film spread function (~5 μrad) and tracker component (~0) is now about 9 μrad, instead of the previous value of 20 μrad. Part of this decrease, of course, can be attributed to improved telescope performance, but most of it has resulted from improved tracker performance. In view of this substantial improvement in the intrinsic background "noise level," it was rather surprising to find on examining the Christchurch data that the images were only slightly improved over previous measurements. The average image size approached ~20 μrad asymptotically as the zenith angle (z) was decreased. This implied that there remained a Z-independent component which was extrinsic to the telescope and which was on the average of the order of 18 μrad. This agrees quite well with the results of the wingtip retroreflector experiments, described earlier in this report, which would strongly suggest that boundary-layer turbulence was the major source of this extrinsic degradation.

The data recently obtained at Christchurch have also afforded an opportunity to check the magnitude of the $\Delta\mu$ and the manner in which atmospheric dispersion enters the equation. A number of blue and blue-white stars were photographed at elevation angles below 15° (Z = 75°). The effective continuum spectrum of these stars is assumed to extend from 3000 to 6000 Å; the lower limit is imposed by the optics, the upper by the film. From Edlén's atmospheric dispersion formula,[6] it is found that at NTP, $\mu(3000\,\text{Å}) - \mu(6000\,\text{Å}) \cong 1.458 \times 10^{-5}$, or $\Delta\mu_o \cong 15 \times 10^{-6}$.

It will be further assumed that $\mu \cong \mu_o e^{-h/h_o}$; where h is the altitude above the earth's surface and $h_o$ is the index scale height, which is about 8 km. The mean altitude of the aircraft is 10 km, so that we would expect $\Delta\mu$ to be about $4.3 \times 10^{-6}$. This number is much below the number quoted earlier[1] of $9 \times 10^{-6}$, which was determined from insufficient low elevation angle data. The expression for angular dispersion is easily derived from Snell's law, $\sin Z/\sin\Theta = \mu_1/\mu_2$; where $\mu_1$ is the index of free space, $\mu_2$ is the local index, Z is the zenith angle and $\Theta$ is the refraction angle. The result is $D = \Delta\Theta \cong \Delta\mu \tan Z$, provided $\frac{1}{2}(\Theta_{\lambda_1} + \Theta_{\lambda_2}) \cong Z$. The expression is useful to within a few degrees of the horizon; however, it rapidly diverges from the observations as Z approaches 90°. The direction of the dispersion is in the star-observer meridian plane. If we take $\varphi_L = (\Sigma 0^2 + D^n)^{1/2}$ for the angular image size in this plane and $\varphi_W = (\Sigma 0^2)^{1/2}$ for the image size normal to this plane, then a plot of $\log(\varphi_L^2 - \varphi_W^2)$ vs $\log\tan Z$ should yield both n (from the slope) and $\Delta\mu$ (from the Z = 45° intercept). The $\Sigma 0^2$ term represents the mean square combination of all degradations other than dispersion. The results are shown in Fig. II-5. Despite the large standard deviation in the smaller Z angle measurements (to be expected), the slope is found to be between 1.7 and 2.3 and $\Delta\mu$, between 3.2 and $6.9 \times 10^{-6}$, which on the average yield $n \cong 2.0$, $\Delta\mu \cong 5.0 \times 10^{-6}$. These are very close to their expected values. It should be noted in

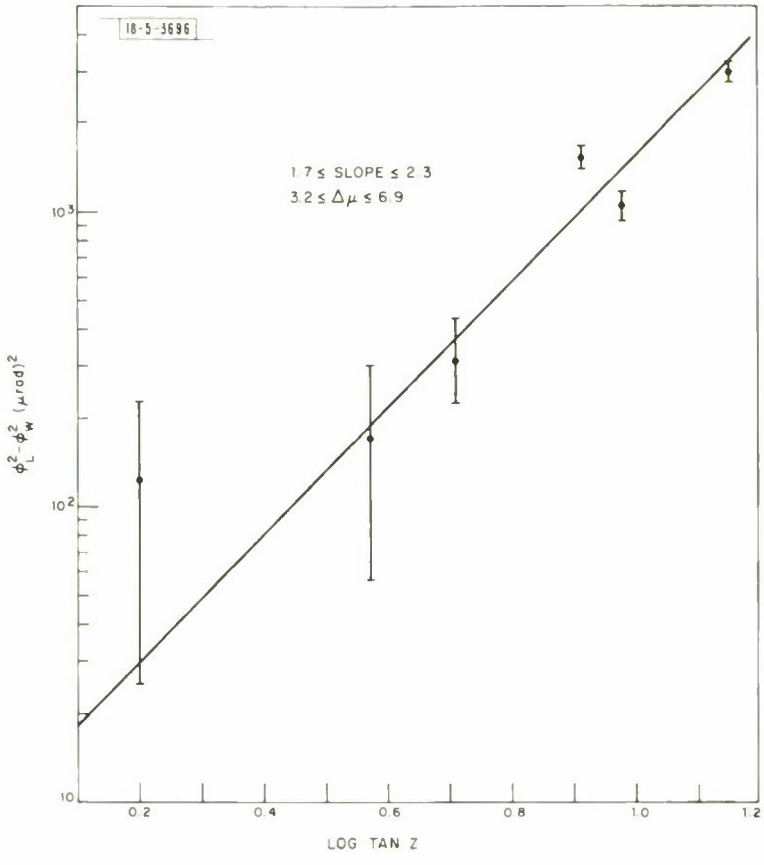


Fig. II-5. Log $(\phi_L^2 - \phi_W^2)$ os o function of log ton Z.

passing that the assumption of a linear superposition of D on the other degradations, i.e., $\varphi_L = (\Sigma 0^2)^{1/2} + D^m$, leads to an incorrect angular dispersion relation ($0.4 \leqslant m \leqslant 0.5$) and a much smaller $\Delta\mu$ than expected ($2.0 \leqslant \Delta\mu \leqslant 2.5$). We conclude that the angular dispersion behaves more or less as a random variable in the presence of the other airborne perturbations.

The zenith blur component,[7,8] S, can be estimated from narrowband data in which atmospheric dispersion has been substantially reduced. Even assuming dispersion to be zero, one cannot make the measurement directly at altitude because it is very much smaller than the "boundary-layer" component. However, if one extracts the difference in the squares of narrowband image size measurements made at high and low elevation angles, then neglecting dispersion, one obtains $\varphi_1^2 - \varphi_2^2 = S^2(\sec Z_1 - \sec Z_2)$, where $Z_1$ and $Z_2$ are the zenith angles corresponding to angular image sizes $\varphi_1$ and $\varphi_2$. Using this technique, we have found $2 \leqslant S \leqslant 4.5 \times 10^{-6}$.

The formula representing the angular diameter (in μrad) in which approximately 90 percent of the exposed grains are located can now be written as follows:

$$\varphi = [a^2 + (\Delta\mu \tan Z)^n + S^2 \sec Z + B^2]^{1/2} \quad ,$$

where

$$a \approx 9$$
$$3 \leqslant \Delta\mu \leqslant 7$$
$$1.7 \leqslant n \leqslant 2.3$$
$$2 \leqslant S \leqslant 4.5$$
$$B \approx 18$$

There is now a fair amount of confidence, based on the retroreflector experiments, that B represents the degradation caused by boundary-layer turbulence. The dispersion term is also felt to be fairly well established. However, it must be remembered that the above formula does not predict exactly what will be observed on a given night, but only what is most likely to be observed averaged over several successive clear nights. This is because many complicated weather phenomena do occur at these altitudes from time to time, which adversely affect imaging, but which by necessity had to be left out of detailed consideration. Furthermore, it should be kept in mind that the dispersion term $\Delta\mu$ depends heavily on the spectral intensity distribution of the source and the bandpass of the system.

B. W. Bryant

## C. INTERFEROMETRIC IMAGING TECHNIQUES

The laboratory corner cube shearing interferometer (described in Ref. 9) has been used to make a series of modulation transfer function (MTF) measurements of the atmosphere from the KC-135 airborne optical aircraft. Two main series of tests have been conducted aboard the aircraft in flight and a number of ground measurements have been made.

### 1. Retroreflector Measurements in Flight

An 89-mm-diameter optical telescope coupled to the interferometer was mounted on a tripod and pointed through the front optical (LFLC) window or the third mount window of the aircraft toward the wing tip. On the wing tip was mounted a convex mirror of 50-cm radius (see Sect. II-A). A HeNe CW laser, with a diverger lens (focal length – 44 mm) placed in the laser beam, was

mounted on the same base plate as the interferometer. The laser was arranged to illuminate and overfill the convex mirror on the wing tip such that the reflected beam could be received by the 89-mm telescope and interferometer instrument. In practice, this arrangement was equivalent to having a point source located at the wing tip. Only the central-most uniform portion of the laser beam was collected by the 89-mm optics.

Visual viewing of the resultant sheared interferogram formed by the interferometer could readily be made. The interferogram could be photographed with a 35-mm camera, while the electrical signal (from the photomultiplier) giving the MTF data was displayed on an oscilloscope in real time (this enabled focusing of the telescope for maximum signal), as well as being recorded on an FM magnetic-tape recorder. This experiment was aimed at obtaining MTF measurements of the near-air-path (or boundary-layer) atmospheric degradation for the aircraft in flight.

### 2. Star Source Measurements in Flight

Measurements over long paths through the atmosphere were made with the interferometer looking at star sources. The interferometer was mounted on the third gimballed mount of the aft array located above the wing of the aircraft (the instrument being dynamically balanced on this mount). It was arranged such that either of two optical telescopes (one 89 mm, the other 178 mm in diameter) could be used in conjunction with the interferometer. Stars could be tracked in flight (by means of the "on-board" Barnes tracker) to keep the star source in the center of the field of view of the telescope. In this way, the MTF along long atmospheric paths could be measured for various elevation angles while in flight. For these measurements, a beam-splitter arrangement allowed 10 percent of the incoming light to be filtered off before entering the interferometer to provide an intensity reference record. This aided in the subsequent data analysis, in that intensity fluctuations or scintillations could be checked (and compensated for, when necessary) at any time. MTF measurements were also made above and below the tropopause, in an extension of the flight measurements carried out in the vicinity of Christchurch, New Zealand, using different star sources. In each case, the measured MTF included both the long-path and the near boundary-layer path image degrading effects from the aircraft.

### 3. Ground Measurements

On the ground, MTF measurements were made from the aircraft through both the front and third mount windows, and also independent of the aircraft. Using the 89-mm optics, the retroreflector experiment was done through both windows.

A boresight light located approximately 13.3 km from the aircraft on a hillside, along a nearly horizontal path, was also available (a white-light source). MTF measurements from the aircraft through the third mount window (with the tracker operating) were made with both the 89-mm and 178-mm optics using this 13.3-km light source.

The interferometer, together with the 89-mm optics mounted on a tripod, was pointed at a star and MTF measurements were made from a nearly sea level location (Bedford, Massachusetts) and on Haleakala mountain at 3-km altitude. In these cases, the star motion in the sky was sufficient for the light collected by the telescope to "track" across the field of view, and measurements were obtained (without a tracker system) with the interferometer.

Using the 178-mm optics, a star was tracked through the third mount window of the aircraft on the ground, and an MTF curve was recorded.

### 4. Results – Retroreflector Measurements

The MTF curves for the retroreflector experiment are shown in Fig. II-6. Measurements in flight were made from the front window both at night and during the middle of the day and from the third mount window in the daytime only. The mean MTF curve for several runs on each flight is shown. In all cases except one, the curves obtained were similar. The exception (curve 3) was one taken in daylight, passing through a cold front, in which case a significantly lower MTF curve was obtained.

Measured MTF curves made at a normal (460-knot) air speed and then at a slower (385-knot) air speed did not vary significantly from each other. MTF curves measured through both windows with the aircraft on the ground (dashed lines) are shown in Fig. II-6 compared with the optical diffraction-limited curve. The effective point source at the wingtip results in a spherical wavefront propagated through the aircraft window, which makes a large angle with the normal to the window producing a small amount of astigmatism. This angle is larger for the front LFLC window, and in this case, more astigmatism is produced. Thus, the measured MTF for this window is poorer than in the case of the third mount window, as shown in Fig. II-6. The astigmatism will not occur when the point source (e.g., a star) is located a large distance away from

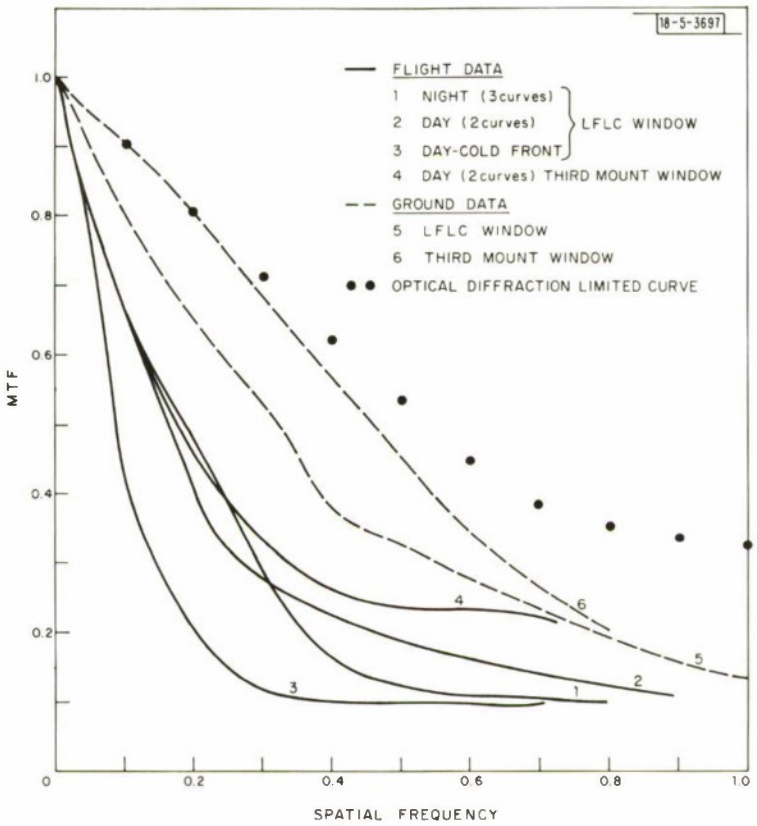


Fig. II-6. Retroreflector MTF measurements (89 mm optics).

the window, sueh that a plane wave is ineident on the window. The distance from the wing-tip mirror to the teleseope inside the aircraft window was about 27 m for the LFLC window and 19 m for the third mount window.

These measurements indicate a degradation arising from the flight environment. The curves on at least seven sets of measurements are more or less the same, with one exception. The exception appears to be one case when a much poorer MTF (curve 3 in Fig. II-6) resulted. In this ease, the aircraft was flying through a cold front. The difference in length of the light path from the wing-tip mirror to either the front window or the third mount window does not appear to influence the MTF significantly, nor does the window location (distance from the nose of the aircraft).

Visual observations were made of the sheared interferogram with the telescope defocused, and in some cases photographs were taken. On two of the night flights, fringes observed visually could be seen out to a shear of $s = 1.0$ and $s = 1.5$, respectively (i.e., two to three times higher shear values than those for which the MTF data were obtained). On daylight flights, the fringes could be seen only to shears of $s = 0.6$ at the best. It therefore appears that these MTF curves have long, but very low, contrast skirts on them, such that low contrast extends to higher-resolution (high spatial frequencies) values than indicated in the figure. However, the energy in the skirts is probably very small and may hardly affect the actual images. The electrical signals were too noisy to reeord these low-contrast signals at high shear values. This high-resolution fringe contrast varies from flight to flight, being less evident during daytime flights.

### 5. Results – Star Source Measurements

From a number of star measurements made with the 89-mm optics and interferometer above and below the tropopause at low and high elevation angles, four MTF curves have been plotted in Fig. II-7. These were the highest measured MTF curves obtained in the series. The best mean curve for this data is shown compared with the mean retroreflector MTF measurement made from the same third mount on the aircraft in flight. The optical diffraction-limited curve is shown for reference.

Analysis of all the data obtained (seven MTF curves using different stars) showed no significant difference between measurements made above or below the tropopause, nor at different elevation angles from 4° to 52°. Also, it appears that the mean long-path MTF curve (using star sources) looks very similar to the near-path (19-m source distance) retroreflector MTF curve.

A comparison of the flight data with the ground data using the 89-mm optics is shown in Fig. II-8. The star source MTF at sea level is substantially lower than that MTF measured from the top of Haleakala mountain at 3-km altitude. This 3-km altitude measurement (actually the mean of three MTF curves taken throughout the night) lies fairly close to the flight data measurements. On the other hand, the 13.3-km light (along a near horizontal path) gives a much higher MTF than either the flight MTF curves or any of the long vertical paths through the atmosphere.

Several measurements have also been conducted with the 178-mm telescope in place of the 89-mm optics. The MTF curves, each the mean of several measurements on different stars for each of three separate flights, are shown on Fig. II-9. Each of the New Zealand curves includes measurements above and below the tropopause, at various elevation angles between 10°

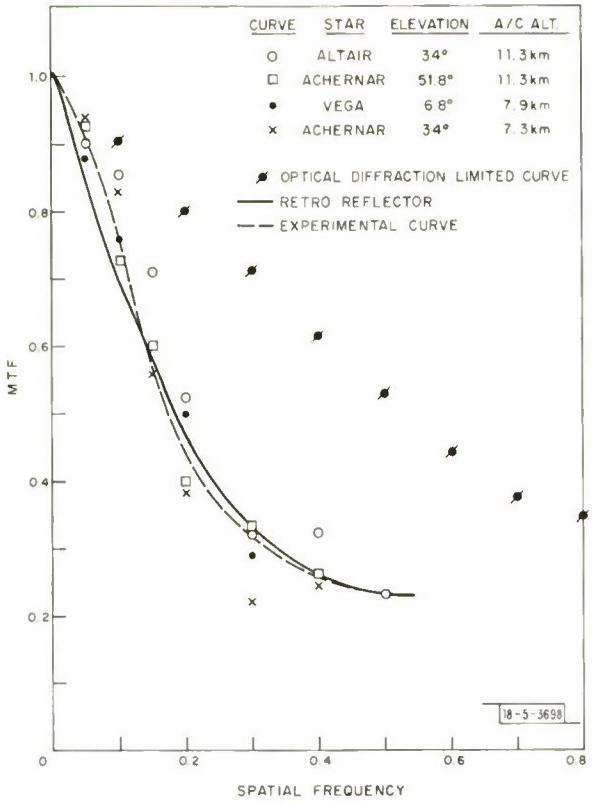


Fig. II-7. Star-source MTF measurements (89 mm aptics) fram airplane.

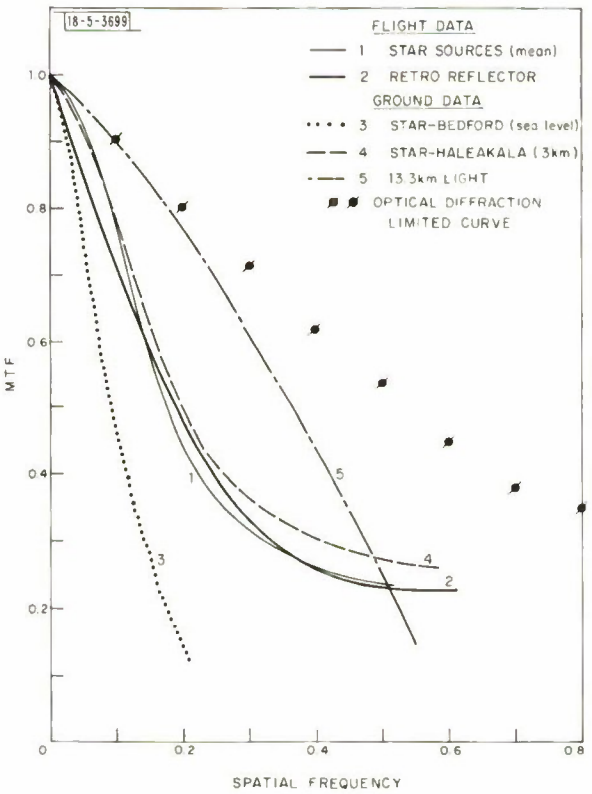


Fig. II-8. Comparison of ground and flight MTF data (89 mm aptics).

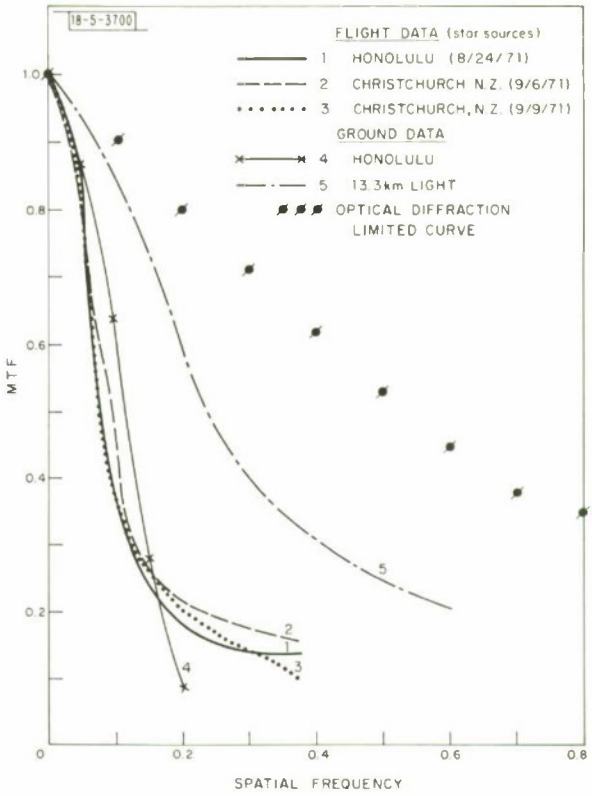


Fig. II-9. Comparison of ground and flight MTF data (178 mm optics).

and 51°. Again, no significant trend between the MTF below or above the tropopause, nor any angular dependence was observed. For comparison on the same figure, a ground measurement of both a star and the 13.3-km light is shown on the same figure. Again, for the 13.3-km light, the MTF is substantially higher than any of the long-path MTF curves. [Note: The reduced spatial frequency parameter $s = 2\lambda RF$, where $\lambda = 560$ nm, R = spatial frequency in cycles/cm and F = f/D (f is the focal length and D, the optics diameter). The angular frequency is then $\Delta\Theta = (2/s)(\lambda/D)$.]

### 6. Conclusion

The measurements described demonstrate that the corner cube interferometer can be made to operate aboard an aircraft in flight, with both laser and white-light (star) sources. A complete analysis of the data has not yet been carried out, but the measurements indicate the aircraft boundary layer is mainly responsible for the aircraft seeing problem.

D. Kelsall

## D. ZnS UPCONVERSION

We have examined the IR upconversion to visible light and absorption in ZnS phosphors as a function of wavelength from 2 to 16 μm (Ref. 10). To accomplish this, the apparatus depicted in Fig. II-10 was used. Since radiation from warm surfaces would interfere with our measurements, a cooled filter assembly was used as a monochromator. The nine filters, cooled to 77°K, were each 1-μm bandpass filters centered on wavelengths 2 μm apart from 2 to 16 μm. In this arrangement, the phosphor views only IR radiation from the blackbody source passed by each cold filter

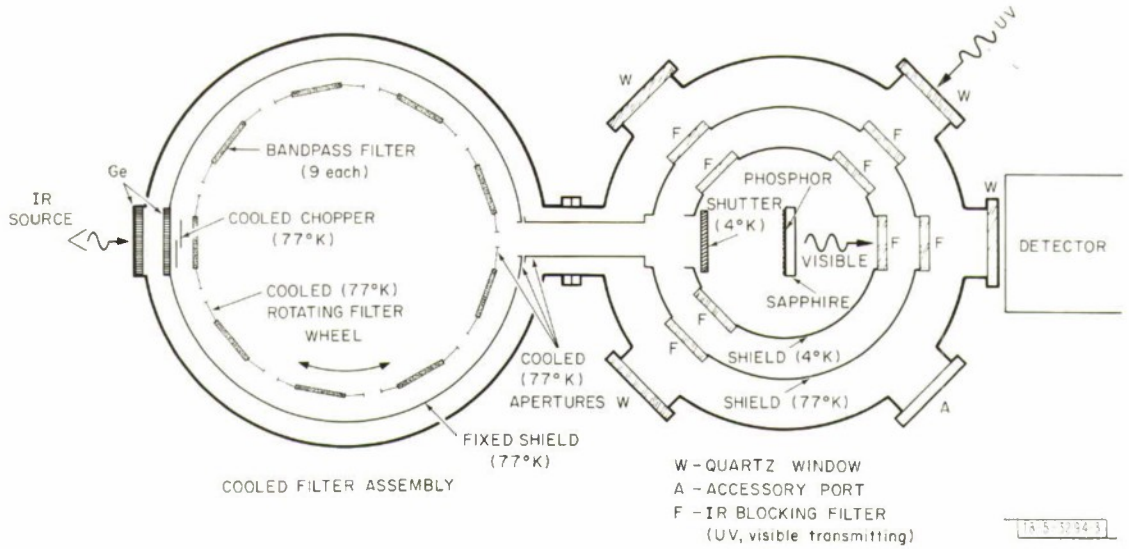


Fig. II-10. ZnS upconversion measurement apparatus.

successively rotated into the optical path. An additional small amount of radiation comes from the cold surfaces. The relative amount of IR radiation passed by each filter was measured and agrees to within 10 percent with that calculated, knowing the blackbody distribution and filter characteristics. Using this equipment, we have measured the visible output of our best ZnS phosphor powder as a function of wavelength and IR intensity. Figure II-11 shows, for example, scope traces of the visible signal for 2-μm radiation of different intensities. Below each photo is indicated the relative rate of IR photons incident upon the phosphor. One observes readily that at high intensities, the phosphor responds immediately and decays rapidly as the luminescing centers deplete. At lower intensities, the peak response is not observed until about 0.2 to 0.3 sec after the IR shutter is opened and the decay is much slower. Similar photographs are obtained at other wavelengths. In Fig. II-12 we show the peak visible output as a function of the IR photon intensity for different wavelengths. On this log-log plot we observe that for each wavelength except 14 μm, the straight lines are parallel with a slope of about 0.85, indicating that the response follows an $I = c_\lambda i^{0.85}$ dependence, where I is the peak response, $c_\lambda$ is a wavelength-dependent constant and i is the relative number of incident IR photons. We have no explanation for this behavior nor for the different slope of the 14-μm line. Figure II-13 shows the peak response as a function of wavelength for a constant value of i = 0.03 in Fig. II-12. Since Fig. II-13 is plotted for the same rate of incident photons at each wavelength, the vertical scale is also representative of the relative quantum efficiency. We see that the efficiency at 2 μm is about 3.5 times that at 10 μm. The rise in efficiency at 12 μm appears to be real and not some experimental anomaly. We have previously reported an absolute quantum efficiency of about $10^{-3}$ for the wavelength band 7.5 to 13 μm. The absolute value obtained from the above results is in agreement with this. These measurements were all taken with the powder sample at 4°K. At 77°K, there is no measurable stimulation effect at any wavelength within our experimental limits, except a barely perceptible response at 2 μm.

We turn now to absorption measurements and the effect of ultraviolet excitation on IR absorption as a function of wavelength. For these measurements, the apparatus of Fig. II-10 was used,

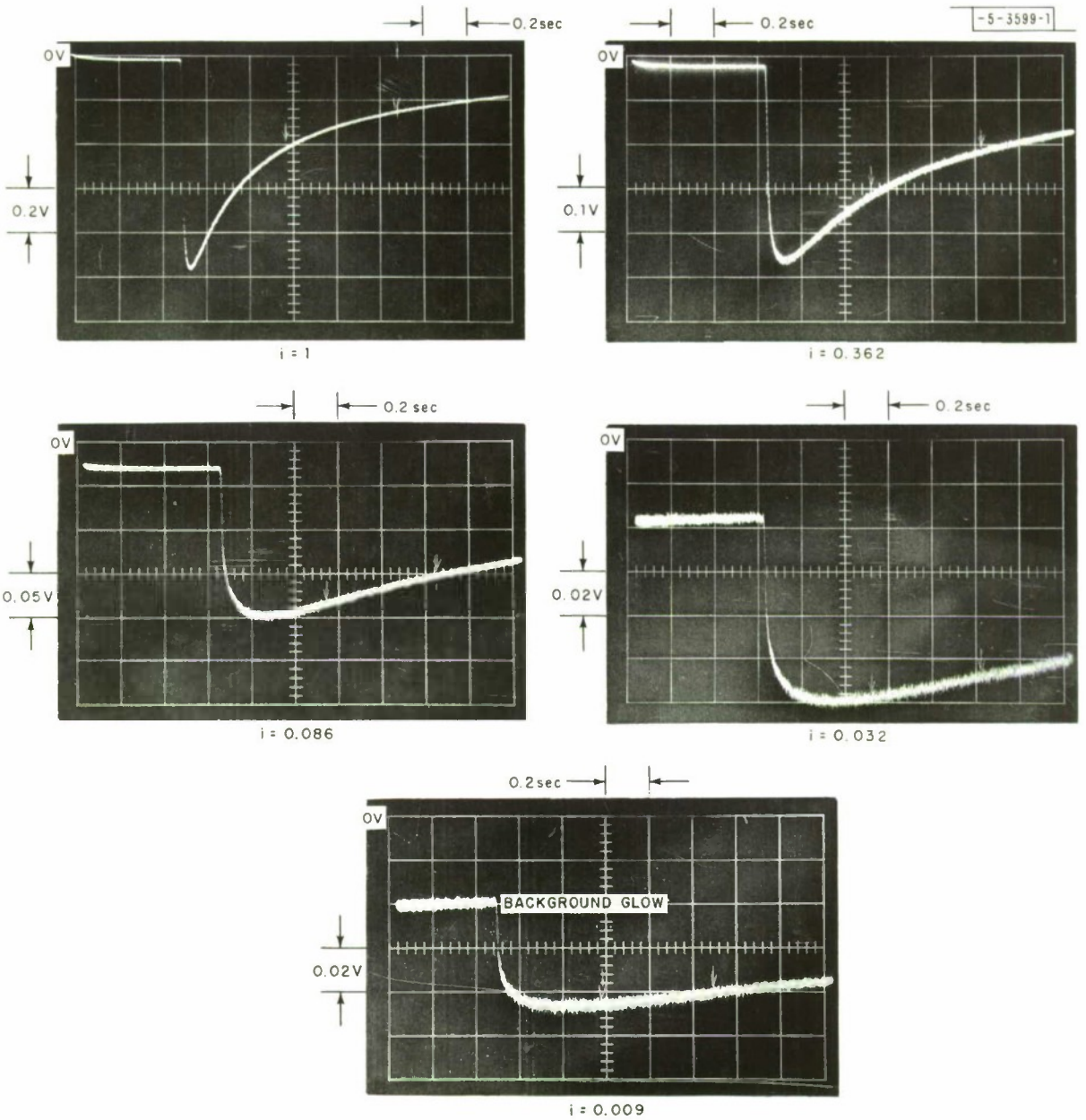


Fig. II-11. Oscilloscope traces of visible signal output for different IR intensities at $\lambda = 2\mu$. i refers to relative number of IR photons/sec incident upon phosphor sample.

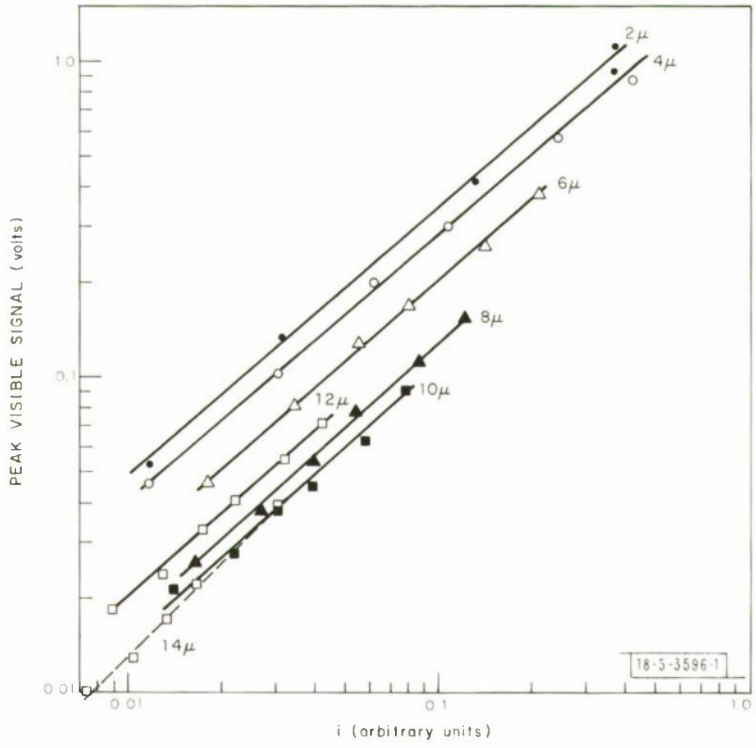


Fig. II-12. Plot of peak visible signal from phosphor as a function of i, the number of incident photons/sec at different λ.

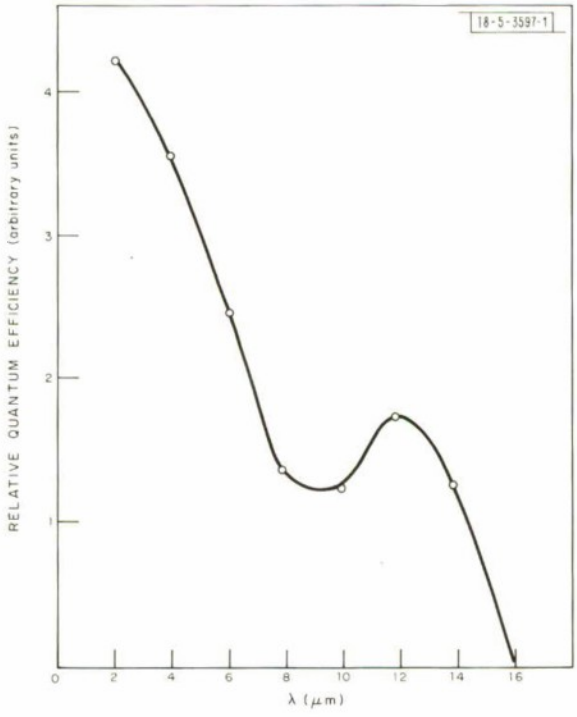


Fig. II-13. Relative quantum efficiency vs λ at i = 0.03 in Fig. II-12 (visible signal/number of incident photons/sec).

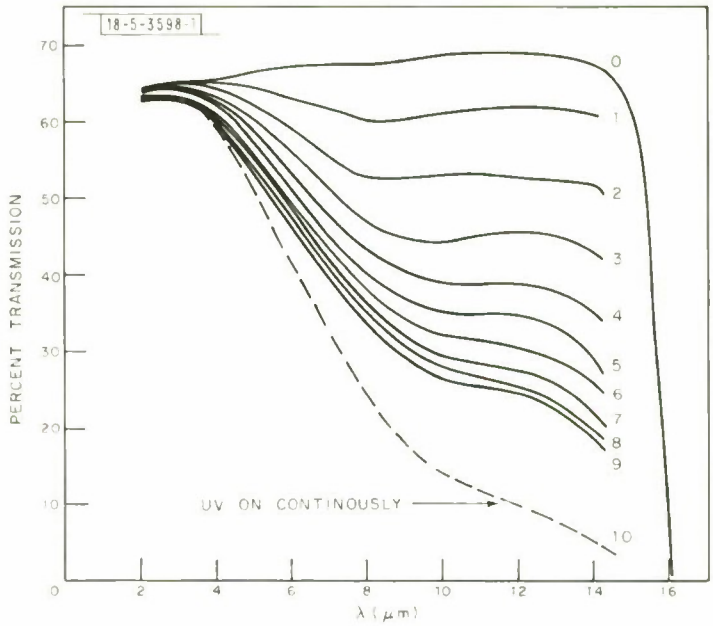


Fig. II-14. Tronsmissian af ZnS phosphor crystol vs λ and effect of successive 4358 Å illuminotian ot 4°K. Curve 0 was token with no UV illumination. Curves 1 through 9 were taken ofter successive illuminatians of 40 sec eoch with UV off during transmissian measurement. Curve 10 was meosured with UV on continuously ond somple soturoted.

with modification of the exit ports of the sample dewar to allow transmission of IR radiation for external measurement. To eliminate any effects due to scattering or voids in a powder, a single crystal sample with IR stimulability similar to that of our powders was used. In a series of measurements, the sample at 4°K was successively exposed to constant amounts of 4358 Å radiation and its IR transmission measured afterward with this radiation off. The effect of the 4358 Å radiation on the transmission is seen in Fig. II-14. We see that after each successive exposure, the transmission at longer wavelengths decreases. This absorption is not directly related to the IR stimulation effect, since it is long lived and the stimulation effect is exhausted after a few seconds of IR exposure.

It appears that only a few percent of the incident IR photons are absorbed in visible luminescing centers. To give some feeling for the duration of the absorption observed in Fig. II-14, ten minutes after the dashed curve was recorded and the UV shut off, the transmission at 10 μm had increased only from 14 to 21 percent. The effect of the 4358 Å radiation on the transmission at 77°K is not as great as at 4°K, but still very significant. At 77°K, under conditions which correspond to those of the dashed curve of Fig. II-14, the transmission at 10 μm was 36 percent.

A 4-inch IR imaging camera has been constructed and is undergoing final assembly and tests at this writing. Imaging tests will begin imminently to determine resolution limits of our phosphors and the image-producing quality of the total system. Other imminent work on our phosphors will involve measurement of the response to short fast pulses of IR radiation. It is clear

from Fig. II-11 that the time response will depend on intensity, and measurements will be made involving those parameters.

W. J. Scouler
D. H. Dickey
T. M. Quist

## E. TUNABLE SEMICONDUCTOR LASERS FOR AIR POLLUTION DETECTION

This work has been described in detail in a report to the Environmental Protection Agency, "Development and Application of Tunable Diode Lasers to the Detection and Quantitative Evaluation of Pollutant Gases." The summary of the report follows.

> "The purpose of this program is to develop and apply tunable semiconductor diode lasers to problems associated with the monitoring of pollutant gases. During the initial phase of the program, reported herein, lasers were developed to operate in the 8.7 μm region where sulfur dioxide ($SO_2$) has a strong infrared absorption band. Because of the potential usefulness of this band for various infrared techniques for the detection of $SO_2$, ultra-high-resolution laser scans were used to catalog several hundred of the spectral lines at reduced pressure. A theoretical spectrum for this band of $SO_2$, derived elsewhere on the basis of accurate microwave spectra, was found to be in near perfect agreement with the laser spectra once the band center used in the theory was properly adjusted on the basis of the laser data. We can now predict most strong $SO_2$ lines in this region, and construct with reasonable accuracy the absorption or emission spectrum of this gas corresponding to anticipated conditions of temperature, pressure, and instrumental resolution. Such information can be used, for example, to determine the optimum wavelength for the detection of $SO_2$ by across-the-stack absorption of laser radiation, over a wide temperature range. If such data were known for other constituent gases as well, a complete model could be used to facilitate development of suitable monitoring instrumentation.
>
> "Although the above theory contains the temperature dependence explicitly, it must rely on independent measurements for predictions involving pressure-broadening of the lines. The rate of pressure broadening of $SO_2$ lines by air was measured by laser spectroscopy and found to be 12 MHz/Torr for the full width at half maximum (FWHM); this yields an atmospheric-pressure-broadened linewidth of 0.30 $cm^{-1}$. Similar measurements for ammonia ($NH_3$) in the 10 μm region produce values of 6.3 MHz/Torr and 0.16 $cm^{-1}$, respectively.
>
> "Experiments were performed to verify the fundamental theory related to remote heterodyne detection of atmospheric pollutant gases. Application of this technique would permit single-ended, passive detection from both stationary and mobile sources. It is shown that, based on information obtained here on the $SO_2$ emission band at 8.7 μm, concentrations of the gas as low as 10 ppm can be detected, essentially independent of range, if the gas temperature is 100 °C. For the same gas at 50 °C, the minimum detectable concentration is about 50 ppm, and the measurements become more

susceptible to changes in the background. Unfortunately, the present diode laser power capability is not sufficient to attain the ultimate remote heterodyne detection sensitivity, although progress is being made in both laser and detector technology.

"Several other applications were studied during the first phase of this program:

(1) Point Sampling – as has been demonstrated earlier, this technique using tunable lasers has the advantage of very high specificity by permitting testing at reduced pressure where overlap between adjacent absorption lines can be eliminated in most cases. With a 10-cm-long cell containing an $NH_3$:air mixture, and a tunable diode laser with 10 μW output power, the minimum detectable concentration was found to be 28 parts per million (ppm) using a line having 1 $cm^{-1}$/Torr absorption constant per unit pressure, and an operating pressure of 4.5 Torr. For this test second-derivative detection was used, which effectively enhances the desired signal.

(2) "White" cell operation – construction of a "White" cell permitted a path length of 7.3 meters to be used for point-sampling applications. Comparison of the signal-to-noise ratio using a 10-cm-long cell with that achieved by the "White" cell for identical gaseous concentrations showed the predicted enhancement; consequently, the minimum detectable concentration for the "White" cell is found to be about 0.3 ppm. Since these minimum detectable values are inversely related to laser power, it is clear that the use of tunable diode lasers in the milliwatt power range can yield much more sensitive point-sampling limits, in the low parts per billion (ppb) region.

(3) Long-path transmission – diode laser radiation was collimated with a lens and transmitted over a 75-meter path from one building to another. Although the experiment was preliminary, and no attempt was made to tune through any atmospheric $SO_2$ lines, a strong signal was received, indicating good potential for long-path transmission techniques using these devices.

(4) Interferences – some studies were made to find possible interferences between the spectral bands of certain other gases which may be found in the atmosphere and the 8.7 μm band of $SO_2$, by using the diode laser to scan portions of this band. Since $NH_3$ is used as the primary calibration standard for wavelength in this region, it can under certain conditions produce interference – however, there are only approximately 5% the number of $NH_3$ lines as $SO_2$ lines in this region. A broader test was to place a quantity of automobile exhaust in the test cell, at 1 atmosphere pressure, and tune the diode laser over a region constituting strong $SO_2$ absorption. No interference was found, despite the many gaseous components (including water vapor) in auto exhaust."

Work is continuing to produce a system using a tunable semiconductor laser for <u>in situ</u> monitoring of $SO_2$ in smokestacks.

E. D. Hinkley
A. R. Calawa

## REFERENCES


1. Optics Research Report, Lincoln Laboratory, M.I.T. (1971:1), p. 34, DDC AD-888823-L.
2. Op. cit. (1969:3), p. 24, DDC AD-867089.
3. Op. cit. (1969:2), p. 17, DDC AD-863265.
4. Op. cit. (1969:1), p. 13, DDC AD-855883.
5. Op. cit. (1970:1), p. 24, DDC AD-870404.
6. B. Edlén, J. Opt. Soc. Am. 43, 339 (1953).
7. J. Stock and G. Keller, Telescopes, G.P. Kuiper and B.M. Middlehurst, Eds. (University of Chicago Press, 1960).
8. J.B. Irwin, Astron. J. 71, 28 (1966).
9. Optics Research Report, Lincoln Laboratory, M.I.T. (1970:3), p. 35, DDC AD-882617.
10. G. Baur, N. Riehl and P. Thoma, Z.f. Physik 206, 229 (1967).

# III. LASER RADAR AND TRACKING

## A. LASER RADAR IMAGING

### 1. Introduction

The narrow field of view (FOV) detector, whose initial performance was previously reported,[1] has been used to investigate incoherent target return signatures. Calibration of the system was accomplished by using three Au-coated sphere segments of different, known radii of curvature. The vertical stabilizer, taken from an F-80 trainer aircraft, was used as a target for qualitatively investigating the correlation of incoherent signal returns vs position on the target from which the returns originate, as well as vs inclination of the target with respect to the line-of-sight. Finally, some preliminary measurements were made of the homodyned return from targets giving a Doppler shift.

### 2. Detector 44

A new detector was constructed and employed in the L-006 laser imaging system. The detector, shown in Fig. III-1, is a Cu:Ge sample taken from the same doped boule as the previous

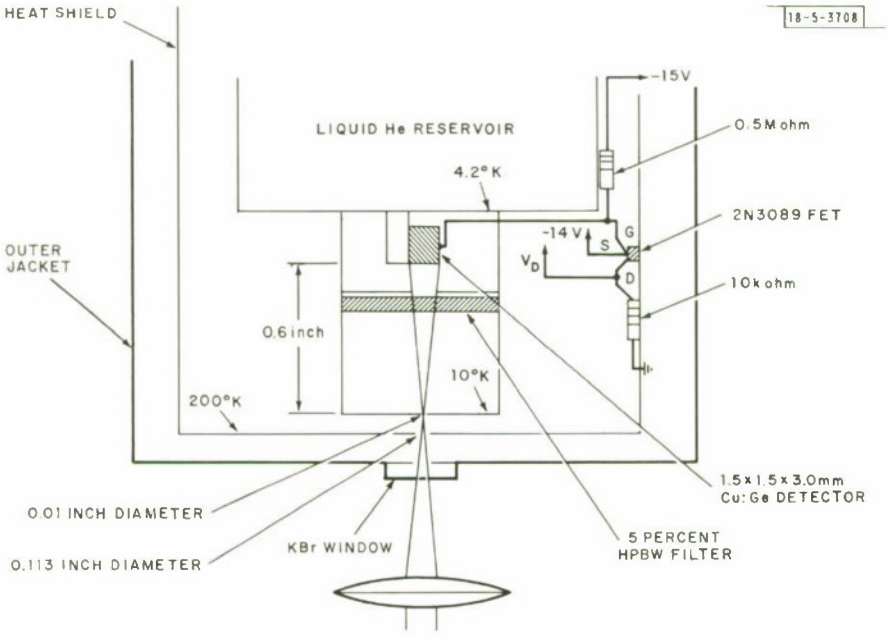


Fig. III-1. 10.6-μm detector 44 (not to scale).

detector (57) that was, and still is, employed primarily for coherent detection, where nominal 1 mW local oscillator power is used.* The new detector has a smaller (1.5 × 1.5 mm) cross section, and is covered by a blackened top hat that is cooled by the liquid helium reservoir. The roof of

* Both doped samples kindly supplied by Theodore M. Quist.

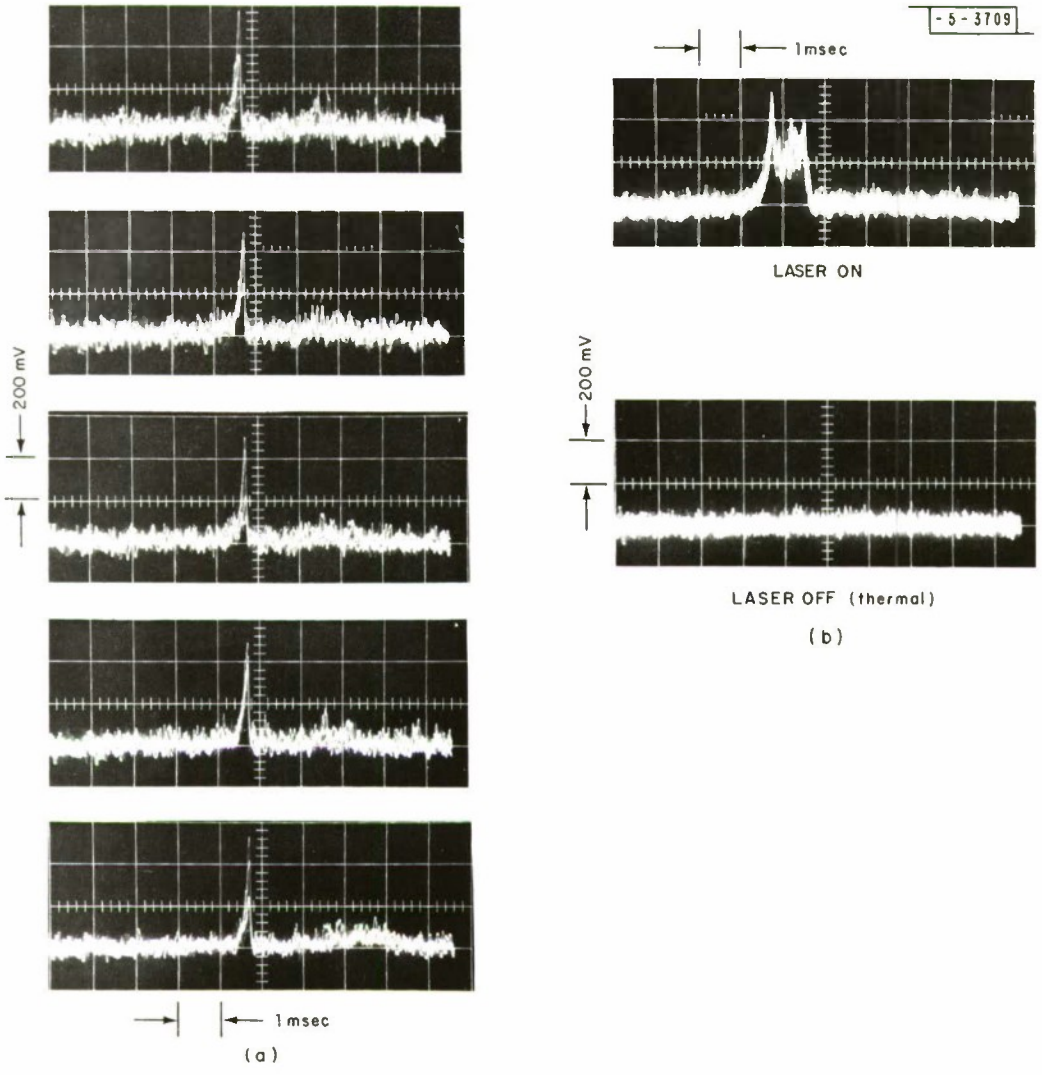


Fig. III-2. Display af returns fram calibratian run an (a) 40-cm$^2$ crass-section target; (b) scatter plate.

the top hat has a 0.010-inch-diameter hole directly over and 0.6 inch from the front face of the Cu:Ge sample. The hole serves as a cold aperture to limit the thermal FOV of the detector to 100 mrad. A diffraction-limited 4-inch focal-length lens placed in front of the detector could just focus a collimated, 1-cm-diameter, 10.6-μm return beam through the hole and onto the Cu:Ge sample, as shown in Fig. III-1. For such a focused return beam, the 0.01-inch-diameter hole serves as an aperture to limit the detector's FOV to 2.5 mrad. (Because a 10X telescope is used to obtain the collimated 1-cm-diameter beam, the FOV of the detector projected onto the target plane in the L-006 system is reduced to 250 μrad.)

With the top hat closed off, the Cu:Ge sample exhibited a resistance of about $4 \times 10^{9}$ ohms. The room temperature radiation incident on the sample from the 0.01-inch-diameter hole (approximately $3.46 \times 10^{-9}$ W through the filter) reduces the resistance of the sample to $6.8 \times 10^{8}$ ohms. (With a 15 V bias applied, the 0.01-inch-diameter hole caused an increase in current from 3.8 to $22 \times 10^{-9}$ A. Assuming the above value for the room temperature radiation incident on the filter, one finds the responsivity of the sample to be 5.2 A/W.) The responsivity was separately measured using a 600°C blackbody radiation source and found, within experimental error, to be between 5.4 and 6.2 A/W.

The detector and FET amplifier, combined, have a 3-dB bandwidth of 22.5 kHz. The FET amplifier has a gain of 8, and serves to reduce the output resistance across which the detector voltage can be measured, from the 0.5 megohm detector load resistance to the 10 kohm load resistance of the FET. This facilitates connecting useful lengths of cable to the detector dewar without having cable capacitance lower the detector bandwidth.

### 3. Calibration

A-scope displays of returns obtained using this detector in a calibration run are shown in Figs. III-2(a-b). In Fig. III-2(a), repeated single-circle scans were made across a section of a Au-coated sphere mounted in the target plane of the L-006 system. The cross section of the sphere section was 40 $cm^2$. Figure III-2(b) shows a typical return from a scatter plate. It was overcast and raining lightly on the day the calibration run was made. As a consequence, no thermal return was observed when the laser was off.*

Calibration of the L-006 system proceeded by averaging five traces for each of three sphere sections with known cross sections. The results, along with rms error bars, are plotted in Fig. III-3. The observed voltage is 800X the actual voltage across the detector. Six different scans of the scatter plate were averaged by dividing each scan into 5 increments equivalent to 2.25 inches. Thirty values were then used to compute the average and rms observed voltage of the return from the plate. The results were then placed on a good-fit line running through the sphere-section data of Fig. III-3. Results indicate that the average return from the plate is equivalent to about a 23-$cm^2$ cross section target.

One can estimate the return from the scatter plate, which was measured at the University of Michigan[2] to be Lambertian for viewing angles beyond 5° from the normal and to have a reflectance in excess of 0.95. The returned power should approximately be given by

* Compare with the A-scope trace of a thermal return in Fig. III-8, p. 48, Ref. 1.

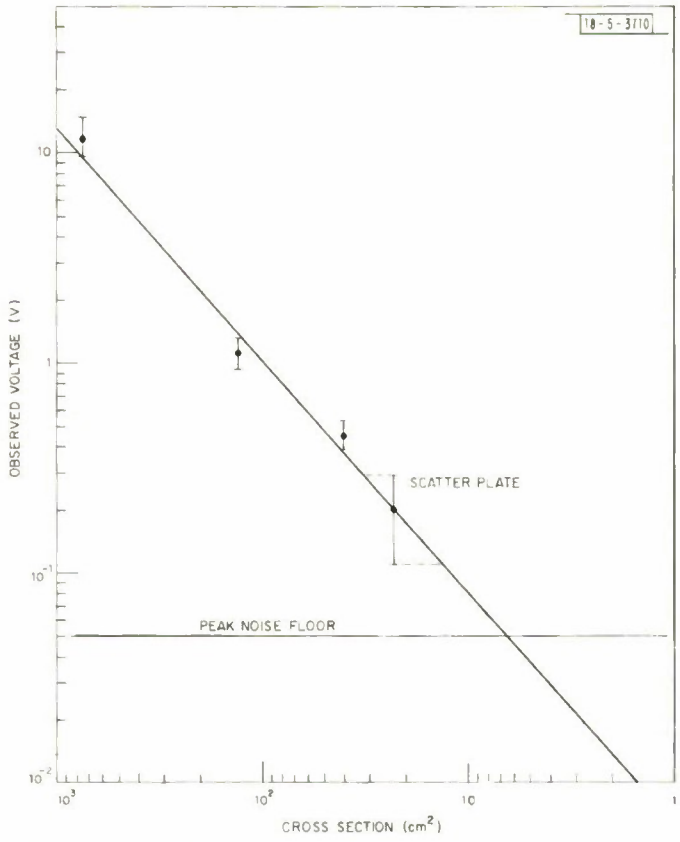


Fig. III-3. Incoherent detection – calibration curve: observed voltage vs cross section.

$$P_R = \eta_R \eta_T P_T \frac{\Omega_R}{\pi} \tag{III-1}$$

where

$P_R$ = returned power

$\eta_R$ = receiver efficiency

$\eta_T$ = transmit efficiency

$P_T$ = transmit power

$\Omega_R$ = receiver FOV

(Atmospheric loss over the 61-m path is absorbed in $\eta_R \eta_T$.) On the other hand, cross section is defined by

$$P_R = \eta_R F_i \frac{\Omega_R}{4\pi} \sigma$$

$$= \eta_R \eta_T \frac{P_T}{A} \frac{\Omega_R}{4\pi} \sigma \tag{III-2}$$

where

$F_i$ = incident radiant flux on target

$\sigma$ = cross section

A = target illumination area

Equating (III-1) and (III-2), one finds

$$\sigma = 4A \qquad \text{(III-3)}$$

Thus, for a Lambertian scatter plate that is large compared with the illumination beam's area, the cross section is just four times the area. For the L-006 system, Eq. (III-3) gives an estimate of 11.4 $em^2$ for the scatter plate cross section.

The 23-$em^2$ cross section observed experimentally indicates that the return from the scatter plate, when measured monostatically, is 3 dB greater than estimated. Previous measurements, made using two sphere sections and a retroreflector as calibration standards, similarly showed the scatter plate return to be larger than estimated.

### 4. Signature

Another set of measurements was made on the scatter plate in which the different scan loci were carefully controlled. Figure III-4 shows the scanning format. The scan was placed on top of the scatter plate and lowered by 1.83-inch increments at the target. The A-scope signatures were found to be repeatable. The resultant individual scan returns were then hand traced from photographs to give Fig. III-5. Scans 3 through 8 arise from the plate and not the frame in which the plate is held. As before, these traces were individually divided into five 0.2 msec increments, corresponding to 2.25 inches along the scan locus, and the thirty data points were averaged. The result was an average observed voltage (again, 800X the actual detector voltage) of 380 mV. The rms variation of these points was 180 mV. It is evident from Fig. III-5 that the large error bars

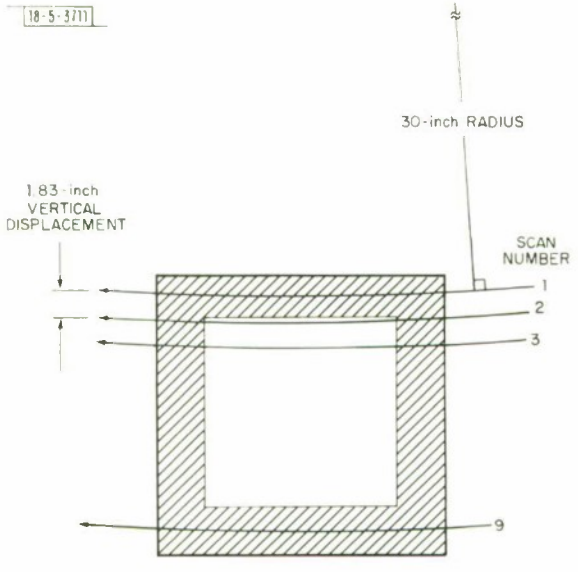


Fig. III-4. Scanning format of fromed Al scatter plate.

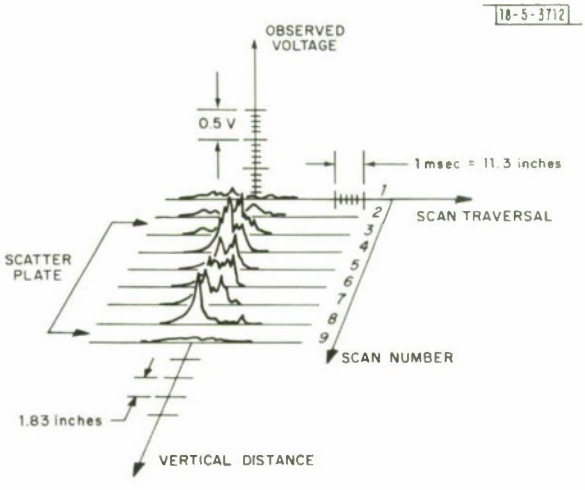


Fig. III-5. Scatter plate – cross-section profile.

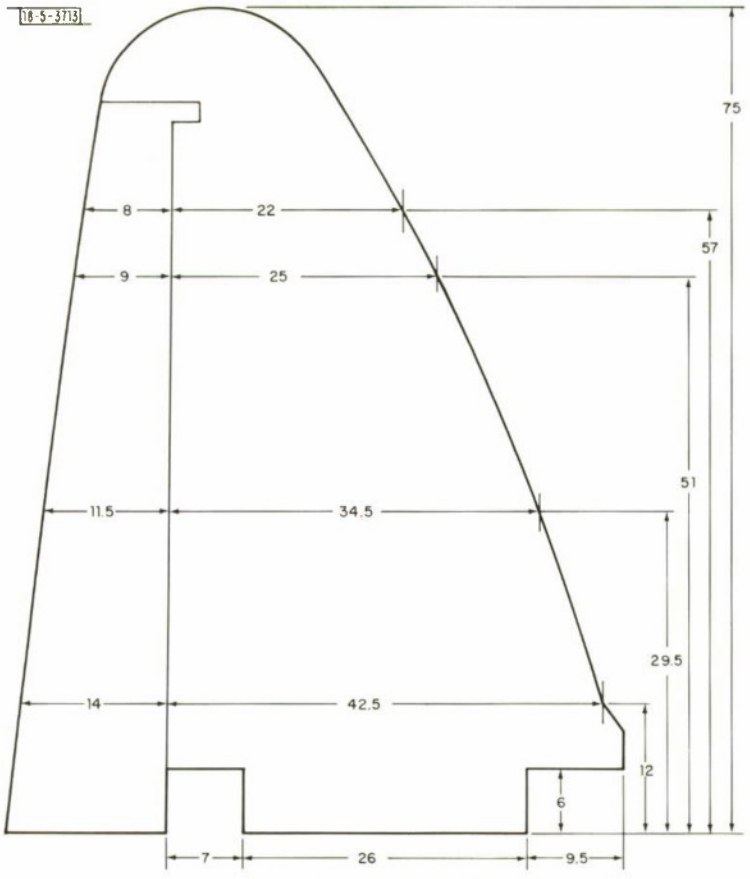


Fig. III-6. Vertical stabilizer of F-80 trainer (measurements in inches).

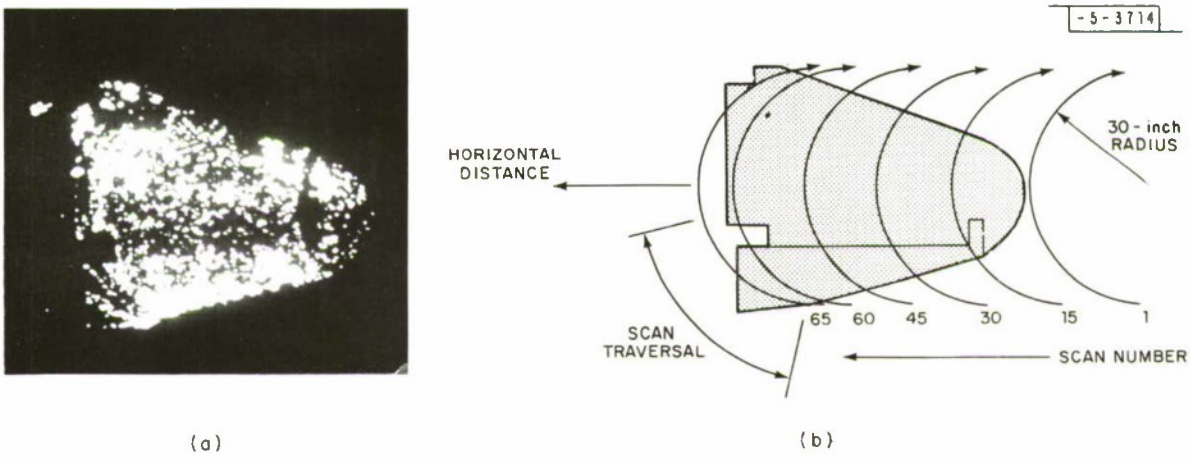


Fig. III-7. F-80 vertical stabilizer: (a) image (hamadyned return); (b) scanning format.

bounding the average return from a scatter plate in Fig. III-2 arise, not primarily from experimental error, but rather from the variation of the return from different segments of the plate.

The data on the scatter plate were taken on an overcast day when no thermal return was observed. The 350 mV average return, which [from Figs. III-2(a-b)] corresponds to an experimental cross section of 23 $cm^2$ on that day, was used as a calibration for measurements made on the same and several subsequent days. (Power levels and typical scatter-plate returns were monitored throughout the measurements.)

### 5. F-80 Vertical Stabilizer

The vertical stabilizer from the tail section of a scrap F-80 trainer was examined. Figure III-6 is a sketch of its broadside dimensions. Figure III-7(a) shows an image of the tail section as viewed on the mount when it had been oriented so that its broadside surface was approximately normal to the line-of-sight. This orientation corresponded to an angle of about 210° on the mount's azimuth control. Figure III-7(b) shows the scanning format. The scan was placed horizontally adjacent to the stabilizer and incremented past it in 1.35-inch steps in the target plane. Figure III-8 shows the resultant cross-section profile, obtained in the same manner as Fig. III-5. (Note that the horizontal coordinate does not represent a linear distance along the stabilizer, but gives the distance along the circular trajectory of the scan as shown in Fig. III-6.) Scan 10 and scans 60 through 65 required reducing the gain of the post-detector amplifier by a factor of 10, thus indicating values of $\sigma/10$ in Fig. III-8.

Data were taken on a subsequent day when a thermal return from the stabilizer was observed. The inclination of the stabilizer was changed by rotating the azimuth position control of the mount. This rotated the stabilizer about the horizontal axis as viewed in Fig. III-7. A single scan, approximately in the location of Scan 50 of Fig. III-8, was then observed. Figure III-9 shows the resultant change in return profile as a result of incrementing the stabilizer inclination by 0.05°. The return shown in Fig. III-9 is due to both reflected laser energy and thermal energy from the stabilizer. To obtain the laser cross section, $\sigma$, one must subtract the equivalent thermal cross section, $\sigma_T$. The thermal return (laser off) was not obtained for each increment, for it was observed to change very little. However, the thermal return, or $\sigma_T$, is shown for 210° and can be used to judge the contribution of $\sigma_T$ at other inclinations as well.

Figures III-10 and III-11 show the cross-section profile variation when the stabilizer inclination is incremented by 0.5° and 5.0°, respectively. The scan locus for these two measurements is the same, and is close to Scan 50 of Fig. III-8, but is not the same as that used to obtain Fig. III-9.

It is seen from Fig. III-8 that, like the scatter plate, various segments of the stabilizer have widely varying values of cross section. Peaks in cross section appear to be correlated over distances ranging from a few to tens of inches. Figures III-9 through III-11 indicate that, although differing in fine structure over small inclination changes, peaks in the return of a single scan are correlated over inclination changes of up to 10° or more. More quantitative data about the signature statistics will be obtained by use of a computer.*

* In collaboration with N. Meyerhoff.

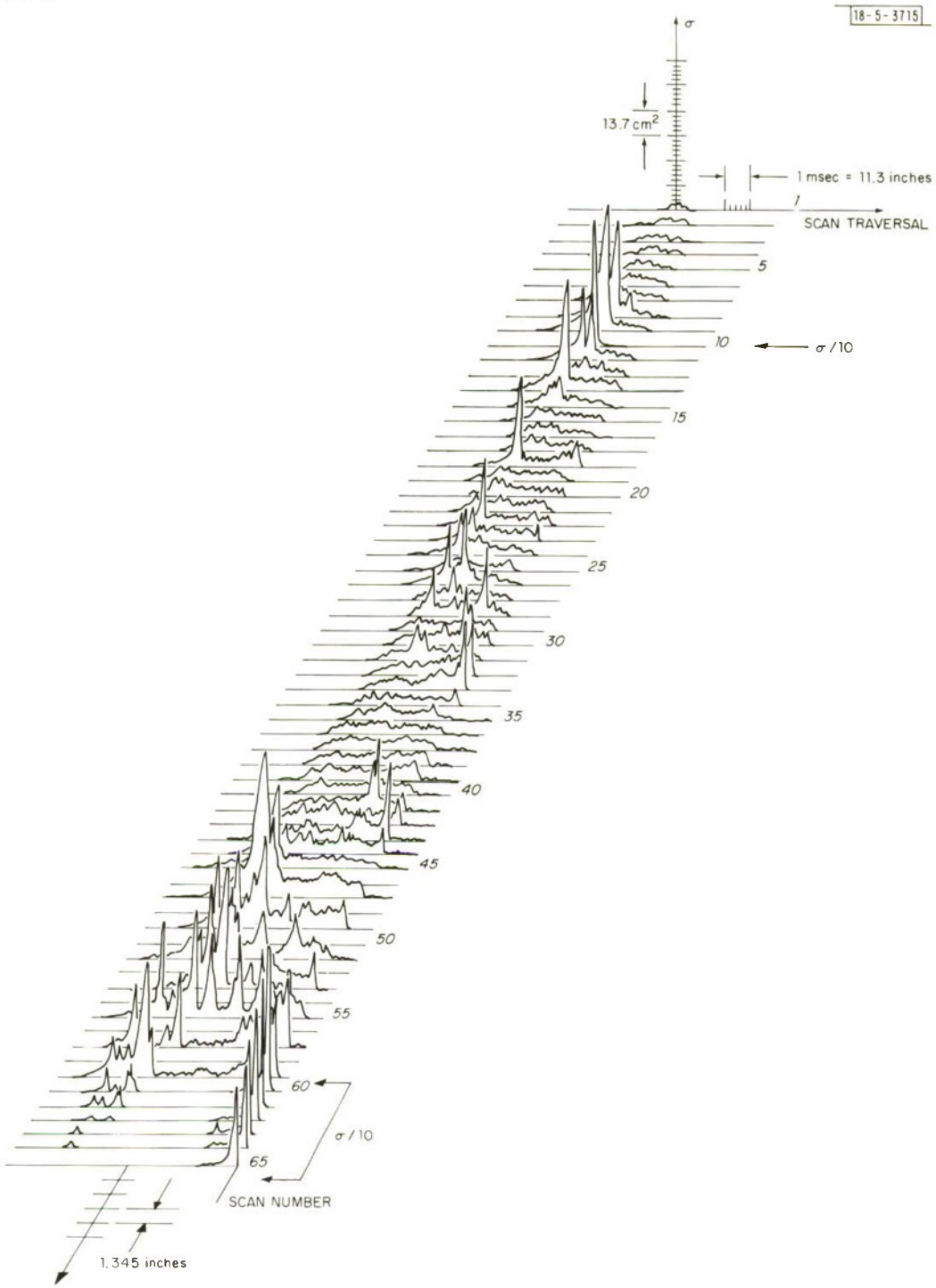


Fig. III-8. F-80 vertical stobilizer – cross-section profile.

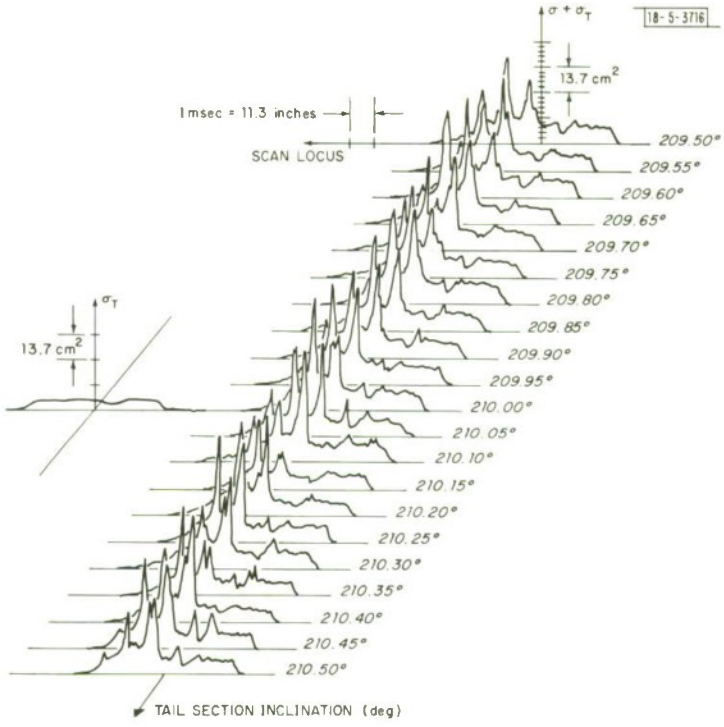


Fig. III-9. F-80 vertical stabilizer – single-scan crass-sectian profile vs inclinotion (0.05° increments).

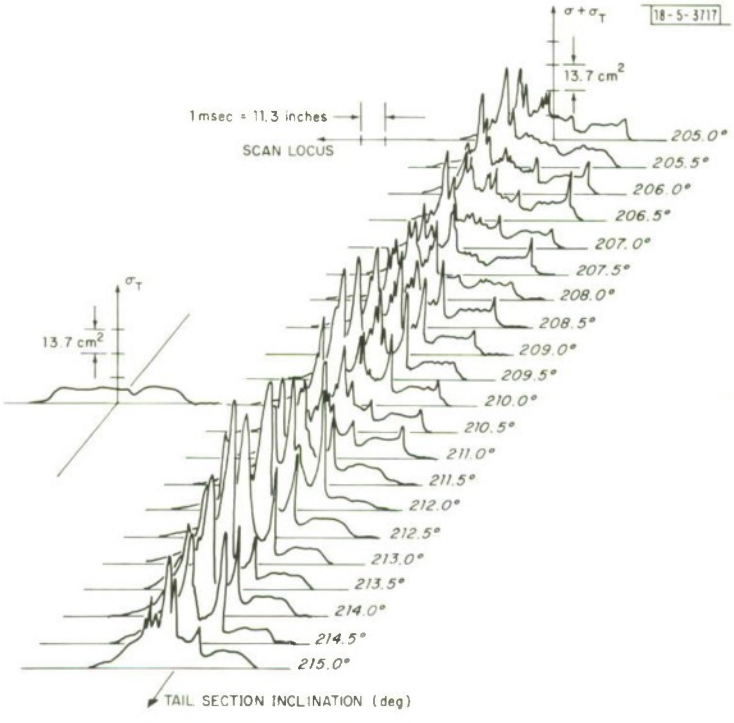


Fig. III-10. F-80 vertical stobilizer – single-scan cross-section profile vs inclinotion (0.5° increments).

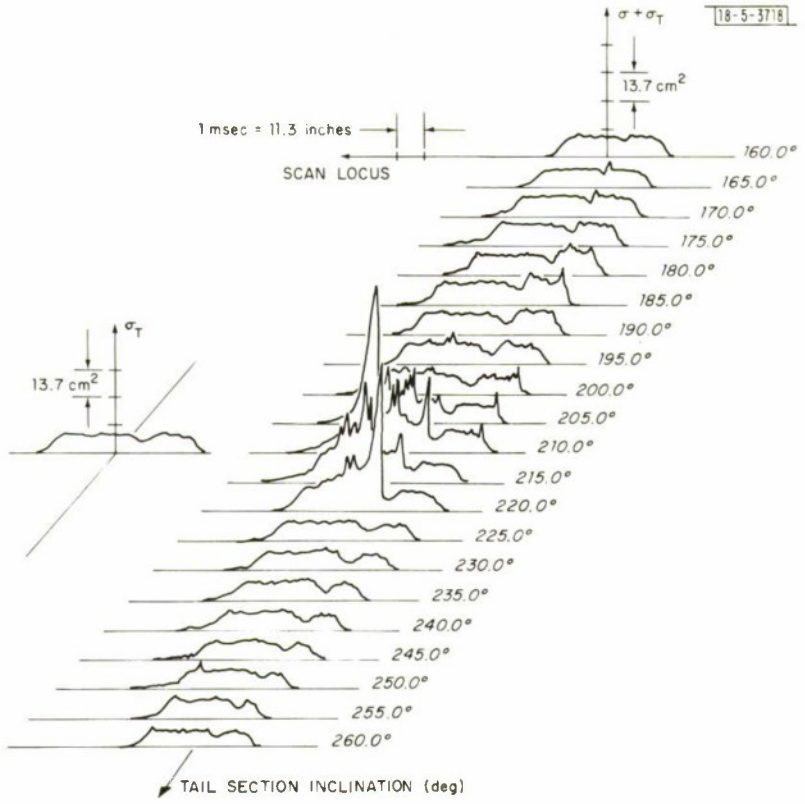


Fig. III-11. F-80 vertical stabilizer – single-scan cross-section profile vs inclination (5.0° increments).

### 6. Doppler

Although investigated by several workers,[3,4] the Doppler shift due to segments of a rotating sphere placed on the target mount was measured. Figure III-12 shows the geometry. A 12-inch-diameter, hollow aluminum sphere, that had a rough surface was rotated at about 1/5 rps. The sphere was very imperfect, compared with 10.6-μm tolerance, and wobbled somewhat when rotated. At 0.2 rps, one expects the outer edge of the sphere to give a Doppler shift of 37.7 kHz. Figure III-13 shows the spectrum of the homodyne return resulting from incrementing the laser beam from the center to the outer edge of the sphere. Note that the two sidebands shown are due to the spectrum analyzer's sweep display. They correspond to two measurements of the same Doppler-shifted return, which was positive with respect to the laser frequency, in this case. The incremented beam locus was approximately along the horizontal great circle of the sphere. The results show that the Doppler shift due to segments of a spinning sphere can be observed over the range and with the components of the L-006 system.

The effect of illuminating a central section of a 2-inch-diameter, spinning steel ball was measured. The ball was roughened by emery cloth and placed on the mount, where it was illuminated by the approximately $\frac{3}{4}$-inch-diameter beam. By finely peaking the return with beam-position adjustments, a central area containing the radar point was obtained. Figure III-14 shows the spectrum of the homodyne return as a function of rotation velocity. In the display of

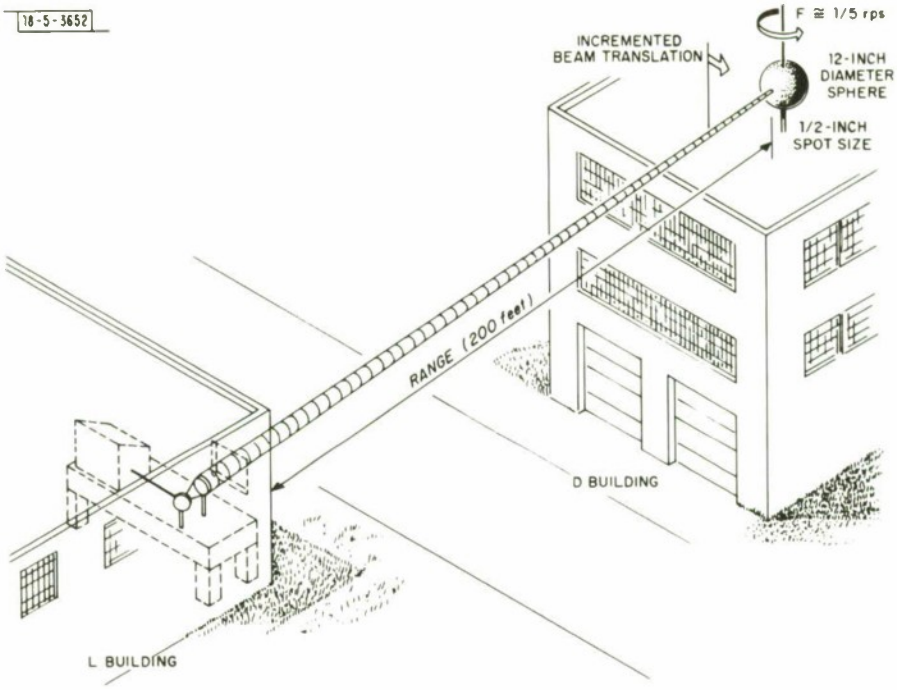


Fig. III-12. Geometry for Doppler study.

the figure, both positive and negative Doppler-shifted frequencies of the return are folded, and the double sidebands shown correspond to two measurements of the same folded spectrum. The inercased broadening vs increased rotation velocity is clearly observed. The limit on the spectrum of the folded Doppler shift, assuming a $\frac{3}{8}$-ineh-radius beam at the target, is shown on Fig. III-14 in parentheses under the rotation rate.

In an attempt to evaluate the Doppler shift resolution of the L-006 system, the speetrum of the return from a retrorefleetor that was translated, unfortunately not very uniformly, along the linc-of-sight was measured. Figure III-15 shows the results. Note the harmonie content of the translational motion at 0.35em/sec. The 0.15-em/see speetrum indicates that a Doppler shift as low as 300 Hz ean be identified. Further measurements with a more uniformly moving meehanieal translation stage are planned.

W. E. Bieknell
D. H. Bates

## B. InSb 10.6-$\mu$m POLARIZATION ROTATOR

An effort has been undertaken to construct a 10.6-$\mu$m isolator using InSb eooled to liquid $N_2$ temperature.[5] The aim is to obtain an isolator capable of handling several tens of watts with minimum loss and optical beam degradation. To obtain the optimum free-earrier concentration (N), a figure of merit (F) has been evaluated that takes into aeeount the negative interband Faraday rotation effeet in InSb.[5] The figure of merit for InSb is

$$F = \frac{1.57 \times 10^{-4} N^{3/4} - 6.7 \times 10^{-3}}{1.54 \times 10^{-18} N^{13/12}}$$

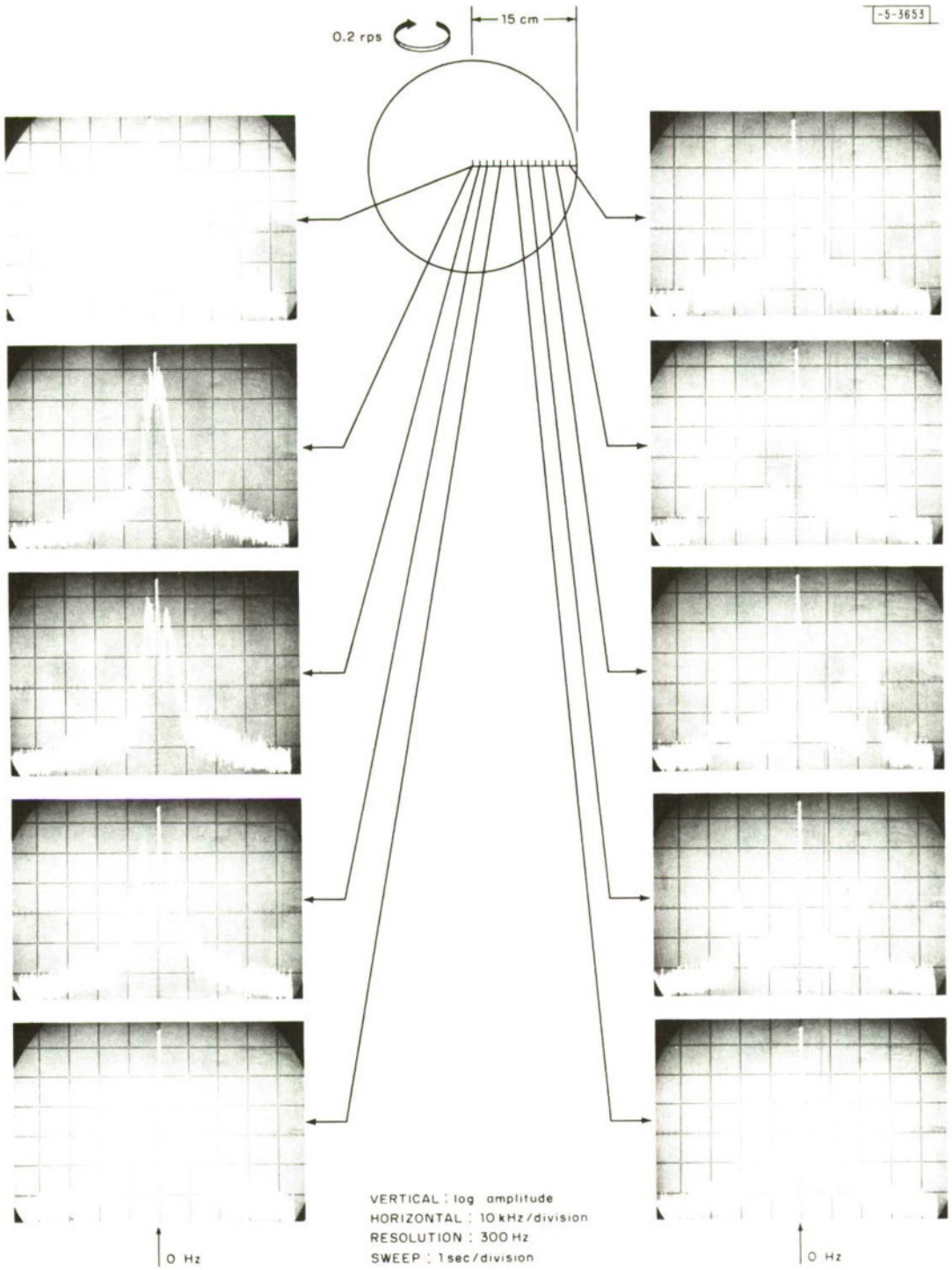


Fig. III-13. Doppler shift due to segments of o rototing sphere.

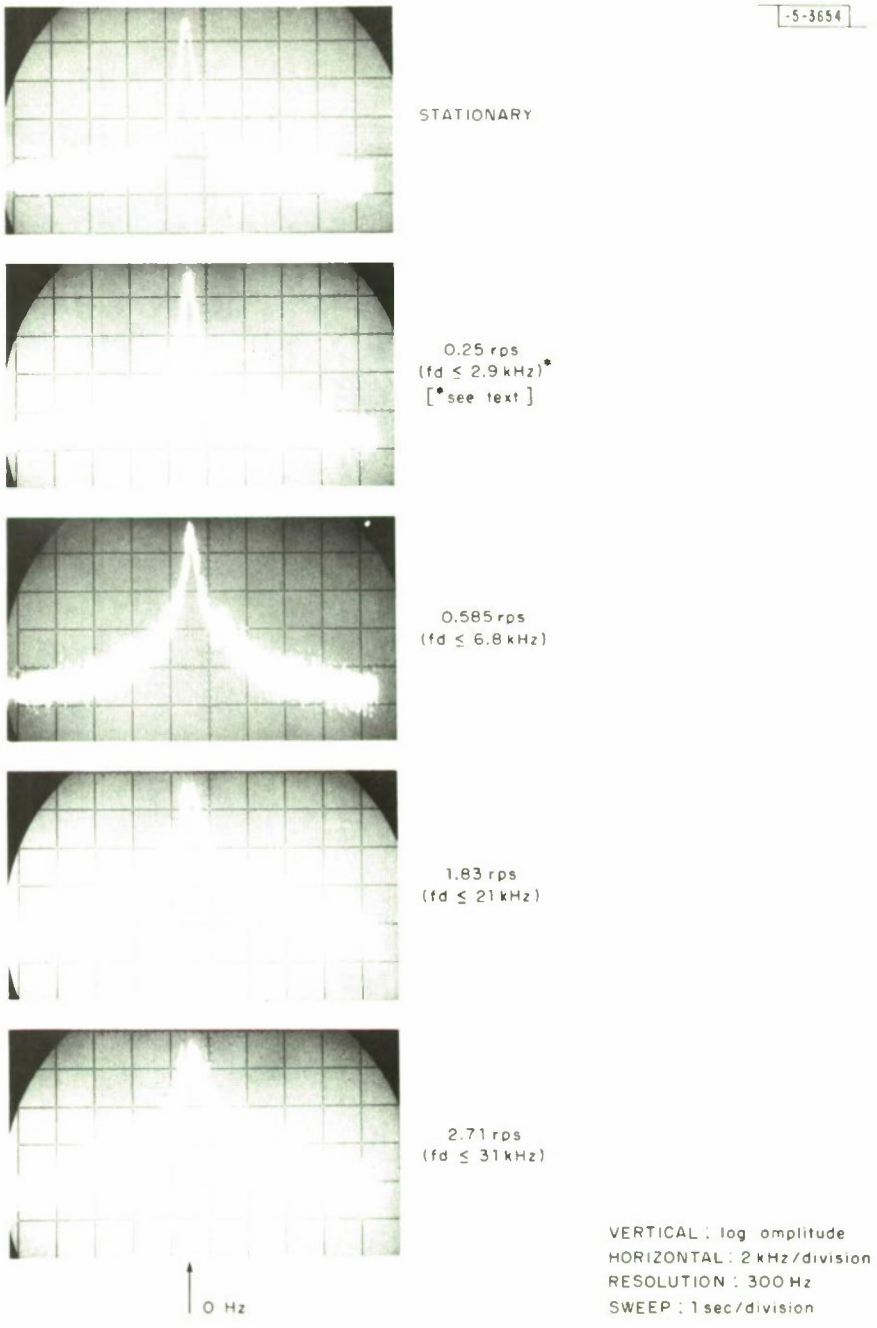


Fig. III-14. Doppler spread due to a rotating 2-inch-diameter steel ball.

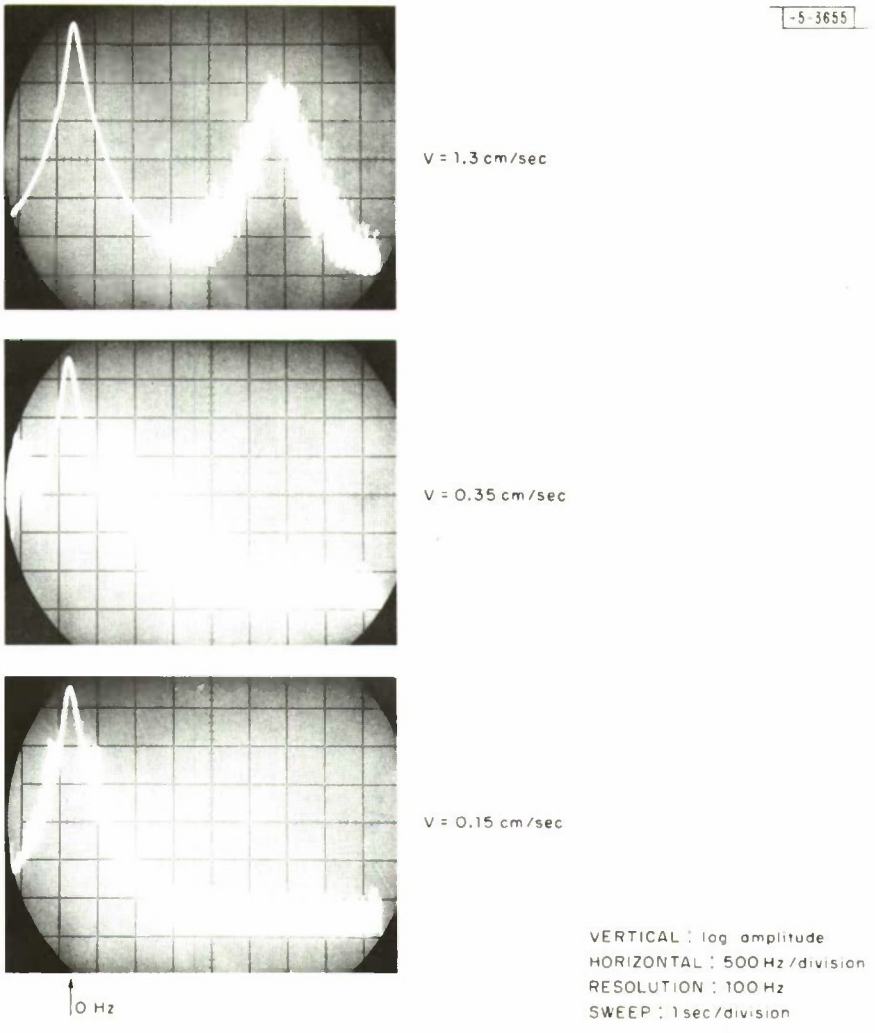


Fig. III-15. Doppler shift due to a retro-reflectar translated alang the line-of-sight.

where F is in degrees/G. The figure of merit in terms of observables is $F = \Theta/2\alpha\ell B$, where $\Theta$ is rotation of polarization, $\alpha$ is the absorption coefficient, $\ell$ is the sample thickness and B is the magnetic field.

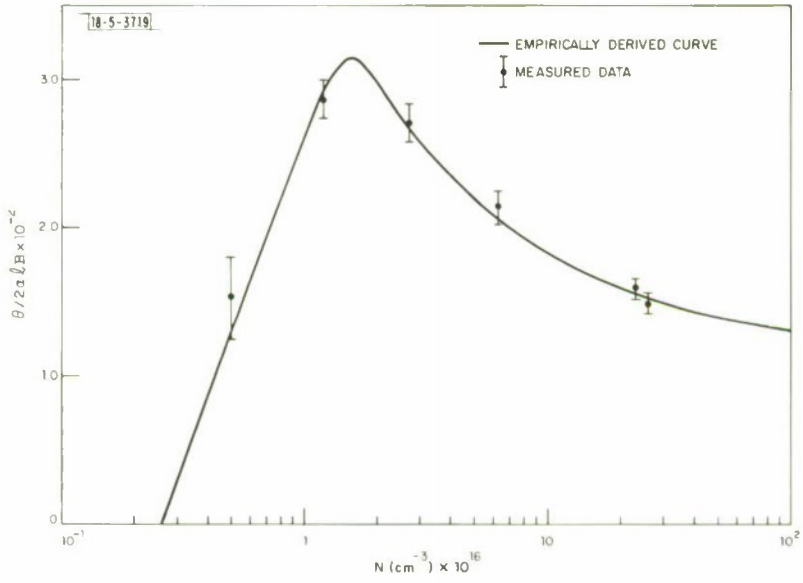


Fig. III-16. Figure of merit vs free-corrier concentration.

Experimental results have confirmed the phenomenological model used to calculate F. Figure III-16 shows experimental points placed on the calculated figure of merit vs concentration plot. Figure III-17 shows experimental points on a plot of Verdet constant ($\Theta/B\ell$) vs concentration.

Absorption was measured by comparing input and output power as observed on a thermopile and accounting for the reflectivity of the InSb and KBr window surfaces. Rotation was measured by using a Brewster angle Ge flat for a polarizer.

Incident CW powers of 55 W were applied on 2.0- and 2.5-mm-thick samples having a free-carrier concentration of $2.7 \times 10^{16}$ $cm^{-3}$ for up to an hour with no measurable change in output. This required a sample power dissipation of 10 and 12 W, respectively. The incident 55 W did not represent an upper limit to the power handling capabilities of the samples and the liquid $N_2$ dewar, but was the highest power source available at the time.

The samples were attached to a copper block $2 \times 1 \times \frac{1}{8}$ inch, as shown in Fig. III-18. Cooling was accomplished by placing a $1 - \times \frac{1}{2}$-inch flange at the end of the bar in contact with a liquid nitrogen reservoir (approximately 2 liters). Note that the InSb was not in direct contact with the liquid nitrogen.

When a 15 W beam with circular symmetry was incident on a sample, the output beam intensity profile showed a marked distortion. The profile was elliptical rather than circular. This distortion has been attributed to the method used to attach the sample to the copper block. The sample was rigidly held by an adhesive bonding at two points on the periphery of the sample. As the sample cooled, or became heated locally, it could expand or contract in one direction, but not in the other. The resultant change in the index of refraction due to an asymmetric strain

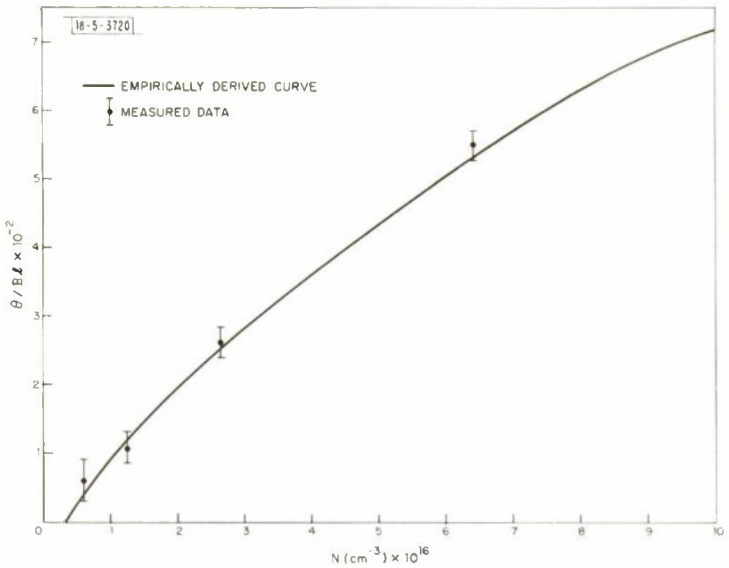


Fig. III-17. Verdet constant vs free-carrier concentration.

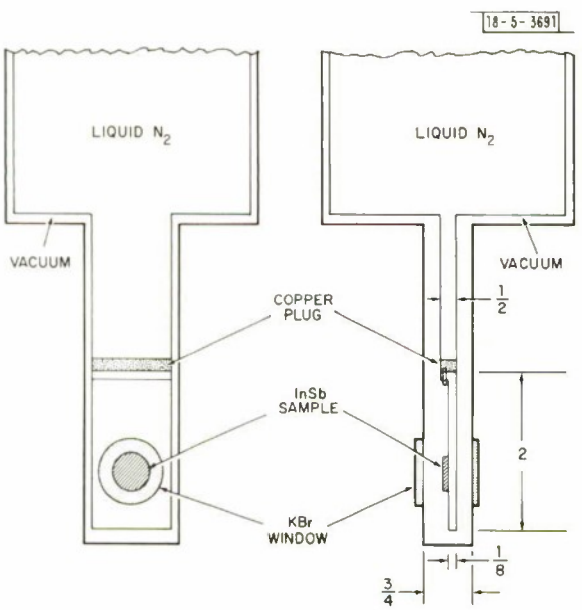


Fig. III-18. InSb liquid $N_2$ assembly (measurements in inches).

could have caused the elliptical profile. A new holder has been designed which will apply attachment pressure symmetrically, and will also permit symmetric expansion or contraction of the sample when under thermal stress.

L. Tomasetta
W. E. Bicknell
D. H. Bates

## C. PULSED MODE TRACKING

Automatic angle and frequency tracking in the pulsed mode was accomplished during this period subsequent to installation of the manual range tracking and gating circuits (described in Sec. III-D) which are required to provide error signals for the angle- and frequency-tracking loops. The transmitter pulsing was performed by a rotating slotted disk shown in Fig. III-19 and located at the internal focus of the beam expander immediately following the master oscillator.

L. J. Sullivan
L. W. Swezey

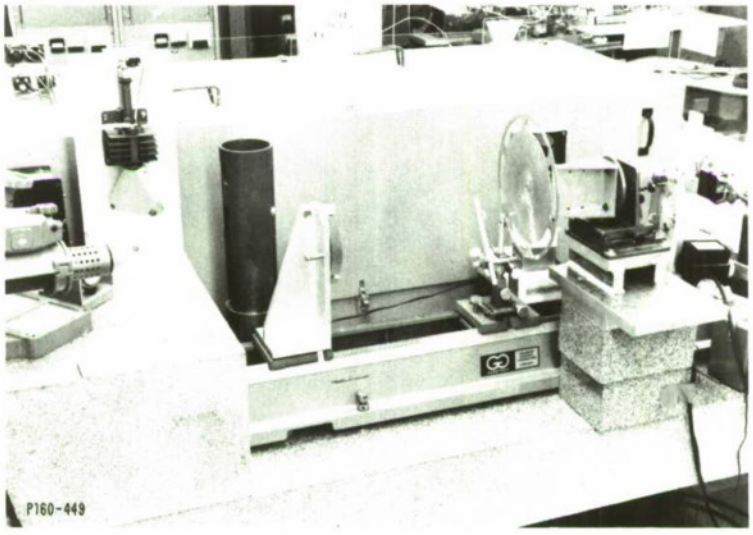


Fig. III-19. Pulsing disk.

## D. MANUAL RANGE TRACKER

In order to operate the Firepond Doppler laser radar in a pulsed mode it is necessary to range-gate and store the signal return from pulse to pulse. To accommodate this mode of operation, a manually operated range tracker was constructed. Figure III-20 is the block diagram of the manual range tracker.

The reference pulse, generated by chopping the He-Ne laser beam, is used to synchronize the tracking display on an oscilloscope, and also to generate a square wave. The fundamental component of the square wave is selected by filtering, and is phase shifted manually. At the zero-crossings of the phase-shifted fundamental, the reset generator is triggered. At the end of the reset pulse, the gate generator is triggered. The unipolar video output from the Doppler laser receiver is peak detected, stored, and used in the AGC and tracking error amplifiers.

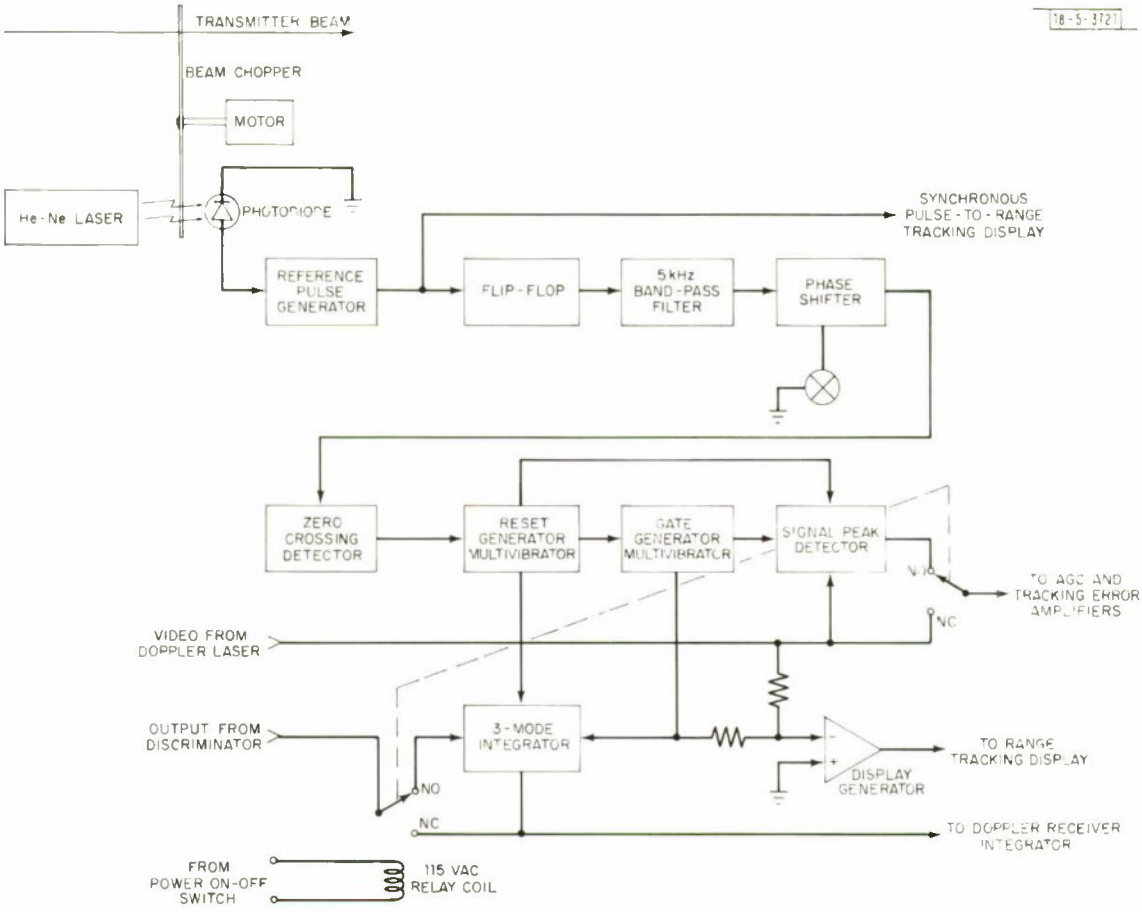


Fig. III-20. Manual range tracker – block diagram.

The bipolar output from the frequency discriminator is stored in the 3-mode integrator and provides the error signal for the frequency tracking loop of the Doppler receiver. For the tracking display, the range gate is combined with the video output from the receiver, then displayed on the oscilloscope.

Future plans call for the addition of automatic range tracking and a range digital readout capability.

M. D. Zimmerman

## E. $CO_2$ LASER OSCILLATOR FREQUENCY STABILITY

The frequency stability of the 1.5-m $CO_2$ laser oscillators at the Firepond Facility was measured by observing the variation in the beat frequency between two $CO_2$ laser oscillators. Frequency variations due to temperature changes, acoustic vibration and electrical noise were observed. The long-term stability was limited by the temperature drifts at the site. An approximately linear frequency drift of 10 kHz/min. was observed for a period of one hour. On a shorter time scale, acoustic pick-up was the most important source of frequency instability. Most of the acoustic pick-up was introduced by vibrations transmitted through the ground. These acoustic vibrations were due mostly to a resonant response at 40 Hz, and caused the frequency to vary

by approximately 300 Hz rms. The laser oscillators were also sensitive to loud noises. Frequency changes on the order of 10 kHz could easily be induced by this means.

Electrical noise in the discharge power supply and in the piezoelectric tuning elements was also observed to cause frequency instability. The frequency sensitivity to changes in discharge voltage was ~10 kHz/V and to changes in the piezoelectric tuning elements, ~250 kHz/V. The noise in the discharge voltage and piezoelectric tuning voltage gave rise to frequency variations of about 100 Hz rms, mostly due to the 60-Hz line and its harmonics.

J. Z. Holtz

## F. DOPPLER VELOCITY MEASUREMENTS

In order to determine the Doppler velocity measurement capability of the $CO_2$ laser radar at the Firepond Site, a target was placed at a distance of approximately 5.45 km, both on and near to the Groton Firetower. The target consisted of a corner cube mounted on a micrometer stage; the cube could be driven at a constant velocity of from 0 to 3 mm/sec and in this manner Doppler shifts of up to ~600 Hz could be produced.

The experimental arrangement used in making the Doppler measurement is indicated schematically in Fig. III-21. The local oscillator was offset in frequency by 5 MHz from the master oscillator and the frequency difference between the two oscillators was measured with a PbSnTe heterodyne detector. A beam-split portion of the master oscillator output was directed through the laser radar optics to the distant target and the return signal detected with a second infrared heterodyne detector. To measure the Doppler shift of the return signal, the electrical outputs of the two detectors were mixed and the difference frequency was spectrum analyzed.

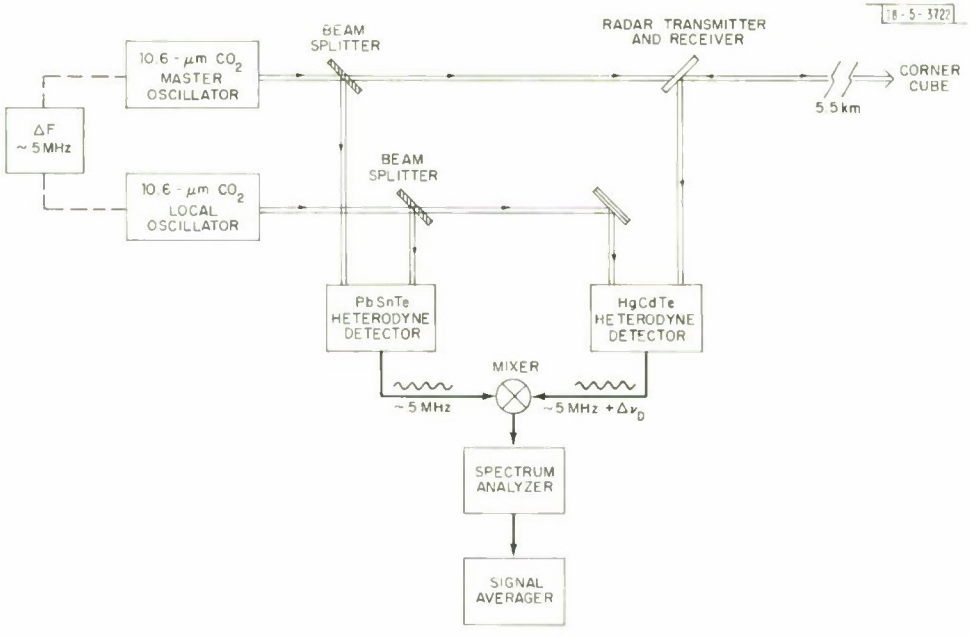


Fig. III-21. Experimental arrangement for Doppler velocity measurements – schematic diagram.

Two typical velocity measurements are shown in Figs. III-22(a-b). Figure III-22(a) is the spectrum with the moving corner cube on the Groton Firetower. The velocity of the cube was 1.8 mm/sec, corresponding to a Doppler frequency shift of 340 Hz. Figure III-22(b) is the spectrum with the moving cube located on the ground near the Firetower. The velocity of the target in this case was 1 mm/sec corresponding to a Doppler frequency shift of 190 Hz. In the case of the cube located on the Firetower [Fig. III-22(a)], the ability to measure the velocity of the cube drive was limited by vibration of the Firetower itself, which gave Doppler frequency shifts of ±100 Hz. When the cube was placed on solid ground, the accuracy with which the cube drive velocity could be measured was improved to ± 35 Hz or ± 0.19 mm/sec. This value of the Doppler velocities measurement accuracy is consistent with the limit set by the present frequency stability of the laser oscillators.

J. Z. Holtz

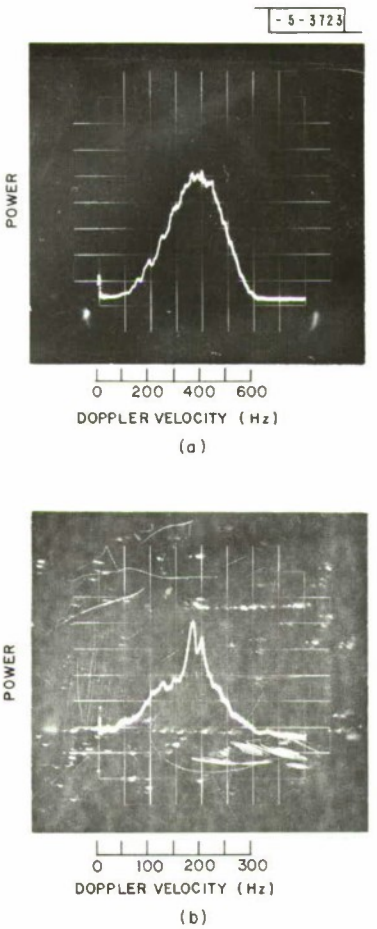


Fig. III-22. Doppler frequency spectrum of return signal: (a) target on Groton fire tower; (b) target on ground.

## G. ANNUAL AVERAGE TEMPERATURE, $H_2O$ PRESSURE AND $H_2O$ ABSORPTION OF 10.6-$\mu$m RADIATION AT FIREPOND

During the spring, summer and fall of 1969, 1970 and 1971, the atmospheric pressure, temperature and relative humidity were recorded at Firepond. The composite average temperature and range of extremes are shown in Fig. III-23. The diurnal variation averaged 22°F from the low to the high. These data were also used to calculate the $H_2O$ partial pressure. The average

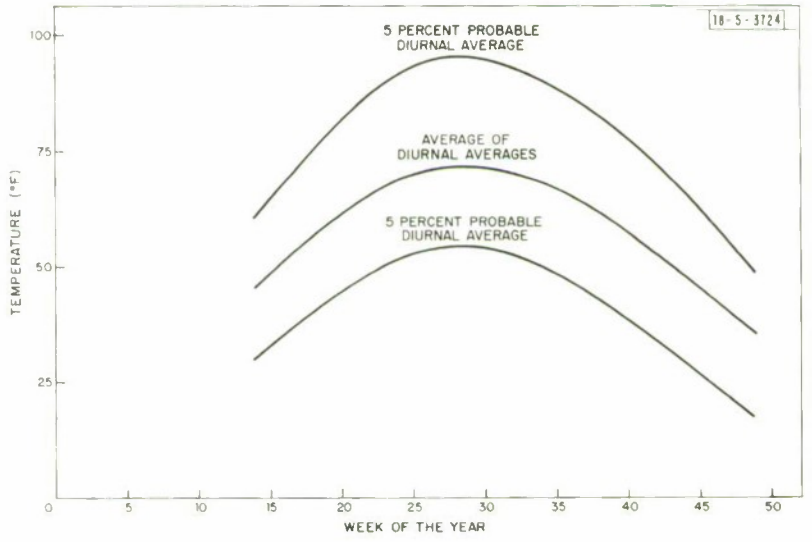


Fig. III-23. Temperature at Firepond – 1969, 1970, 1971. The average of diurnal average temperatures was computed from a composite for three years. Diurnal variation about the diurnal average is 22°F from a low before dawn to a high in mid-afternoon. Diurnal averages are between the 5-percent probable temperatures 90 percent of the time.

$H_2O$ pressure and range of extremes are shown in Fig. III-24. The temperature and $H_2O$ pressure for winter were not recorded continuously, because the meteorological station was not designed to work below 0°C. However, some winter data have been obtained from dew-point temperature readings taken at Hanscom Field and are summarized as the dashed portion of the curves in Fig. III-24. Over 24 hours in a given weather system, the $H_2O$ pressure varies very little being down and up about 8 percent from the daily average at 0400 and 1700, respectively.

The importance of the $H_2O$ vapor pressure to the operation of 10.6-$\mu$m radar can be seen in Fig. III-25, which shows the signal loss in –dB/km at sea level to $H_2O$ molecular absorption of the laser radiation from the laser transitions around P(20) of $C^{12}O_2^{16}$. This curve was computed from the formula determined by McCoy, et al.[6]

T. J. Gilmartin
W. J. Amisial

## H. CONVERSION TO DUPLEXED OPTICAL CONFIGURATION

During this period, all components for the duplexed optical configuration were completed. Early in November the original optical system was dismantled to make way for installation of the new optical configuration. The installation has essentially been completed and the system has been operated at low power.

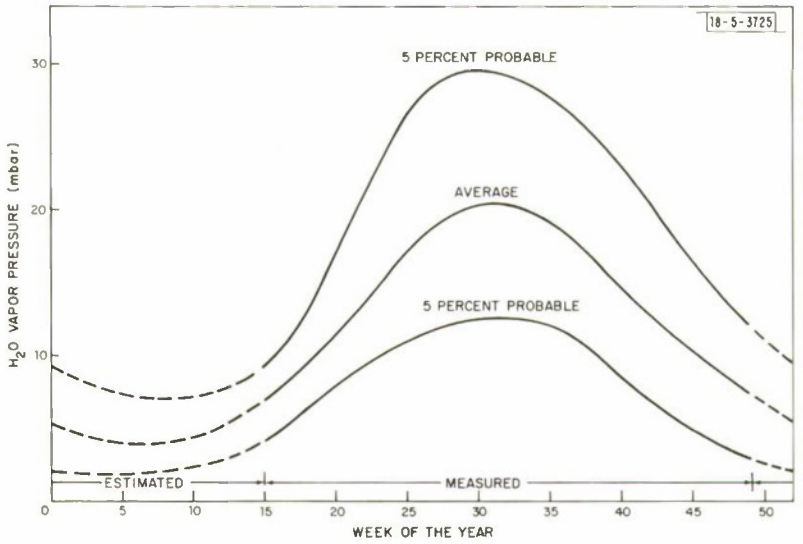


Fig. III-24. $H_2O$ vopor pressure ot Firepand – 1969, 1970, 1971. The average pressure wos computed from o composite for three yeors. Diurnol voriotion about the overoge is +8 percent in mid-ofternoon to −8 percent before dawn. Diurnal overoge pressure is between the 5-percent probable pressures 90 percent of the time.

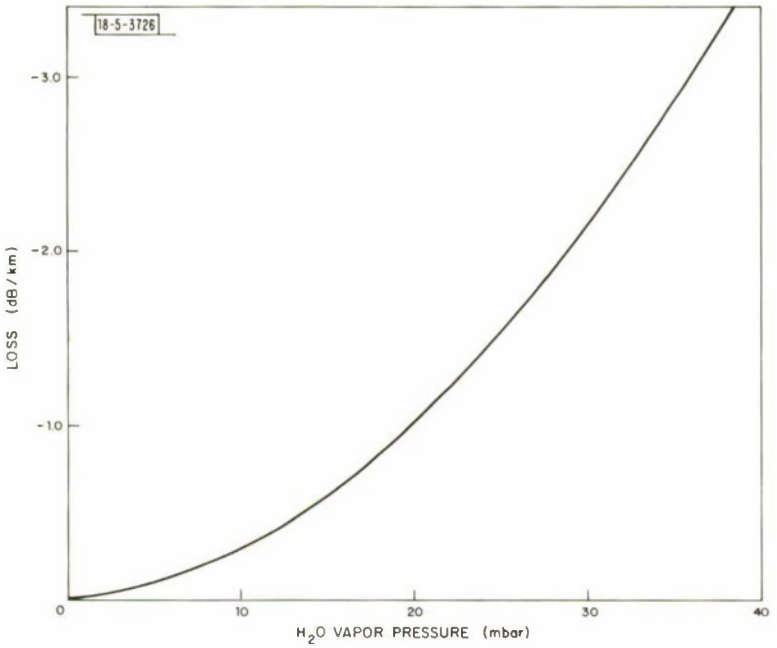


Fig. III-25. One-woy tronsmission loss ot seo level due to $H_2O$ vapor obsorption ot 10.6 μm.

The new configuration utilizes the same telescope for both transmitting and receiving. This provides a common optical path into which high speed scanning elements can be introduced to provide a rapid scanning capability for imaging purposes. This configuration results in identical beam widths for both received and transmitted beams, which should result in an increase in system performance of approximately 10 dB over the original system in which the transmitting aperture was less than a third that of the receiver.

The new system consists of a 20-inch decentered Newtonian telescope for both transmitting and receiving (Fig. III-26). Duplexing, i.e., switching between the transmitter and receiver, is performed mechanically by a rotating disk (Fig. III-27). The 24-inch-diameter disk is made of beryllium, one side of which has been polished to an optical flat and coated with gold over kanigen. The disk contains two rows of holes disposed circumferentially. The diameters of the holes in each row differ by a factor of two. The row of larger holes performs the duplexing function, while the smaller set of holes chops the output of the master oscillator to perform the pulse forming function.

The high speed scan format is the so called "Circular Palmer" in which a linear scan is superimposed in one coordinate on a large angle circular scan.

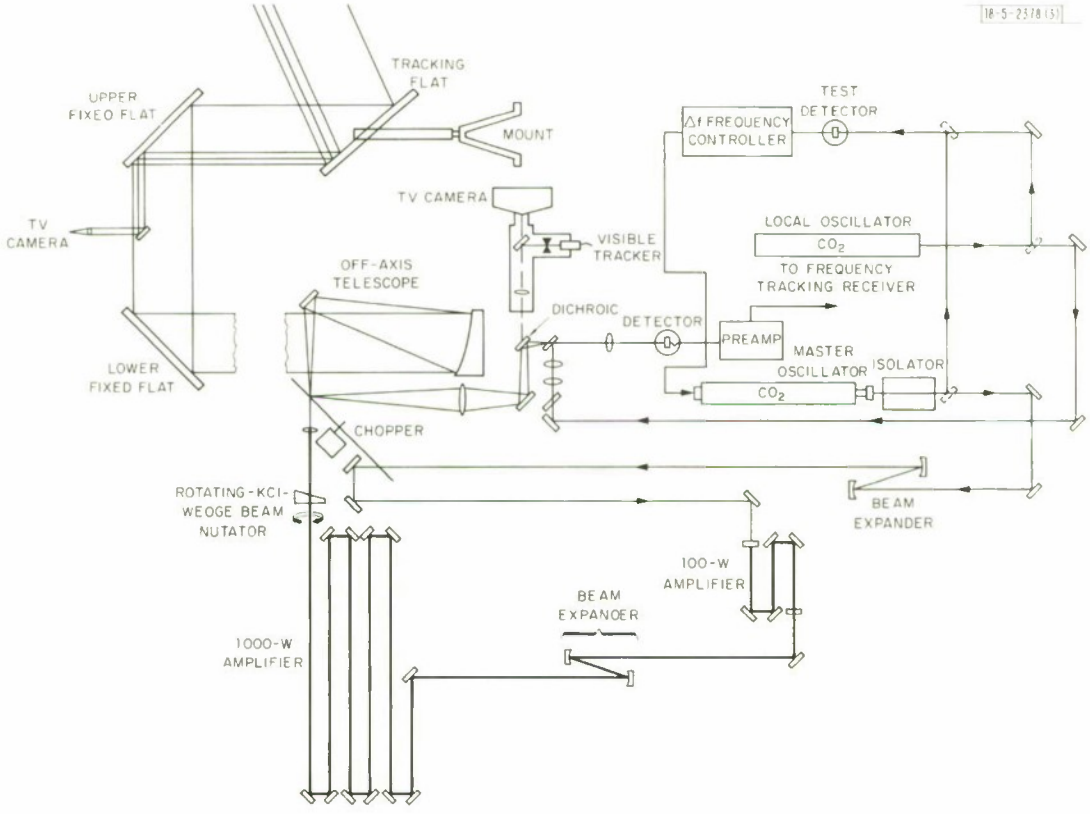


Fig. III-26. Optical schematic of duplexed system.

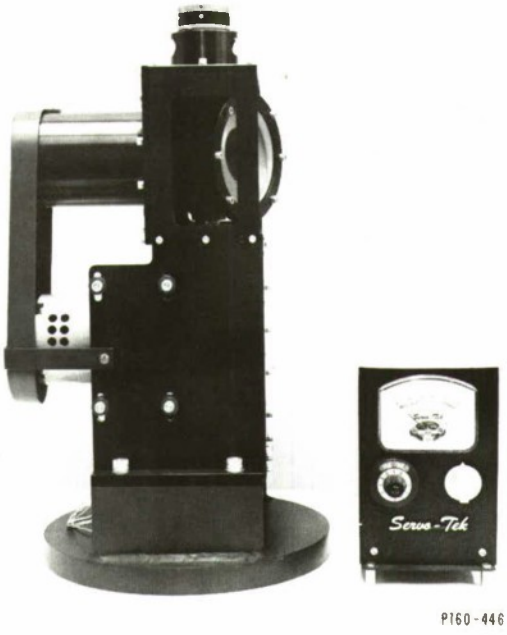


Fig. III-27. Switching disk.

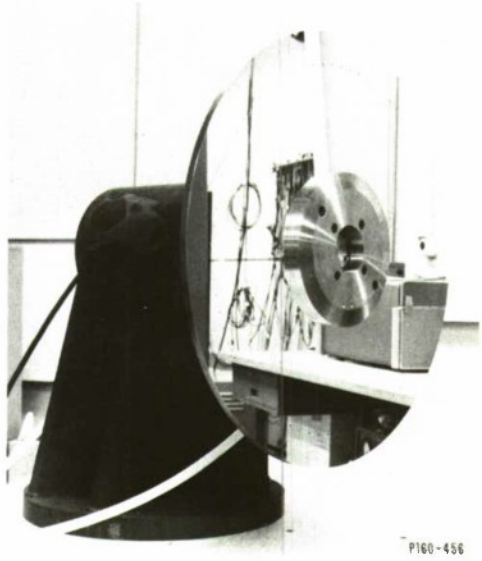


Fig. III-28. Beam scanner.

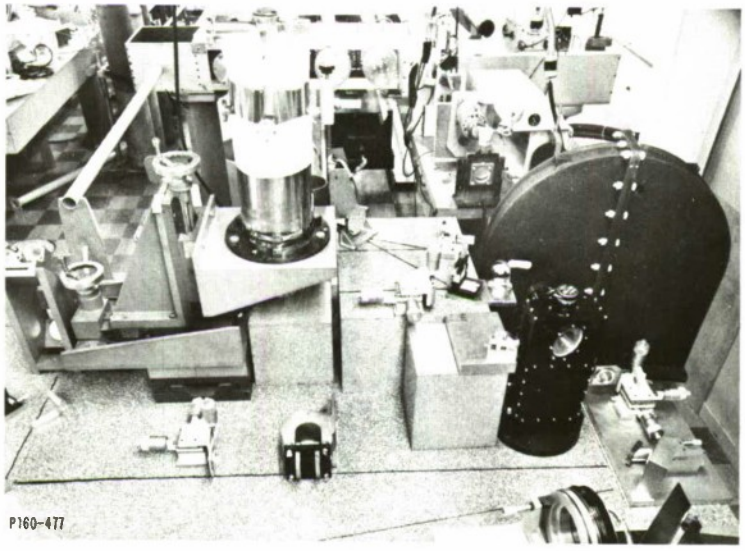


Fig. III-29. Duplexed optical system.

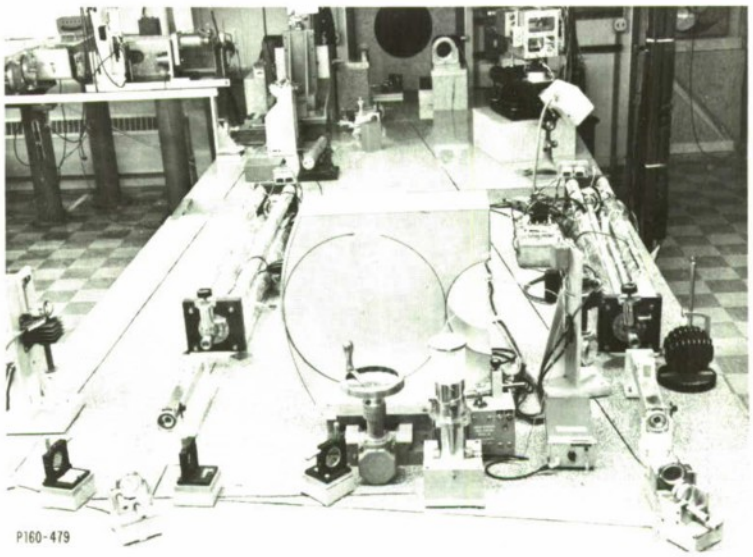


Fig. III-30. Duplexed optical system.

The scanning function will be performed by rotating and oscillating refracting elements made of KCl. The scanner, shown in Fig. III-28, is located in the conical telescope beam immediately after the switching disk.

The new optical system is shown in Figs. III-29 and III-30.

L. J. Sullivan
J. A. Daley, Jr.

## I. LARGE APERTURE BEAM PROJECTION AT 10.6 μm

At the Firepond Research Facility, a 48-inch-aperture telescope has been mounted in a fixed position to project a focused 10.6-μm spot into a tower shed at a range of 5.4 km. The purpose of this experiment is to measure the spot intensity distribution while monitoring the modulation transfer function (MTF) of the atmosphere at 0.6328 μm, in order to measure directly the atmosphere's effect on large aperture optics at 10.6 μm and to establish the relationship between the atmosphere's optical quality at these two wavelengths. The 10.6-μm image will be visualized and measured by means of an AGA thermovision system, which will view the IR image on a sand-blasted Al plate. The atmospheric MTF over a parallel proximate path will be measured by an instrument which scans the image of the distant visible laser source with a variable spatial frequency reticle. This experiment will be in progress during January 1972.

T. J. Gilmartin  J. Z. Holtz
L. J. Sullivan  J. A. Daley, Jr.

## REFERENCES


1. Optics Research Report, Lincoln Laboratory, M.I.T. (1971:1), pp. 48-49, DDC AD-888823-L.
2. M. Baer, private communication.
3. M.C. Teich, "Homodyne Detection of Infrared Radiation from a Moving Diffuse Target," Proc. IEEE 57 (1969), pp. 786-792.
4. Optics Research Report, Lincoln Laboratory, M.I.T. (1969:1), pp. 6-9, DDC AD-855883.
5. J.J. Dennis, "A 10.6$\mu$ Four-Port Circular Using Free-Carrier Rotation in InSb," IEEE J. Quantum Electron. QE-3 (1967), p. 416.
6. J.H. McCoy, D.B. Rensch and R.K. Long, Appl. Opt. 8, 1471 (1969).

## DOCUMENT CONTROL DATA – R&D

*(Security classification of title, body of abstract and indexing annotation must be entered when the overall report is classified)*

1. ORIGINATING ACTIVITY *(Corporate author)*
Lincoln Laboratory, M.I.T.

2a. REPORT SECURITY CLASSIFICATION
Unclassified

2b. GROUP
None

3. REPORT TITLE
Optics Research

4. DESCRIPTIVE NOTES *(Type of report and inclusive dates)*
Semiannual Report – 1 July through 31 December 1971

5. AUTHOR(S) *(Last name, first name, initial)*
Kingston, Robert H.

| 6. REPORT DATE | 7a. TOTAL NO. OF PAGES | 7b. NO. OF REFS |
|---|---|---|
| 31 December 1971 | 94 | 35 |

8a. CONTRACT OR GRANT NO. F19628-70-C-0230

b. PROJECT NO. ARPA Order 600

c.

d.

9a. ORIGINATOR'S REPORT NUMBER(S)
Optics Research (1971:2)

9b. OTHER REPORT NO(S) *(Any other numbers that may be assigned this report)*
ESD-TR-72-31

10. AVAILABILITY/LIMITATION NOTICES
Statement A
Distribution ~~limited~~ to U.S. Government ~~agencies only; test and evaluation, 21 April 1972~~.
~~Other~~ requests for ~~this~~ document must be referred to ~~ESD-TR-2~~.

11. SUPPLEMENTARY NOTES
None

12. SPONSORING MILITARY ACTIVITY
Advanced Research Projects Agency,
Department of Defense

13. ABSTRACT

This report covers work of the Optics Division at Lincoln Laboratory for the period 1 July through 31 December 1971. The topics covered are laser technology and propagation, optical measurements and instrumentation, and laser radar and tracking. Additional information on the optics program may be found in the semiannual technical summary reports to the Advanced Research Projects Agency.

14. KEY WORDS

optics
laser technology
thermal blooming
optical devices
optical systems
KC-135
laser radar imaging system
air pollution control

DEPARTMENT OF THE AIR FORCE
HEADQUARTERS ELECTRONIC SYSTEMS DIVISION (AFSC)
LAURENCE G. HANSCOM FIELD, BEDFORD, MASSACHUSETTS 01730

REPLY TO ATTN OF: TML (Lincoln Lab) 23 January 1974

SUBJECT: Review of Technical Report(s) Marked with a Distribution Limitation

TO: Defense Documentation Center
DDC-TSR
Cameron Station
Alexandria, Virginia 22314

1. As directed by ODDR&E, we have re-examined the need for a distribution limitation statement on the following document(s):

(1) ESD-TR-72-31; AD #901 213L

(2) _____

(3) _____

(4) _____

(5) _____

2. This letter documents the review and our determination that the distribution statement(s) B should be replaced with a statement A.

FOR THE COMMANDER

EUGENE C. RAABE, Lt Colonel, USAF
Chief, Lincoln Laboratory Project Office

Cys to: ESD (DRI)
Hq AFSC (DLXL)
Linc Lab (R. Clarke)

DEPARTMENT OF THE AIR FORCE
HEADQUARTERS ELECTRONIC SYSTEMS DIVISION (AFSC)
LAURENCE G. HANSCOM FIELD, BEDFORD, MASSACHUSETTS 01730

REPLY TO ATTN OF: TML (Lincoln Lab) 23 January 1974

SUBJECT: ESD-TR-72-31, dtd Dec 71, "Optics Research: 2".

TO: DDC/Air Force Liaison Representative
Cameron Station
Alexandria, VA 22314

1. I certify that the subject TR has been reviewed and approved for public release by the controlling office and the information office in accordance with AFR 80-45/AFSC Sup 1. It may be made available or sold to the general public and foreign nationals.

2. Distribution statement A appears on the subject TR and the DD Form 1473 as required by AFRs 80-44 and 80-45.

FOR THE COMMANDER

EUGENE C. RAABE, Lt Colonel, USAF
Chief, Lincoln Laboratory Project Office

Atch
Cys to: ESD (DRI)
Hq AFSC(DLXL)